Second Order Convergent Discontinuous Galerkin Projection Method for Dispersive Shallow Water Flows

Dissertation with the aim of achieving a doctoral degree at the
Faculty of Mathematics, Informatics and Natural Sciences
Department of Mathematics Universität Hamburg

submitted by Anja Jeschke
Hamburg, 2018

Day of oral defense: October 17^{th}, 2018
– Corrected version –
The following evaluators recommend
the admission of the dissertation

Prof. Dr. Jörn Behrens
Department of Mathematics
Universität Hamburg
Hamburg, Germany
email: joern.behrens@uni-hamburg.de

Prof. Dr. Geir K. Pedersen
Department of Mathematics
University of Oslo
Oslo, Norway
email: geirkp@math.uio.no

Declaration on oath

I hereby declare on oath, that I have written the present dissertation on my own and have not used other than the acknowledged resources and aids.

.....	.....
Date and place	Signature

Der HERR ist mein Fels, meine Burg
und mein Erretter.

2. Samuel 22,2

Kurzfassung

In dieser Arbeit wird ein unstetiges Galerkin (DG)-Verfahren zweiter Konvergenzordnung für die nicht-hydrostatische Erweiterung der Flachwassergleichungen in einer Raumdimension vorgestellt. Dieses Verfahren ist als Projektionsverfahren implementiert, und es ist, nach dem Kenntnisstand der Autorin, das erste DG-Verfahren und das erste Verfahren zweiter Konvergenzordnung für die nicht-hydrostatischen Gleichungen. Analytische Lösungen resultieren aus einer Äquivalenz dieser Gleichungen zu bekannten Gleichungen des Boussinesq-Typs. Diese Äuqivalenz kann gezeiget werden, falls eine Annahme in der Herleitung der nicht-hydrostatischen Gleichungen angepasst wird. Diese Annahme ist das vertikale Druckprofil des nicht-hydrostatischen Drucks. Eine Verbesserung der Verfahrenseffizienz wird vorgestellt, die dadurch erreicht wird, dass die nicht-hydrostatischen Gleichungen nur lokal auf einem Teilgebiet gelöst werden.

Für die Erweiterung des Gültigkeitsbereichs der hydrostatischen Flachwassergleichungen zur Modellierung von Dispersion werden üblicherweise zwei unterschiedliche Ansätze verwendet: Die Gleichungen des Boussinesq-Typs und die nicht-hydrostatische Erweiterung der Flachwassergleichungen. Bisher wurden beide Ansätze noch nicht analytisch in Bezug auf ihre Annahmen verglichen. Das vertikale Druckprofil des nicht-hydrostatischen Drucks in den nicht-hydrostatischen Gleichungen wird traditionell als linear angenommen. In dieser Arbeit wird diese Annahme durch die Herleitung eines quadratischen Druckprofil ersetzt, die auch den Gleichungen des Boussinesq-Typs zugrunde liegt. Dadurch wird Äquivalenz der nicht-hydrostatischen Gleichungen zu den Green-Naghdi-Gleichungen gezeigt, die sich im Falle konstanter Bodentopographie zu den Serre-Gleichungen vereinfachen. Unter Verwendung des linearen Druckprofils kann keine Äquivalenz zu einer bekannten Gleichung vom Boussinesq-Typ gezeigt werden. Im Grenzfall der langen Wellen ist das quadratische Druckprofil zu wählen.

Zur Diskretisierung der nicht-hydrostatischen Gleichungen wird ein DG-Verfahren zweiter Ordnung präsentiert. Ein inkrementelles Projektionsverfahren unterteilt die zeitdiskreten Gleichungen in einen Prediktorschritt, die Lösung einer elliptischen Gleichung und einen Korrekturschritt. Der Prediktorschritt verwendet das Runge-Kutta-DG (RK-DG)-Verfahren mit linearen Polynomen und einer linearen Extrapolation des nicht-hydrostatischen Druckterms. Die elliptische Gleichung für den nicht-hydrostatischen Druck wird als System erster Ordnung

und unter Verwendung des lokalen DG (LDG)-Verfahrens gelöst. Der Korrekturschritt aktualisiert die im Prediktorschritt berechneten Größen mit dem nicht-hydrostatischen Druck der elliptischen Gleichung. Zur Verwendung im LDG-Verfahren werden numerische Flüsse für periodische und reflektierende Randbedingungen der nicht-hydrostatischen Gleichungen hergeleitet und deren Stabilität gezeigt.

Analytische Lösungen für den Testfall der stehenden Welle und eine Solitärwelle der Serre-Gleichungen ermöglichen die Durchführung von Konvergenztests mit dem numerischen Verfahren, um die zweite Genauigkeitsordnung auf konstanter Bodentopographie zu zeigen. Das numerische Modell wird außerdem mithilfe von analytischen Lösungen und Labordaten unter Verwendung von Dirichlet-, periodischen und reflektierenden Randbedingungen, komplettiert durch ein Überflutungsschema, validiert. Beide Druckprofile verhalten sich gleichmaßen gut unter reflektierenden Randbedingungen und im Überflutungsprozess. Auf nicht-konstanter Bodentopographie ist es dem vorliegenden Verfahren nicht möglich alle Eigenschaften der Green-Naghdi-Gleichungen wiederzuspiegeln. Daher kann in manchen Fällen das lineare Druckprofil bessere Ergebnisse im Vergleich zum quadratischen Druckprofil zeigen. Auf konstanter Bodentopgraphie zeigen beide Druckprofile die erwarteten Ergebnisse.

Die Entwicklung einer lokalen Version des nicht-hydrostatischen Modells verbessert die Effizienz des Verfahrens. Ein einfaches Kriterium, das auf linearer Theorie basiert, wird zur Unterteilung des Rechengebiets in eine hydrostatische und eine nicht-hydrostatische Region definiert. Vorläufige Tests der lokalen Version zeigen im Vergleich mit dem globalen nicht-hydrostatischen Modell sehr ähnliche Ergebnisse, falls sowohl das Kriterium als auch die Auflösung sorgfältig ausgewählt werden. Die lokale Version des nicht-hydrostatischen Verfahrens spart ca. 60% des zusätzlichen Rechenaufwands des nicht-hydrostatischen Verfahrens im Vergleich zur alleinigen Lösung der hydrostatischen Gleichungen.

Abstract

This thesis presents a second order convergent discontinuous Galerkin (DG) method for the non-hydrostatic extension for shallow water equations in one spatial dimension. The scheme is implemented as a projection method, and it is, to the author's knowledge, the first DG method as well as the first scheme of second order of convergence for this non-hydrostatic equation set. Analytical solutions result from an equivalence of Boussinesq-type equations to the non-hydrostatic extension for shallow water equations. The equivalence is shown in case of an assumption in the derivation of the non-hydrostatic equation set is adapted. This assumption is the vertical profile of the non-hydrostatic pressure. Computational efficiency issues are tackled applying the non-hydrostatic equation set in a local manner on a subset of the computational domain.

Two different approaches are considered traditionally, if the hydrostatic regime of validity of the shallow water equations is expanded to model dispersive properties: Boussinesq-type equations and the non-hydrostatic extension for shallow water equations. So far, both approaches were not compared analytically with respect to underlying physical assumptions. The vertical profile of the non-hydrostatic pressure considered in the non-hydrostatic equation set is usually linear. We adapt the assumption of a linear pressure profile to be quadratic as in Boussinesq-type equations to show equivalence. In this case, the non-hydrostatic extension for shallow water equations is equivalent to the Green-Naghdi equations reducing to the Serre equations on constant bathymetry. There is no equivalence to any known Boussinesq-type equation, if the linear pressure profile is applied. The quadratic pressure profile is the correct one in the long-wave limit.

The non-hydrostatic equation set is discretized with a DG scheme of second order. An incremental projection method splits the time-discrete equations into a predictor relying on the hydrostatic shallow water equations, the solution of an elliptic equation, and a correction step. The predictor applies the Runge-Kutta DG method with linear polynomials and a linear extrapolation for the non-hydrostatic pressure term. The elliptic equation for the non-hydrostatic pressure is solved as a system of first order equations using the local discontinuous Galerkin (LDG) method. The corrector step updates the predicted quantities with the non-hydrostatic pressure computed with the elliptic equation. Numerical fluxes for the LDG method corre-

sponding to periodic and reflecting boundary conditions for the non-hydrostatic equation set are derived and their stability is proofed.

Analytical standing and solitary wave solutions of the Serre equations enable convergence tests with the numerical model to show second order accuracy on constant bathymetry. Furthermore, the non-hydrostatic model is validated with analytical solutions and experimental data using Dirichlet, periodic and reflecting boundary conditions completed with an inundation scheme. Both profiles behave equally well under reflection and during the inundation process. On non-constant bathymetry, the present model formulation is not able to represent all properties of the Green-Naghdi equations. Hence, the linear pressure profile may yield better results compared to the quadratic pressure profile. On constant bathymetry, both pressure profiles behave as expected.

The development of a local approach of the non-hydrostatic model improves the computational efficiency. A simple splitting criterion is defined that is based on linear theory and separates the computational domain into a hydrostatic and a non-hydrostatic region. Preliminary tests applying the local approach show very similar model results compared to the global non-hydrostatic model results, if the splitting criterion as well as the resolution are chosen carefully. The local approach saves approximately 60% of the computational overhead of the non-hydrostatic model compared to the hydrostatic model.

Contents

1 Introduction

Long surface gravity waves dominate large-scale phenomena in ocean dynamics such as tides, storm surges and tsunamis. Therefore, modeling these types of waves has been of interest for a long time. The shallow water equations are a good approximation to describe most aspects of these phenomena fairly well, but the validity of this model is limited to flows being in hydrostatic balance, where the pressure is mostly hydrostatic. However, if the wave length becomes small or if the wave propagates over rapidly varying bathymetry, the assumption of a small ratio between vertical and horizontal scales of motion loses its validity and the influence of non-hydrostatic effects on the wave motion is not negligible anymore. In both cases, dispersion is introduced into the flow motion.

An example for very long surface gravity waves are tsunamis. The water depth is related to their phase speed and results in propagation velocities of approximately 700 km/h which can imply short warning times. Although present tsunami warning systems rely on simulation tools using the hydrostatic model assumption due to their low computational cost, the inclusion of dispersion may be beneficial in order to improve the results. Hydrostatic models may overestimate the tsunami wave height leading to too high evacuation costs. A dispersive model is able to better represent the second and third wave [59]. Mid-size earthquakes and most landslides tend to generate tsunami waves that develop distinguished dispersive properties during oceanic propagation at least in some spatial directions, whereas dispersion has no large influence on tsunami waves generated by the largest earthquakes [52]. However, the understanding of the interaction of dispersive effects and tsunami generation, propagation and run-up is still far from being complete. Dispersive water wave models were developed in order to include dispersive effects into mathematical models for shallow water waves. Two different approaches gained attention: Boussinesq-type equations and the non-hydrostatic extension for shallow water equations.

The derivation of Boussinesq-type equations uses asymptotic expansions in non-dimensional parameters for dispersion and non-linearity for each variable of the incompressible Euler equations of motion. The first equations of such type were derived in the 19^{th} century by Boussinesq [13, 14]. The attempt is to eliminate the dependency on the vertical axis from the equations while retaining some important properties. Different Boussinesq-type equation sets

have been published using different expansion orders and formulations [17, 64, 68, 73, 74, 77, 82]. According to their respective expansion order, models are described by the terms weakly, moderately or fully dispersive and non-linear. Assumptions on the vertical velocity and the pressure profile help to derive a closed system of equations for the surface elevation and the depth-averaged horizontal velocities. Higher order derivatives and mixed space-time derivatives appear in Boussinesq-type equation sets, which often cause problems in the numerical discretization. Different strategies were used [39, 41] to get rid of the time derivative in the non-linear terms. Other attempts add additional viscosity into the equations [78] or use Boussinesq-type equations for multiple layers [70, 71]. If dispersion is disregarded in Boussinesq-type equations, they reduce to the shallow water equations.

The second approach called non-hydrostatic extension for shallow water equations is more directly linked to the solution of the three-dimensional incompressible Navier-Stokes equations. Hence, the inclusion of viscosity and multiple layers comes with the derivation naturally. However, the non-hydrostatic part of the pressure is not a dynamical variable, but serves as a Lagrange multiplier. A divergence constraint is needed to close the equation set. Hence, the basis of the method is a projection method [28, 97] in its version of a pressure-correction scheme solving the time-discrete equations stepwise: In each time step, an auxiliary system is solved first by disregarding a divergence constraint (the incompressibility condition) in the governing equations. Second, the resulting intermediate momentum is corrected by the solution of an elliptic equation to be in compliance with the divergence constraint. A decomposition of the pressure into hydrostatic and non-hydrostatic components [26, 91] serves to apply the projection method to the non-hydrostatic extension for shallow water equations. This splitting is advantageous because the solver for the non-hydrostatic equation sets can resort to the solver for the shallow water equations (the auxiliary system). This extension still requires the solution of an additional elliptic equation in each time step. We refer to this procedure as projection method in the following, whereas we use the terms *non-hydrostatic extension for shallow water equations* or *non-hydrostatic equation set* for the continuous system of equations. The combination of both we call a *non-hydrostatic model*. Non-hydrostatic models were developed to solve equations numerically depending on three spatial dimensions. The vertical dependence of unknown quantities is discretized as linear approximations between multiple layers. The depth-averaged discrete non-hydrostatic equation set is the simplified one-layer case derived from the original multi-layer approach.

These equation sets were usually studied separately. The conjecture that non-hydrostatic models may be comparable to Boussinesq-type wave models was made in [92]. Numerical comparisons seemed to confirm this statement [92, 101]. But an analytic comparison regarding different underlying physical assumptions is missing in the literature. Hence, we aim at extracting the main different physical assumptions of both approaches. We focus on depth-averaged equations to find an analytic Boussinesq-type formulation for non-hydrostatic equation sets. We adapt the depth-averaged non-hydrostatic extension for shallow water equations to be

equivalent to well-known Boussinesq-type equations. We explain how non-hydrostatic equation sets are advantageous with respect to mixed space-time derivatives in the corresponding Boussinesq-type equations.

Other approaches have been performed previously to compare non-hydrostatic equation sets and Boussinesq-type equations. Emphasis was put on linear dispersion relations [5, 6, 38] in order to match the full linear dispersion relation as best as possible. A rewriting of the non-hydrostatic equation system as a closed continuous system for the depth-averaged equation set helps to derive a Boussinesq-type formulation of the depth-averaged non-hydrostatic equation set [5, 98]. Both works stated that there is an another coefficient in the equation set on constant bathymetry and in front of the linear dispersion term compared to Boussinesq-type equations [5]. The multi-layer non-hydrostatic equation set is written in a Boussinesq-type formulation [6]. A parameter for the non-hydrostatic pressure relating the bottom and half-height non-hydrostatic pressure in a two-layer non-hydrostatic equation set is introduced [5]. An attempt is made to split the vertical profile of the non-hydrostatic pressure from temporal and spatial horizontal dependencies [101]. A Boussinesq-scaling is included in a projection method [41]. But in none of the cited works, the physical assumptions are adapted nor an equivalence of non-hydrostatic equation sets to other Boussinesq-type equations is shown, which is one of this thesis' goals.

Numerical models for dispersive shallow water flows are constructed on the basis on both approaches as well. The first Boussinesq-type models were finite difference models, because the ease of their implementation. Finite element discretizations came up in order to deal with complex geometries. Since the 2000s, finite volumes became the dominating discretization technique [17] as the local conservation property is advantageous for fluid flows. However, the third-order dispersive terms inherent in Boussinesq-type equations are not easy (but possible) to treat with finite volume techniques [11]. Hence, combined discretizations of finite volumes (for hyperbolic shallow water terms) and finite differences (for dispersive terms) were developed [10, 64]. More recently, discontinuous Galerkin (DG) methods applying implicit time stepping schemes [42, 106] or explicit Runge-Kutta time stepping schemes [43, 45, 79] are arising. Implicit methods are in use to overcome the severe time step restriction $\Delta t \sim (\Delta x)^3$ [42] inherent in explicit schemes that are in need to treat third-order spatial derivatives. Usually, higher order methods are used and proofed for convergence compared to analytical solutions.

Concerning non-hydrostatic models, the development originates in solving the three-dimensional incompressible Navier-Stokes equations. Hence, multi-layer methods were considered. Finite difference models with more than ten vertical layers [26, 27, 93] formed the start of numerical investigations applying non-hydrostatic models. The models agreed well with experiments, because grids with high resolution and with 10-20 layers were applied. Important improvements using this solution procedure were the reduction of the number of required vertical layers to 1–3 layers while still achieving the desired dispersion accuracy [92] and a minimized Poisson equation formulation [38] allowing for the same computational effort as

depth-averaged (one-layer) systems. The multi-layer equation set has been employed widely [46, 62, 72, 92, 108] and was also partly compared to realistic data with adequate results. Similarly, the depth-averaged version of the non-hydrostatic equation set found its application in several numerical methods, using finite differences [92], finite volumes [37, 38], finite elements [48, 101, 103] and combined discretizations of finite volumes and finite elements [3] to treat hydrostatic and dispersive terms differently.

A lot of similarities arise when comparing the development status of models discretizing both approaches: Developers of both approaches aim at representing higher dispersion accuracy, including extra features as vertical flow structure and viscosity, and treating efficiency issues. Numerical solutions are graphically compared to analytical solutions as well as laboratory and real-world data.

But there are at least three aspects in which the development of Boussinesq-type models is more advanced and the development of non-hydrostatic models is falling short: First, there is no discontinuous Galerkin model for the non-hydrostatic equation set so far; second, higher (than first) order models are rarely developed (except [2, 25, 44]); and third, the habit of testing numerical solutions for convergence with analytical solutions is usually not pursued. To the author's best knowledge, the single exception with respect to the third issue is [2] using an analytical solitary wave solution constructed in [16]. Regarding the second issue, [2] also aims at constructing a second order model. However, convergence tests revealed an order of convergence less of second order only. The authors [25, 44] claimed to present a model for the non-hydrostatic equation set that is formally second order. Convergence studies showed second order behavior, but their discrete model was compared to a finest numerical solution. However, we emphasize that they use a non-incremental projection method. We will show, that an incremental projection method is needed to obtain a method for the non-hydrostatic equation set that is fully second order convergent compared to analytical solutions. Therefore, this thesis aims at handling these three short-comings of current non-hydrostatic models in comparison to Boussinesq-type models.

The choice of a DG discretization with low order polynomials goes along with the concern about efficiency, as the degrees of freedom are doubled at cell interfaces. Compared to other discretizations, this drawback is reduced with increasing order of approximation. Furthermore, DG discretizations allow to straight-forward increase the approximation order. Hence, they provide a suitable choice to make depth-averaged non-hydrostatic models more competitive and comparable with state-of-the-art Boussinesq-type models.

However, the concern about efficiency for low order DG discretizations in combination with non-hydrostatic models has to be taken seriously. The problem may not occur in idealized testing situations, but if the model should assist in real-world simulations including much larger computational domains and simulation times. Therefore, this thesis presents a local version of the non-hydrostatic extension for shallow water equations. The idea is to solve the non-hydrostatic equation set in the most important spatial regions only and resort to the

cheaper hydrostatic equations elsewhere. The most important task is to determine suitable criteria to split the computational domain into regions that are important with respect to dispersive effects and regions that can be treated with the hydrostatic equations separately. The determination of the criteria also involves the definition of the quantity of information that may be considered to be negligible.

Similar ideas were studied in application to multi-layer ocean and atmospheric models. Usually, different models are coupled [47, 49] or grids of different resolutions in spatial regions of different physics are used [12, 49, 80]. These approaches have to consider strategies for grid nesting and interpolation to account for varying resolutions. An exception is [75, 76] solving the incompressible Navier-Stokes equations with a single model. To consider varying resolutions is reasonable if three-dimensional models are applied approximating the primitive equations. However, we do not aim at approximating the primitive equations, but at reproducing the simplified dispersive equation sets. Hence, we focus on locally adapting the physics only while applying the same resolution in all spatial regions. Concerning depth-averaged dispersive equation sets, the idea to resolve the dispersive effects in localized regions only was mentioned before in the context of modeling wave breaking (see [17] for an overview) and in the context of long-term wave propagation and inundation [90]. The latter couples a hydrostatic model with a Boussinesq-type model whereas both models use different discretization techniques. This may lead to the introduction of numerical errors in addition to physical errors at the splitting interfaces. Hence, we present a locally adapting physics model based on one single model. We consider a simple criterion to split the computational domain and use test cases to evaluate their ability to track the propagating wave in a stable and appropriate manner.

As explained in detail above, the purpose of this thesis is to answer the following research questions:

1. What are the physical assumptions distinguishing the depth-averaged non-hydrostatic extension for shallow water equations and Boussinesq-type equations? Can we obtain equivalence?

2. How do both physical assumptions influence the propagation of dispersive waves?

3. How could we set up a discontinuous Galerkin discretization of the depth-averaged non-hydrostatic extension for shallow water equations?

4. What efforts do we have to undertake to get a second order convergent discontinuous Galerkin discretization for the depth-averaged non-hydrostatic extension for shallow water equations? Are we able to show second order convergence compared to analytical solutions?

5. Can we make use of the locality of dispersive effects? Is the model able to produce stable and reasonable results in this case?

This thesis is structured as follows: The first research question is answered in chapter 2 in which we derive the non-hydrostatic equation set. Here, the second question is tackled analytically. These results are confirmed and extended numerically through simulations in chapter 3. This chapter is also concerned with the response to the third and fourth question. Chapter 4 responds to the last question. Conclusions and an outlook in chapter 5 serve as a summary of the new contributions of this thesis.

2 Equivalence to Boussinesq-type equations

This chapter contains main parts of the publication of Jeschke et al. (2017) "Depth-averaged Non-hydrostatic Extension for Shallow Water Equations with Quadratic Vertical Pressure Profile: Equivalence to Boussinesq-type Equations" (see [61]). The contents of the appendix of that paper are included in the Appendix A of this thesis.

The content of the paper is adapted to better fit into the structure of this thesis in the following aspects: The introduction and conclusion (section 1 and 6 in [61]) are moved to chapters 1 and 5. Numerical results of section 5 in [61] are not included in order to avoid duplication with numerical results in chapter 3. Analytical results of the test case standing wave are added to section 2.4.1 (section 4.1 in [61]). Section 2.4.3 is added describing analytical solutions of the test cases standing wave and solitary wave including the discussion about the solitary wave of the KdV equation in which the coefficient ν changes to η.

2.1. Abstract

We reformulate the depth-averaged non-hydrostatic extension for shallow water equations to show equivalence with well-known Boussinesq-type equations. For this purpose, we introduce two scalars representing the vertical profile of the non-hydrostatic pressure. A specific quadratic vertical profile yields equivalence to the Serre equations. In this case, one single scalar in the traditional equation system needs to be modified. Equivalence can also be demonstrated with other Boussinesq-type equations from the literature when considering variable depth, but then the non-hydrostatic extension involves mixed space-time derivatives. In case of constant bathymetries, the non-hydrostatic extension is another way to circumvent mixed space-time derivatives arising in Boussinesq-type equations. On the other hand, we show that there is no equivalence when using the traditionally assumed linear vertical pressure profile. Linear dispersion and asymptotic analysis show the advantages of the quadratic compared to the linear vertical non-hydrostatic pressure profile in the depth-averaged non-hydrostatic extension for shallow water equations.

2.2. Governing equations

In this section, a non-hydrostatic extension for the shallow water equations is derived similarly to derivations given in the literature concerning non-hydrostatic models [37, 48, 92, 101, 103]. The differences to the other approaches are threefold: We restrict ourselves to the depth-averaged one-layer case, we set up a system of equations formulated in depth-averaged variables only, and we look explicitly at the vertical profiles of the velocity and the non-hydrostatic pressure. For the latter, two different vertical pressure profiles are discussed and the system of equations is derived in such a way, that we are able to specify the profile after setting up the equations. This strategy allows us to investigate differences between the two choices analytically and numerically in the following sections.

Throughout this chapter, we use lower case letters for variables independent of the vertical coordinate z, and upper case letters indicate z-dependent variables. Bold font denotes vectors while scalar variables are written in normal font.

2.2.1. The non-hydrostatic extension for shallow water equations

The incompressible Euler equations of motion

$$\boldsymbol{\nabla}_3 \cdot \boldsymbol{V} = 0, \tag{2.1}$$

$$\partial_t \boldsymbol{V} + \boldsymbol{\nabla}_3 \cdot (\boldsymbol{V}\boldsymbol{V}^T) = -\frac{1}{\rho}\boldsymbol{\nabla}_3 P - g\boldsymbol{E}_z \tag{2.2}$$

form the starting point for the derivation, with the three-dimensional gradient operator $\boldsymbol{\nabla}_3 = (\partial_x, \partial_y, \partial_z)^T$, the velocity $\boldsymbol{V} = (U, V, W)^T = (\boldsymbol{U}, W)^T$, the constant density ρ, the pressure P, the gravitational acceleration g and the unit vector in z-direction $\boldsymbol{E}_z$. In the literature on non-hydrostatic models, additional source terms such as Coriolis force and viscosity terms are common, e.g. [37, 48, 101]. The inclusion of these terms is straight forward, so we omit them here. The water depth $h = d + \xi$ is decomposed into the still water depth d and the elevation ξ of the free surface, as displayed in figure 2.1. The kinematic boundary conditions at the free surface and the fluid bottom, and the pressure boundary condition assuming a zero atmospheric pressure are

$$W_\xi := W(t, x, y, \xi) = \partial_t \xi + \begin{pmatrix} U_\xi \\ V_\xi \end{pmatrix} \cdot \boldsymbol{\nabla}\xi, \tag{2.3}$$

$$W_{-d} := W(t, x, y, -d) = -\begin{pmatrix} U_{-d} \\ V_{-d} \end{pmatrix} \cdot \boldsymbol{\nabla} d, \tag{2.4}$$

$$P_\xi = 0, \tag{2.5}$$

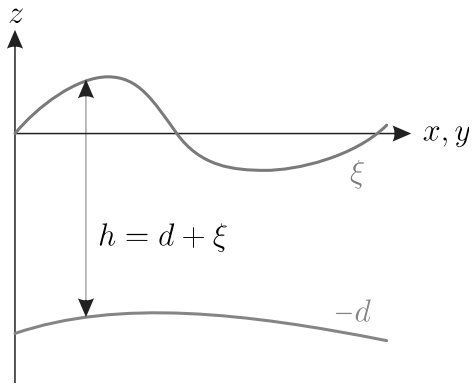

Figure 2.1.: Decomposition of the total water depth h into bottom and free surface elevation

where $\boldsymbol{\nabla}$ denotes the two-dimensional gradient operator $\boldsymbol{\nabla} = (\partial_x, \partial_y)^T$. The shallow water equations are derived from the Euler equations (2.1)–(2.2) under the assumption that vertical accelerations are small compared to horizontal accelerations. Hence, the vertical momentum equation would imply that the pressure P is purely hydrostatic. However, in order to obtain the non-hydrostatic correction for the shallow water equations, the pressure P is assumed to have a non-hydrostatic component P^{nh} in addition to the hydrostatic component P^{hy}. Therefore, the pressure P and its boundary conditions are given by

$$P = P^{hy} + P^{nh} = \rho g(\xi - z) + P^{nh}, \tag{2.6}$$

$$P_\xi = P^{hy}_\xi = P^{nh}_\xi = 0. \tag{2.7}$$

The splitting (2.6) is substituted into the Euler equations (2.1)–(2.2), which are depth-averaged by integrating over the fluid depth h. Therefore we obtain a system of equations solving for the water height and the depth-averaged unknowns

$$(u, v)^T = \boldsymbol{u} := \frac{1}{h}\int_{-d}^{\xi} \boldsymbol{U}\, dz, \qquad w := \frac{1}{h}\int_{-d}^{\xi} W\, dz, \qquad p^{nh} := \frac{1}{h}\int_{-d}^{\xi} P^{nh}\, dz. \tag{2.8}$$

The averaging of non-linear terms in (2.1)–(2.2) is made under the assumption of small vertical variation of $\boldsymbol{U}$. Then, the application of Leibniz's integration rule and boundary conditions (2.3)–(2.7) leads to

$$\partial_t \xi + \boldsymbol{\nabla} \cdot (h\boldsymbol{u}) = 0 \tag{2.9}$$

$$\partial_t \boldsymbol{u} + (\boldsymbol{u} \cdot \boldsymbol{\nabla})\boldsymbol{u} = -g\boldsymbol{\nabla}\xi - \frac{1}{\rho h}\left(\boldsymbol{\nabla}\left(h p^{nh}\right) - P^{nh}_{-d}\boldsymbol{\nabla} d\right) \tag{2.10}$$

$$\partial_t w + (\boldsymbol{u} \cdot \boldsymbol{\nabla})w = \frac{1}{\rho h} P^{nh}_{-d} \tag{2.11}$$

and the kinematic boundary conditions

$$W_\xi = \partial_t \xi + \boldsymbol{u} \cdot \boldsymbol{\nabla} \xi, \tag{2.12}$$

$$W_{-d} = -\boldsymbol{u} \cdot \boldsymbol{\nabla} d. \tag{2.13}$$

In these equations, values for $\boldsymbol{U}$ at the boundaries are replaced by $\boldsymbol{u}$. This is appropriate since the vertical velocity only couples with $\boldsymbol{u}$ and ξ through the small, non-hydrostatic pressure corrections in (2.10). Hence, small relative errors in w and W yield even smaller relative errors in $\boldsymbol{u}$ and ξ.

In [92], the discretization process starts already after deriving the equation system (2.9)–(2.13) plus a divergence constraint. Here, we combine the boundary conditions (2.12)–(2.13) with an expression for the depth-averaged vertical velocity w to recover the divergence constraint for purely depth-averaged equations. We assume the vertical profile of the vertical velocity W to be linear. This assumption was also made in the literature. The justification comes from the Euler continuity equation (2.1), where we again approximate $\boldsymbol{U}$ by $\boldsymbol{u}$, which yields $\partial_z W = -\nabla \cdot \boldsymbol{u}$. The linear vertical profile $W(z)$ and the depth-averaged vertical velocity w are given explicitly as

$$W(z) = W_{-d} + \frac{1}{h}(W_\xi - W_{-d})(d + z), \tag{2.14}$$

$$w = \frac{1}{2}(W_\xi + W_{-d}). \tag{2.15}$$

A reformulation of equation (2.15) using (2.12), (2.13) and (2.9) yields

$$\begin{aligned} 2\left(w + \boldsymbol{u} \cdot \boldsymbol{\nabla} d\right) = 2\left(w - W_{-d}\right) = W_\xi - W_{-d} = \partial_t \xi + \boldsymbol{u} \cdot \boldsymbol{\nabla}(d + \xi) \\ = -h\left(\boldsymbol{\nabla} \cdot \boldsymbol{u}\right), \end{aligned}$$

such that this divergence constraint combines the continuity equation with the assumption of the linear vertical profile of W and its boundary conditions. At this point, our non-hydrostatic extension for the shallow water equations formulated for depth-averaged variables is

$$\partial_t \xi + \boldsymbol{\nabla} \cdot (h\boldsymbol{u}) = 0 \tag{2.16}$$

$$\partial_t \boldsymbol{u} + (\boldsymbol{u} \cdot \boldsymbol{\nabla})\boldsymbol{u} = -g\boldsymbol{\nabla}\xi - \frac{1}{\rho h}\left(\boldsymbol{\nabla}\left(h p^{nh}\right) - P^{nh}_{-d}\boldsymbol{\nabla} d\right) \tag{2.17}$$

$$\partial_t w + (\boldsymbol{u} \cdot \boldsymbol{\nabla})w = \frac{1}{\rho h} P^{nh}_{-d} \tag{2.18}$$

$$2\left(w + \boldsymbol{u} \cdot \boldsymbol{\nabla} d\right) = -h\left(\boldsymbol{\nabla} \cdot \boldsymbol{u}\right). \tag{2.19}$$

Here, the first together with the second equation, neglecting the non-hydrostatic pressure

terms, form the shallow water equations. One additional equation is required to close the system (2.16)–(2.19), which is a relation between p^{nh} and the bottom value P^{nh}_{-d}. A vertical pressure profile helps to establish this relation. We present two different profiles in the next subsection.

2.2.2. The vertical pressure profile

Vertical profiles of the non-hydrostatic pressure distribution differ depending on the literature consulted. References following [92] for non-hydrostatic extension commonly utilize a linear vertical pressure profile. On the other side, references using Boussinesq-type equations (see, e.g., [86]) prefer a quadratic vertical pressure profile. In the following, both alternatives are discussed.

1. Linear vertical profile:
   The vertical pressure profile
   $$P^{nh}(z) = \frac{P^{nh}_{-d}}{h}(\xi - z) \tag{2.20}$$
   is found using the pressure boundary condition (2.7). Depth-averaging according to definition (2.8) yields the so called linear pressure relation
   $$P^{nh}_{-d} = 2p^{nh}. \tag{2.21}$$
   In the literature concerning non-hydrostatic models, the linear profile occurs explicitly for numerical reasons [101] or implicitly [92] in the integral hp^{nh} (see (2.8)) appearing in (2.17), which is approximated with $0.5hP^{nh}_{-d}$. This is exact if the non-hydrostatic pressure has a linear vertical profile. Additionally, the linear vertical profile (2.14) of W appears implicitly [92, 105] or explicitly [101]. The boundary values W_ξ and W_{-d} are traditionally additional unknowns in the depth-averaged non-hydrostatic equation system, because this depth-averaged method was derived from the multi-layer approach [92].

2. Quadratic vertical profile:
   In contrast to the previous linear profile, it is possible to get an equation-based argument for a quadratic vertical profile of the non-hydrostatic pressure. While deriving the depth-averaged divergence constraint, we obtained that W is linear in z. When inserting this into the vertical Euler momentum equation, the term $\partial_z P^{nh}$ becomes linear in z and hence P^{nh} needs to have a quadratic vertical profile. Application of the pressure boundary condition (2.7) leads to the quadratic profile given in Appendix A. By averaging this profile, we obtain the relation between p^{nh} and P^{nh}_{-d}, which is needed to close the

equation set (2.16)–(2.19), namely

$$P_{-d}^{nh} = \frac{3}{2}p^{nh} + \frac{1}{4}\rho h\Phi, \tag{2.22}$$

where $\Phi = -\boldsymbol{\nabla}d \cdot (\partial_t \boldsymbol{u} + (\boldsymbol{u}\cdot\boldsymbol{\nabla})\boldsymbol{u}) - \boldsymbol{u}\cdot\boldsymbol{\nabla}(\boldsymbol{\nabla}d)\cdot\boldsymbol{u}$. For the detailed derivation, see Appendix.

The equations (2.23)–(2.26) form the non-hydrostatic extension for shallow water equations

$$\partial_t \xi + \boldsymbol{\nabla}\cdot(h\boldsymbol{u}) = 0, \tag{2.23}$$

$$\partial_t \boldsymbol{u} + (\boldsymbol{u}\cdot\boldsymbol{\nabla})\boldsymbol{u} = -g\boldsymbol{\nabla}\xi - \frac{1}{\rho h}\left(\boldsymbol{\nabla}\left(hp^{nh}\right) - (f_{\mathsf{nh}}p^{nh} + f_{\mathsf{d}})\boldsymbol{\nabla}d\right), \tag{2.24}$$

$$\partial_t w + (\boldsymbol{u}\cdot\boldsymbol{\nabla})w = \frac{1}{\rho h}(f_{\mathsf{nh}}p^{nh} + f_{\mathsf{d}}), \tag{2.25}$$

$$2\left(w + \boldsymbol{u}\cdot\boldsymbol{\nabla}d\right) = -h\left(\boldsymbol{\nabla}\cdot\boldsymbol{u}\right), \tag{2.26}$$

using a general pressure relation

$$P_{-d}^{nh} = f_{\mathsf{nh}}p^{nh} + f_{\mathsf{d}}, \tag{2.27}$$

where the scalars f_{nh} and f_{d} are chosen to match either the pressure relation (2.21) or (2.22) based on a linear or quadratic vertical pressure profile.

2.3. Relation to other Boussinesq-type equations

In this section, we reformulate the depth-averaged non-hydrostatic extension for shallow water equations (2.23)–(2.26), such that we can easily compare it to well-known Boussinesq-type equations, where the first is a system of four equations in contrast to the latter being a system of two equations. We solve equation (2.26) for the vertical velocity yielding

$$w = -\frac{1}{2}h(\boldsymbol{\nabla}\cdot\boldsymbol{u}) - \boldsymbol{u}\cdot\boldsymbol{\nabla}d. \tag{2.28}$$

This vertical velocity is inserted into the vertical momentum equation (2.25) leading to

$$\partial_t w + (\boldsymbol{u}\cdot\boldsymbol{\nabla})w = \frac{1}{2}\Gamma + \Phi = \frac{1}{\rho h}(f_{\mathsf{nh}}p^{nh} + f_{\mathsf{d}})$$

with

$$\Gamma := h\left(-(\boldsymbol{\nabla}\cdot\partial_t\boldsymbol{u}) - (\boldsymbol{u}\cdot\boldsymbol{\nabla})(\boldsymbol{\nabla}\cdot\boldsymbol{u}) + (\boldsymbol{\nabla}\cdot\boldsymbol{u})^2\right) \tag{2.29}$$

$$\Phi := -\boldsymbol{\nabla}d\cdot(\partial_t\boldsymbol{u} + (\boldsymbol{u}\cdot\boldsymbol{\nabla})\boldsymbol{u}) - \boldsymbol{u}\cdot\boldsymbol{\nabla}(\boldsymbol{\nabla}d)\cdot\boldsymbol{u}. \tag{2.30}$$

With this knowledge, we eliminate p^{nh} in the horizontal momentum equation (2.24) resulting in our Boussinesq-type formulation of the non-hydrostatic extension for shallow water equations

$$\partial_t\xi + \boldsymbol{\nabla}\cdot(h\boldsymbol{u}) = 0, \tag{2.31}$$

$$\begin{aligned}\partial_t\boldsymbol{u} + (\boldsymbol{u}\cdot\boldsymbol{\nabla})\boldsymbol{u} + g\boldsymbol{\nabla}\xi &= -\frac{1}{\rho h}\left(\boldsymbol{\nabla}\left(hp^{nh}\right) - (f_{\mathsf{nh}}p^{nh} + f_{\mathsf{d}})\boldsymbol{\nabla}d\right)\\ &= -\frac{1}{h}\boldsymbol{\nabla}\left(h^2\left(\frac{1}{2f_{\mathsf{nh}}}\Gamma + \frac{1}{f_{\mathsf{nh}}}\Phi - \frac{f_{\mathsf{d}}}{f_{\mathsf{nh}}\rho h}\right)\right) + \boldsymbol{\nabla}d\left(\frac{1}{2}\Gamma + \Phi\right).\end{aligned} \tag{2.32}$$

It still depends on both scalars f_{nh} and f_{d}, which will be set in the following. If these scalars are designed according to the pressure relation (2.22) as $f_{\mathsf{nh}} = \frac{3}{2}$, $f_{\mathsf{d}} = \frac{1}{4}\rho h\Phi$, the non-hydrostatic equation system (2.23)–(2.26) for a non-constant bathymetry is equivalent to

$$\partial_t\xi + \boldsymbol{\nabla}\cdot(h\boldsymbol{u}) = 0, \tag{2.33}$$

$$\partial_t\boldsymbol{u} + (\boldsymbol{u}\cdot\boldsymbol{\nabla})\boldsymbol{u} + g\boldsymbol{\nabla}\xi = -\frac{1}{h}\boldsymbol{\nabla}\left(h^2\left(\frac{1}{3}\Gamma + \frac{1}{2}\Phi\right)\right) + \boldsymbol{\nabla}d\left(\frac{1}{2}\Gamma + \Phi\right). \tag{2.34}$$

These equations are well-known Boussinesq-type equations, as they are the same as equation (26) in [66], which are the Green-Naghdi equations [54], when assuming irrotational motion. In one dimension, they are derived in [68] (equation (B3)) and also in [86] (equation (13)). Hence, the one-dimensional version of the non-hydrostatic equation set (2.23)–(2.26) on a constant bathymetry are equivalent to the Serre equations [87], which yields $f_{\mathsf{d}} = 0$. On the contrary, there is no equivalence to a Boussinesq-type equation for the original depth-averaged non-hydrostatic extension for shallow water equations using the linear vertical pressure profile represented by $f_{\mathsf{nh}} = 2$ and $f_{\mathsf{d}} = 0$ in (2.23)–(2.26). However, the modification of the pressure profile yields the above equivalence.

In case of a constant bathymetry, this modification is easily adopted, since only the scalar f_{nh} needs to be adapted in (2.23)–(2.26). In case of a non-constant bathymetry, this equivalence has one drawback: If the pressure relation (2.22) is applied in (2.23)–(2.26), it is not clear anymore how to rewrite it as a projection method, because the scalar f_{d} contains the time derivative of the horizontal velocity. The projection method usually presumes right hand sides without time derivatives. Hence, we are not able to implement this equation set on the basis of our projection method, so the practical use gained out of the equivalence on a non-constant

bathymetry is not clear to us. Nevertheless, we can easily create a new set of equations by choosing $f_{\mathsf{nh}} = \frac{3}{2}$ and $f_{\mathsf{d}} = 0$, while still considering a non-constant bathymetry. Our resulting equations read

$$\partial_t \xi + \boldsymbol{\nabla} \cdot (h\boldsymbol{u}) = 0, \tag{2.35}$$

$$\partial_t \boldsymbol{u} + (\boldsymbol{u} \cdot \boldsymbol{\nabla})\boldsymbol{u} + g\boldsymbol{\nabla}\xi = -\frac{1}{h}\boldsymbol{\nabla}\left(h^2\left(\frac{1}{3}\Gamma + \frac{2}{3}\Phi\right)\right) + \boldsymbol{\nabla} d\left(\frac{1}{2}\Gamma + \Phi\right), \tag{2.36}$$

which differs from (2.33)–(2.34) only in one factor in front of the term $\frac{1}{h}\boldsymbol{\nabla}(h^2\Phi)$ containing higher order derivatives of the bathymetry. This equation can be subjected to a projection method. On constant bathymetries, it is equivalent to the above listed Boussinesq-type equations (2.33)–(2.34) and we have implemented it in the version of the depth-averaged non-hydrostatic extension for shallow water equations (2.23)–(2.26). Compared to (2.33)–(2.34), equations (2.35)–(2.36) neglect some influence arising from the non-constant bathymetry on the flow.

There are two types of mixed space-time derivatives in the Boussinesq-type equations (2.33)–(2.34): Some terms arise explicitly and some only implicitly in the equivalent non-hydrostatic equation set. We do not have to take care of such implicit mixed derivatives, because the treatment comes with our non-hydrostatic model. Thereby, our approach using non-hydrostatic models differs from previous attempts [39, 41] to deal with these terms. At the moment, we disregard the arising explicit terms in the non-hydrostatic equation set, as it was done in non-hydrostatic models previously. In case of constant bathymetries, we do not have to deal with mixed space-time derivatives at all.

2.4. Analytical properties

Basic analytical properties of the depth-averaged non-hydrostatic extension for the shallow water equations are discussed, depending on the vertical pressure profile applied. Both profiles are compared according to their linear dispersion relations and regarding their resulting behavior at the asymptotic wave front. For simplicity, we restrict ourselves to the one-dimensional case.

2.4.1. Linear dispersion relations

The calculation of linear dispersion relations assumes a constant bathymetry, meaning that the scalar f_{d} in (2.31)–(2.32) is set to zero in the following. Therefore, the linearized system

of equations with constant bathymetry reduces to

$$0 = \partial_t \xi + \partial_x (du),$$
$$\partial_t u + g\partial_x \xi = \frac{1}{2f_{\mathsf{nh}}} d^2 \partial_{txx} u,$$

where the scalar f_{nh} determines the vertical pressure profile. We consider harmonic solutions

$$u = \overline{u} e^{i(\kappa x - \omega t)}, \quad \xi = \overline{\xi} e^{i(\kappa x - \omega t)},$$

in the above system with the wave number κ, the frequency ω and the time t. Nontrivial solutions must satisfy the dispersion relation

$$\omega^2_{\mathsf{nh},f_{\mathsf{nh}}} = \frac{c^2_{\mathsf{sw}} \kappa^2}{1 + \frac{(\kappa d)^2}{2f_{\mathsf{nh}}}}, \tag{2.37}$$

where $c_{\mathsf{sw}} = \sqrt{gd}$ is the linear shallow water gravity wave speed. The dispersion relation resulting from the quadratic vertical pressure profile ($f_{\mathsf{nh}} = \frac{3}{2}$) is the same as for the Serre equations, so

$$\omega^2_{\mathsf{nh,quad}} = \omega^2_{\mathsf{Se}} = \frac{c^2_{\mathsf{sw}} \kappa^2}{1 + \frac{(\kappa d)^2}{3}}, \tag{2.38}$$

whereas the linear vertical pressure profile ($f_{\mathsf{nh}} = 2$) leads to the dispersion relation

$$\omega^2_{\mathsf{nh,lin}} = \frac{c^2_{\mathsf{sw}} \kappa^2}{1 + \frac{(\kappa d)^2}{4}}. \tag{2.39}$$

The same result is given in [38] for the linear vertical profile, and in [1] for both profiles. For comparison, the dispersion relation from the full linearized inviscid equations is (see, e.g., [104])

$$\omega^2_{\mathsf{nh,full}} = g\kappa \tanh(\kappa d). \tag{2.40}$$

These dispersion relations will be used for numerical validation in the next chapter.
Figure 2.2 shows a graphical comparison of all phase velocities above. In a close neighborhood of the shallow water assumption (i.e., in the limit $\frac{d}{\lambda} \to 0$), the quadratic vertical pressure profile gives a better phase velocity compared to the full reference solution than the linear profile, as known from series expansions around this state used in equation (2.41). However, for ratios $\frac{d}{\lambda} > 0.25$ approximately, the linear profile matches better. Another conclusion is the weaker dispersion of the linear pressure profile compared to the quadratic profile. This is graphically observed in figure 2.2, because the shallow water curve is closer to the curve of the linear profile than the curve representing the quadratic profile.

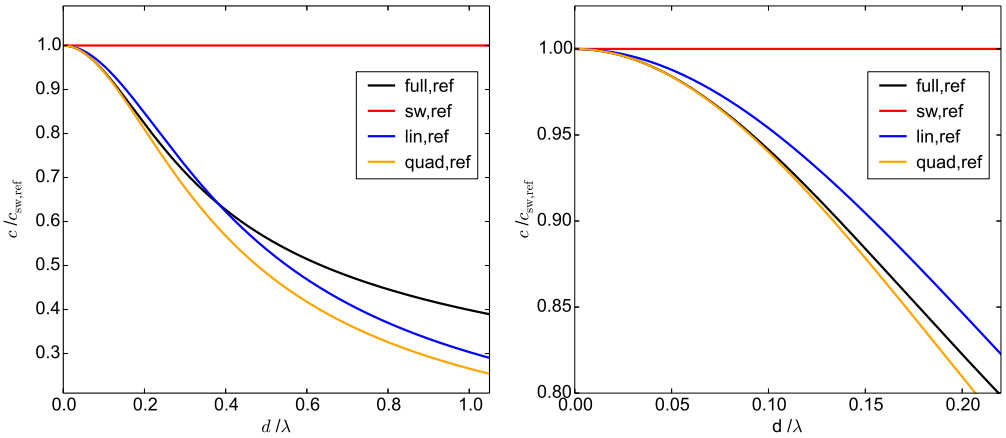

Figure 2.2.: Phase velocities: Comparison of analytic hydrostatic and non-hydrostatic phase velocities (left) and a zoom onto the close neighborhood of the long wave limit (right).

2.4.2. Asymptotic wavefront

For a wave propagation in the positive x-direction the linear dispersion relations in the previous subsection can be expanded in the wave number to yield

$$\omega = c_{\mathsf{sw}}\kappa(1 - \eta d^2\kappa^2) + O(\kappa^5). \tag{2.41}$$

The relation from the linear pressure profile (2.39) gives the coefficient $\eta = \frac{1}{8}$, while the remaining relations (2.38) and (2.40) share the coefficient $\eta = \frac{1}{6}$. Hence, the linear pressure profile yields too weak dispersion in the long wave limit.

The two terms in (2.41) suffice to determine some important general solutions for dispersive waves, which illustrate the effects of a wrong value for η. For large times the evolution governed by the linearized equations of a confined, plane, initial distribution of surface elevations on constant depth d will be dominated by the longest waves ($\kappa \to 0$). For any initial condition with a net elevation, or depression, we may then write (see [104], chapter 13.6)

$$\xi \sim \frac{V}{2(3c_{\mathsf{sw}}d^2\eta t)^{\frac{1}{3}}}\mathrm{Ai}\left(\frac{x - c_{\mathsf{sw}}t}{(3c_{\mathsf{sw}}d^2\eta t)^{\frac{1}{3}}}\right), \tag{2.42}$$

near the front of the wave train, where Ai is the Airy function, V is the volume per width of the initial elevation and η is as used in (2.41). It is noteworthy that this asymptotic solution for the wave front does not depend on the shape of the initial condition. The linear pressure profile yields a too small value for η, which in turn implies a wave front that is about 10%

too high and short (see figure 2.3). For realistic tsunamis, equation (2.42) should be taken only in a qualitative sense since the bathymetry is non-constant and the propagation is in two horizontal dimensions. Moreover, while the leading waves from moderately strong earthquakes rapidly develop the typical shape in figure 2.3, those from the strongest earthquakes will not do so even after passing long distances of whole oceans. However, some influence of dispersion will then be apparent. Examples and more details on dispersion in tsunamis are found in [52].

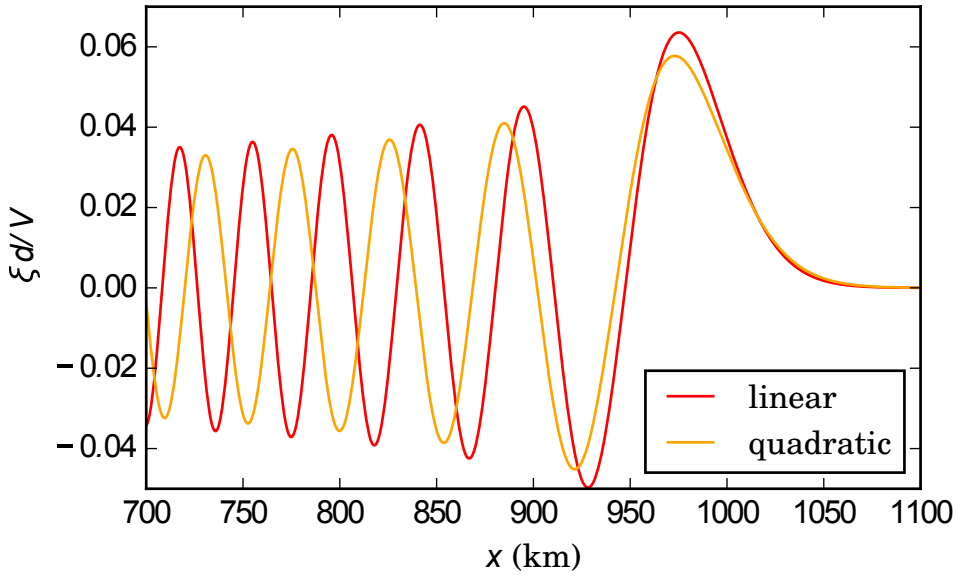

Figure 2.3.: The asymptotic wavefront, in a depth of $d = 5000$m, after 1h 15min, corresponding to a propagation distance of 1000km. The results for the quadratic pressure profile and full potential theory is drawn by an orange line, while the one for the linear pressure profile is represented by a red one.

2.4.3. Analytical solutions on constant bathymetry

The linearized as well as the non-linear version of the depth-averaged non-hydrostatic extension for the shallow water equations have analytical solutions on constant bathymetry. The list is far from being complete. These solutions presented serve as analytical test cases in the next chapter.

2.4.3.1. Linear standing wave

Both, the linearized systems of the non-hydrostatic extension for the shallow water equations and the shallow water equations have an analytic standing wave solution

$$\xi(\boldsymbol{x},t) = -a\sin(\kappa x)\cos(\kappa c t)\,, \tag{2.43}$$

$$u(\boldsymbol{x},t) = a\frac{c}{d}\cos(\kappa x)\sin(\kappa c t)\,, \tag{2.44}$$

$$v(\boldsymbol{x},t) = 0, \qquad \forall\ \boldsymbol{x} = (x,y)^T \in \Omega,\ \forall t \in \mathbb{R}_{\geq 0}, \tag{2.45}$$

with maximal amplitude a. The phase velocity $c = \frac{\omega_{\mathsf{nh}, f_{\mathsf{nh}}}}{\kappa}$ is chosen for the non-hydrostatic equation set and $c = c_{\mathsf{sw}}$ for the hydrostatic equation set, respectively. For the first, the analytic vertical velocity and the non-hydrostatic pressure is

$$w(\boldsymbol{x},t) = -\frac{d}{2}\partial_x u = \frac{1}{2}ac\kappa\sin(\kappa x)\sin(\kappa c t)\,, \tag{2.46}$$

$$p^{nh}(\boldsymbol{x},t) = \frac{d}{f_{\mathsf{nh}}}\partial_t w = \frac{ad}{2f_{\mathsf{nh}}}(c\kappa)^2\sin(\kappa x)\cos(\kappa c t)\,, \tag{2.47}$$

which is derived directly from the linearized version of the vertical velocity equation (2.25) and divergence constraint (2.26).

2.4.3.2. Propagating solitary wave

The non-hydrostatic extension for shallow water equations using the quadratic vertical pressure profile has an analytic solitary wave solution on constant bathymetry, because we showed the equivalence to the Serre equations [87]. We choose a solitary wave propagating in the positive x-direction, such that the analytic solution according to [86] is

$$\xi(\boldsymbol{x},t) = a\ \mathsf{cosh}^{-2}(K(x - ct - x_0)), \tag{2.48}$$

$$u(\boldsymbol{x},t) = c\frac{\xi(\boldsymbol{x},t)}{d + \xi(\boldsymbol{x},t)}, \tag{2.49}$$

$$w(\boldsymbol{x},t) = -0.5(d + \xi(\boldsymbol{x},t))\partial_x u(\boldsymbol{x},t) \tag{2.50}$$

$$\mathsf{th}(\boldsymbol{x},t) := \tanh(K(x - ct - x_0)), \tag{2.51}$$

$$p^{nh}(\boldsymbol{x},t) = (cdK)^2\frac{\xi(\boldsymbol{x},t)}{(d + \xi(\boldsymbol{x},t))f_{\mathsf{nh}}}\left(2d\frac{\mathsf{th}(\boldsymbol{x},t)}{d + \xi(\boldsymbol{x},t)} - \frac{\xi(\boldsymbol{x},t)}{a}\right) \tag{2.52}$$

with maximal amplitude a and propagation velocity $c = \sqrt{g(d+a)}$ on a constant depth d, scale factor $K = \sqrt{\left(\frac{3a}{4d^2(d+a)}\right)}$ and displacement x_0 on a domain of length l. Equation (2.50)

results from (2.26). The non-hydrostatic pressure p^{nh} is chosen, such that the vertical velocity equation is satisfied. This choice is also in line with the horizontal velocity equation.

Not all Boussinesq-type equations inherit an exact solitary wave solution, but leading order approximations are readily available and may be employed to illustrate how the linear pressure distribution affects the properties. When only the leading order of both non-linearity and dispersion, the latter given by (2.41), are taken into account, the wave dynamics are governed by the KdV equation ([104], chapter 13.11, 13.12)

$$\frac{\partial \xi}{\partial t} + c_{\mathsf{sw}} \left(1 + \frac{3\xi}{2d}\right) \frac{\partial \xi}{\partial x} + \eta c_{\mathsf{sw}} d^2 \frac{\partial^3 \xi}{\partial x^3} = 0. \tag{2.53}$$

Following the steps of the reference we then obtain the solitary wave solution of the same form as (2.48), but with other expressions for the scale factor and the celerity

$$K = \sqrt{\frac{a}{8d^3\eta}}, \quad c = \sqrt{gd}\left(1 + \frac{a}{2d}\right). \tag{2.54}$$

This provides the correct leading approximation to the solitary wave solution of full potential theory [55], as well as (2.48), while the linear pressure profile yields a wave that is 13% too short for a given initial amplitude a. On the other hand, to first order in a/d, the wave celerity c is independent of η. A solitary wave solution of the Serre equations ($\eta = \frac{1}{6}$) will be too long when used as an initial solitary wave for $\eta = \frac{1}{8}$. The wave will then adjust to a solitary wave solution for $\eta = \frac{1}{8}$ by becoming higher and slightly shorter, while a trailing wave system will emerge.

3 Second order discontinuous Galerkin model

The first order version of the method presented in this chapter was published in Jeschke et al. (2017) "A Discontinuous Galerkin Method for Non-hydrostatic Shallow Water Flows" (see [60]) including the validation tests on constant bathymetry. The content of the publication is rewritten and extended for this thesis.

3.1. Abstract

We present a second order discontinuous Galerkin (DG) model for the conservative formulation of the depth-averaged non-hydrostatic extension for the shallow water equations, which was derived in chapter 2 in primitive formulation. The model combines a second order incremental projection method and a DG discretization using piecewise linear polynomials. The predictor and corrector of the projection method relies on a second order Runge-Kutta DG method, whereas the elliptic system of equations of first order differential equations is treated with the local discontinuous Galerkin (LDG) method. Boundary conditions for the elliptic system of equations are derived and proofed to be stable. The equivalence to well-known Boussinesq-type equations shown in chapter 2 provides analytical solutions to the non-hydrostatic equation set and enables convergence tests. To the author's best knowledge, we present the first non-hydrostatic model that is second order accurate compared to analytical solutions. Different numerical simulations including non-constant bathymetry and inundation serve to validate the second order DG model.

3.2. Conservative non-hydrostatic equation set

The governing equations of this chapter are the one-dimensional non-hydrostatic extension for shallow water equations in conservative formulation

$$\begin{pmatrix} h \\ hu \\ hw \end{pmatrix}_t + \begin{pmatrix} hu \\ hu^2 + \frac{g}{2}h^2 + \frac{1}{\rho}hp^{nh} \\ hwu \end{pmatrix}_x = \begin{pmatrix} 0 \\ -ghb_x - \frac{1}{\rho}\left(f_{\mathsf{nh}}p^{nh} + f_{\mathsf{d}}\right)b_x \\ \frac{1}{\rho}\left(f_{\mathsf{nh}}p^{nh} + f_{\mathsf{d}}\right) \end{pmatrix}, \tag{3.1}$$

$$2hw - hu(h+2b)_x = -h(hu)_x. \tag{3.2}$$

Under the assumption of smooth quantities, these equations are a rewriting of the non-hydrostatic equation set (2.23)–(2.26) that is given in primitive formulation. The fluid depth h is measured from a bathymetry $b = b(x)$ to the water surface, as displayed in figure 3.1. Note that this definition varies compared to the definition of the bathymetry used in chapter 2 and displayed in figure 2.1. The functions h, hu, hw and p^{nh} are defined for $x \in \Omega \subset \mathbb{R}$ and time $t \in [0, T]$. The computational domain Ω is bounded and it is assumed that the functions do not have any singularities. For the description later on, let us define $\boldsymbol{q} := (h, hu, hw)^T$ and

$$\boldsymbol{f_{sw}}(\boldsymbol{q}) := \begin{pmatrix} hu \\ hu^2 + \frac{g}{2}h^2 \\ hwu \end{pmatrix}, \qquad \boldsymbol{s_{sw}}(\boldsymbol{q}) := \begin{pmatrix} 0 \\ -ghb_x - \frac{f_{\mathsf{d}}}{\rho}b_x \\ \frac{f_{\mathsf{d}}}{\rho} \end{pmatrix}, \tag{3.3}$$

$$\boldsymbol{f_{nh}}(p^{nh}, h) := \begin{pmatrix} 0 \\ \frac{1}{\rho}hp^{nh} \\ 0 \end{pmatrix}, \qquad \boldsymbol{s_{nh}}(p^{nh}) := \begin{pmatrix} 0 \\ -\frac{f_{\mathsf{nh}}}{\rho}b_x p^{nh} \\ \frac{f_{\mathsf{nh}}}{\rho}p^{nh} \end{pmatrix}, \tag{3.4}$$

such that we may rewrite the system of equations (3.1)–(3.2) to

$$\boldsymbol{q}_t + \boldsymbol{f_{sw}}(\boldsymbol{q})_x + \boldsymbol{f_{nh}}(p^{nh}, h)_x = \boldsymbol{s_{sw}}(\boldsymbol{q}) + \boldsymbol{s_{nh}}(p^{nh}), \tag{3.5}$$

$$2hw - hu(h+2b)_x = -h(hu)_x. \tag{3.6}$$

For the purpose of shorter notation later on, let us define

$$\boldsymbol{r_{sw}}(\boldsymbol{q}) := -\boldsymbol{f_{sw}}(\boldsymbol{q})_x + \boldsymbol{s_{sw}}(\boldsymbol{q}), \tag{3.7}$$

$$\boldsymbol{r_{nh}}(p^{nh}, h) := -\boldsymbol{f_{nh}}(p^{nh}, h)_x + \boldsymbol{s_{nh}}(p^{nh}) \tag{3.8}$$

to be the right hand side vectors restricted to the non-hydrostatic pressure terms, respectively. Additionally, the divergence constraint (3.6) may be rewritten as

$$\begin{pmatrix} 0 \\ h(\cdot)_x - h(h+2b)_x \\ 2 \end{pmatrix} \cdot \boldsymbol{q} =: \boldsymbol{d} \cdot \boldsymbol{q} = 0. \tag{3.9}$$

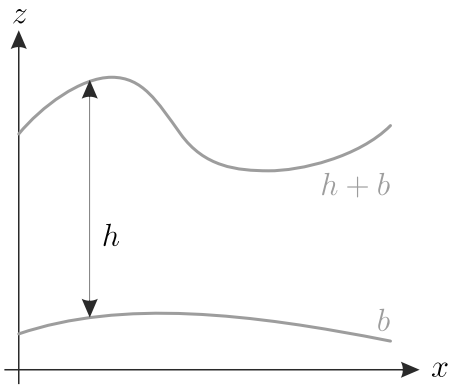

Figure 3.1.: Visualization of the total water depth h with bathymetry b and free surface elevation $h + b$

3.3. Introduction to important numerical methods

This section serves to summarize background knowledge about specific numerical methods that form the basis for the numerical scheme developed in this chapter. The numerical methods presented are projection methods, the Runge-Kutta discontinuous Galerkin (RK-DG) method and the local discontinuous Galerkin (LDG) method.

3.3.1. Projection methods

A projection method forms the main principle for the time discretization of the depth-averaged non-hydrostatic extension for the shallow water equations (3.5)–(3.6). The advantage of considering projection methods for the non-hydrostatic equation set is to solve the non-hydrostatic equation set under the advantageous condition that the algorithm reuses the solution routine for the hydrostatic shallow water equations. Projection methods were introduced by [28, 97]

to numerically solve the incompressible Navier-Stokes equations

$$\boldsymbol{\nabla}_3 \cdot \boldsymbol{V} = 0, \tag{3.10}$$

$$(\boldsymbol{V})_t + \boldsymbol{\nabla}_3 \cdot (\boldsymbol{V}\boldsymbol{V}^T) - \nu \boldsymbol{\nabla}_3 \cdot \boldsymbol{\nabla}_3 \boldsymbol{V} = -\frac{1}{\rho}\boldsymbol{\nabla}_3 P - \boldsymbol{F} \tag{3.11}$$

equipped with Dirichlet boundary conditions and an initial condition. The incompressible Navier-Stokes equations describe the flow of a viscous Newtonian fluid and are the generalization of the incompressible Euler equations of motion (2.1)–(2.2) for viscous fluids with kinematic viscosity ν. The source term $\boldsymbol{F}$ contains external forces, e.g. the gravitational force in equation (2.2). The main challenge for numerical simulations of the incompressible Navier-Stokes equations is the structure of the system of equations. The velocity $\boldsymbol{V}$ and the total pressure P are coupled by the momentum equation (3.11) whereas the pressure is not a dynamical variable of the incompressible Navier-Stokes equations (3.10)–(3.11). Projection methods address this numerical difficulty by splitting the discrete procedure in each time step into three sub-steps. These sub-steps are the predictor step, the solution of an elliptic equation and the corrector step.

The class of projection methods for the incompressible Navier-Stokes equations subdivides into three classes: Pressure-correction schemes, velocity-correction schemes and consistent splitting schemes. Each class is subdivided again according to the properties non-incremental, incremental and rotational incremental. Pressure-correction schemes as well as velocity-correction schemes make direct use of the equations, whereas consistent splitting schemes use the $L^2(\Omega)$-inner product. The difference of pressure-correction and velocity-correction schemes is the information neglected in the predictor, and this choice affects the subsequent two sub-steps, too. Pressure-correction schemes disregard information about the pressure in the predictor whereas velocity-correction schemes disregard information about the velocity in the predictor. The following description restricts to pressure-correction schemes, because it forms the basis of the method presented in this thesis. The choice of pressure-correction schemes is made in order to implement the non-hydrostatic equation set (3.5)–(3.6) that uses the non-hydrostatic pressure. The pressure-correction method is called non-incremental, if the pressure is neglected entirely in the predictor. It is an incremental pressure-correction method, if the predictor includes some amount of information about the pressure. The pressure-correction method is called rotational incremental, if the method is incremental and additionally, the viscosity in the momentum equation (3.11) arises in the solution of the elliptic equation.

An example of time-discrete non-incremental and incremental pressure-correction schemes for the linear Navier-Stokes equations are depicted in tables 3.1 and 3.2. Non-linear terms are dropped for convenience. The information given about the order of accuracy is explained at the end of this section. The time discretization is specified with the implicit Euler scheme in the non-incremental pressure-correction method and the rotational incremental pressure-

Solve for $(\widetilde{\boldsymbol{V}}, P, \boldsymbol{V})^{n+1}$ for all n:	
1. predictor step	$\frac{1}{\Delta t}\left(\widetilde{\boldsymbol{V}}^{n+1} - \boldsymbol{V}^n\right) - \nu \boldsymbol{\nabla}_3 \cdot \boldsymbol{\nabla}_3 \widetilde{\boldsymbol{V}}^{n+1} = \boldsymbol{F}(t^{n+1})$
2. solve elliptic equation	$\frac{1}{\Delta t}\left(\boldsymbol{\nabla}_3 \cdot \widetilde{\boldsymbol{V}}^{n+1}\right) = \frac{1}{\rho}\boldsymbol{\nabla}_3 \cdot \boldsymbol{\nabla}_3 P^{n+1}$
3. corrector step	$\frac{1}{\Delta t}\left(\boldsymbol{V}^{n+1} - \widetilde{\boldsymbol{V}}^{n+1}\right) + \frac{1}{\rho}\boldsymbol{\nabla}_3 P^{n+1} = 0$
convergence order of $\boldsymbol{V}$	1
convergence order of P	0.5

Table 3.1.: Non-incremental pressure-correction scheme for the linear Navier-Stokes equations (3.10)–(3.11) on general domains.

Solve for $(\widetilde{\boldsymbol{V}}, P, \boldsymbol{V})^{n+1}$ for all n:	
1. predictor step	$\frac{1}{2\Delta t}\left(3\widetilde{\boldsymbol{V}}^{n+1} - 4\boldsymbol{V}^n - \boldsymbol{V}^{n-1}\right)$ $-\nu \boldsymbol{\nabla}_3 \cdot \boldsymbol{\nabla}_3 \widetilde{\boldsymbol{V}}^{n+1} + \frac{1}{\rho}\boldsymbol{\nabla}_3 P^n = \boldsymbol{F}(t^{n+1})$
2. solve elliptic equation	$\frac{1}{2\Delta t}\left(3\boldsymbol{\nabla}_3 \cdot \widetilde{\boldsymbol{V}}^{n+1}\right) = \boldsymbol{\nabla}_3 \cdot \boldsymbol{\nabla}_3 \psi^{n+1}$ $\psi^{n+1} = \frac{1}{\rho}(P^{n+1} - P^n) + \nu \boldsymbol{\nabla}_3 \cdot \widetilde{\boldsymbol{V}}^{n+1}$
3. corrector step	$\frac{1}{2\Delta t}\left(3\boldsymbol{V}^{n+1} - 3\widetilde{\boldsymbol{V}}^{n+1}\right) + \boldsymbol{\nabla}_3 \psi^{n+1} = 0$
convergence order of $\boldsymbol{V}$	2
convergence order of P	1.5

Table 3.2.: Rotational incremental pressure-correction scheme for the linear Navier-Stokes equations (3.10)–(3.11) on general domains.

correction method uses the Backward Difference Formula of second order (BDF2). Both time discretizations may be replaced. The predictor step in pressure-correction methods disregards the divergence constraint, such that the predicted velocity $\widetilde{\boldsymbol{V}}^{n+1}$ is not divergence-free. The elliptic equation solves for an updated pressure P^{n+1}. It combines the divergence constraint and the corrector step. The corrector step projects the predicted velocity $\widetilde{\boldsymbol{V}}^{n+1}$ onto the space of divergence-free velocities $\boldsymbol{V}^{n+1}$. For more details of different projection methods, we refer to [18, 56] and the references therein.

A time-discrete pressure-correction method for the non-hydrostatic equation set is shown in table 3.3 as it was used in [60] and similarly in other works [92, 101, 105] considering similar non-hydrostatic equation sets. The differences regarding the non-hydrostatic equation sets themselves are explained in section 2.2.2. The predictor in table 3.3 solves the shallow water

equations augmented with the passive tracer hw. An elliptic equation for the non-hydrostatic pressure is solved, and the corrector updates the predicted horizontal and vertical velocities with non-hydrostatic pressure terms. The projection method is non-incremental as it is common in the literature concerning non-hydrostatic equation sets. Incremental projection methods were not applied to the non-hydrostatic equation sets yet. Therefore, this new derivation will be part of section 3.4 in this thesis.

Solve for $(\widetilde{\boldsymbol{q}}, p^{nh}, \boldsymbol{q})^{n+1}$ for all n:	
1. predictor step	$\frac{1}{\Delta t}\left(\widetilde{\boldsymbol{q}}^{n+1} - \boldsymbol{q}^{n}\right) = \boldsymbol{r_{sw}}(t^{n+1})$
2. solve elliptic equation	$\frac{1}{\Delta t}\left(\boldsymbol{d}^{n+1} \cdot (\widetilde{\boldsymbol{q}}^{n+1})\right) = -\boldsymbol{d}^{n+1} \cdot \boldsymbol{r_{nh}}(p^{nh}, \widetilde{h})^{n+1}$
3. corrector step (only hu, hw)	$\frac{1}{\Delta t}\left(\boldsymbol{q}^{n+1} - \widetilde{\boldsymbol{q}}^{n+1}\right) = \boldsymbol{r_{nh}}(p^{nh}, \widetilde{h})^{n+1}$
convergence order of $\boldsymbol{q}$	1
convergence order of p^{nh}	1

Table 3.3.: Non-incremental pressure-correction scheme for the non-hydrostatic equation set (3.5)–(3.6) on periodic domains.

In the following, major differences in the numerical solution of the incompressible Navier-Stokes equations (3.10)–(3.11) and the depth-averaged non-hydrostatic extension for the shallow water equations (3.5)–(3.6) are explained. These differences are twofold and refer to the relevant pressure term and the elliptic equation. Both differences result from the structure of the continuous equation sets. The Navier-Stokes equations (3.10)–(3.11) consider the total pressure P in the equations, whereas the non-hydrostatic equation set (3.5)–(3.6) splits the total pressure into a hydrostatic and a non-hydrostatic component. The aim is to keep this splitting at the level of discretization in order to reuse the implemented algorithm for the shallow water equations. The non-hydrostatic pressure p^{nh} takes the role of the total pressure P in the corresponding projection method. The different structure of the divergence constraint (3.10) of the Navier-Stokes equations and the divergence constraint (3.6) of the non-hydrostatic equation set leads to different elliptic equations, whereas the elliptic equation resulting from the Navier-Stokes equations is the Poisson equation. The elliptic system in the pressure-correction scheme for the non-hydrostatic equation set is solved as a system of first order equations, as it is explained in section 3.3.3.

The property, if a projection method is incremental, is closely related to the order of approximation. Non-incremental projection methods for the Navier-Stokes equations are first order accurate in the $L^2(\Omega)$-norm of the velocity and accurate with order 0.5 in the $L^2(\Omega)$-norm of the pressure. The reason is an artificial Neumann boundary condition enforced on the pressure. An incremental projection method leads to a second order approximation in the $L^2(\Omega)$-norm of the velocity but only to a first order approximation in the $L^2(\Omega)$-norm of the pressure. In

turn, the reason is another artificial Neumann boundary condition. The rotational incremental projection method keeps the second order approximation in the $L^2(\Omega)$-norm of the velocity, and improves the order in the $L^2(\Omega)$-norm of the pressure to 1.5 for general domains and to 2.0 on periodic domains. In case of vanishing viscosity, the rotational incremental projection method reduces to the incremental projection method. Having this in mind, one aim of this thesis is to derive a second order scheme on the basis of an incremental pressure-correction method for the non-hydrostatic equation set (3.5)–(3.6). The presented scheme will be of second order on periodic domains as well as with Dirichlet boundary data.

3.3.2. Runge-Kutta discontinuous Galerkin methods

The RK-DG method was introduced with arbitrary order of approximation for non-linear hyperbolic conservation laws in a series of papers [30–33, 35] and further developed by others (see references in [34]). The combination of explicit Runge-Kutta time stepping methods and locally-conservative discontinuous Galerkin spatial discretizations leads to numerical schemes that are of high-order and that are able to handle complex geometries, too. The underlying continuous equation sets are usually discretized first in space and second in time.

The roots of the DG method are attributed to [83] on the numerical approximation of the neutron transport equation. The idea behind DG methods is to combine the best ingredients of finite element and finite volume discretization techniques. The finite element world contributes with a Galerkin approach for a weak formulation of the underlying continuous equation sets. It is not taking place on a global level on the entire computational domain, but locally in each computational cell as in finite volume methods. Hence, the resulting global approximation may be discontinuous along cell interfaces and cells are only connected through so-called numerical fluxes. These numerical fluxes have to be defined carefully to reflect the underlying dynamical behavior, but they provide more flexibility to ensure stability. The computation of numerical fluxes is performed at each cell interface and the discontinuity combined with the underlying equation set defines a Riemann problem. This Riemann problem is solved using so-called Riemann solvers (see [99] for an overview). A consequence from the fact that cells are connected only through numerical fluxes is the local character of the method including its local conservation properties. Furthermore, basis functions in each cell are chosen to be polynomials of arbitrary degree similar in (continuous) finite element methods. The mass matrix decomposes into cell mass matrices and is therefore easily invertible. This makes the method highly parallelizable. The possibility to choose different polynomial degrees in each cell makes the method suitable for hp-adaptivity, too. The equation-based details of the derivation of DG methods are part of section 3.5.1 that describes its application to the time-discrete predictor and corrector equations of the non-hydrostatic equation set (3.5)–(3.6). When discretizing in space first, the remaining semi-discrete equations are a system of ordinary

differential equations (ODEs)

$$(\boldsymbol{q}_h)_t = \boldsymbol{r_h}(\boldsymbol{q}_h) \tag{3.12}$$

equipped with initial data, in which $\boldsymbol{q}_h(t)$ is the vector of unknown quantities resulting from $\boldsymbol{q}(t, \boldsymbol{x})$ after discretization in space and $\boldsymbol{r_h}$ is a spatial operator. The ODEs are discretized in time using a Runge-Kutta method. Runge-Kutta schemes [19, 65, 84] are a class of explicit and implicit time-integration methods of general order for ordinary differential equations. In each time step, the equation is solved for a number of s sub-steps (stages), in which intermediate solutions are computed. A special subclass consists of the so-called total-variation diminishing (TVD) [88, 89] or more general strong stability-preserving (SSP) [53] Runge-Kutta methods. These are Runge-Kutta methods aiming at preserving (not increasing) a given norm, e.g. the TVD-norm. They can be rewritten as a convex combination of explicit Euler steps. The SSP RK subclass of Runge-Kutta methods conserve this property, too, under the assumption that the explicit Euler time discretization is (strongly) stable for the given ODE. The rewriting implies conditions on the coefficients of the Runge-Kutta method: For each Runge-Kutta method of order less than four, there is one TVD RK method [89], which is optimal concerning efficiency. SSP RK methods are of advantage for problems with strong shocks and discontinuities, because they do not introduce additional oscillations around the discontinuity. This behavior turns SSP RK methods into the adequate time stepping schemes when using DG methods for solving partial differential equations numerically.
Explicit SSP RK methods with s stages are of the general form [89]

$$\boldsymbol{q}_h^{(0)} = \boldsymbol{q}_h^n, \tag{3.13}$$

$$\boldsymbol{q}_h^{(m)} = \Pi_h \left(\sum_{l=0}^{m-1} \alpha_{ml} \boldsymbol{q}_h^{(l)} + \beta_{ml} \Delta t \boldsymbol{r_h} \left(\boldsymbol{q}_h^{(l)} \right) \right) \quad \text{for } m = 1, ..., s, \tag{3.14}$$

$$\boldsymbol{q}_h^{n+1} = \boldsymbol{q}_h^{(s)}, \tag{3.15}$$

in which $\boldsymbol{q}_h$ is the global vector of degrees of freedom. We choose to apply the explicit second order representative being Heun's method [50] in order to achieve a second order scheme. Heun's method reformulates to

$$\boldsymbol{q}_h^{(0)} = \boldsymbol{q}_h^n, \tag{3.16}$$

$$\boldsymbol{q}_h^{(1)} = \Pi_h \left(\boldsymbol{q}_h^{(0)} + \Delta t \boldsymbol{r_h} \left(\boldsymbol{q}_h^{(0)} \right) \right), \tag{3.17}$$

$$\boldsymbol{q}_h^{(2)} = \Pi_h \left(\boldsymbol{q}_h^{(0)} + \frac{1}{2} \Delta t \left(\boldsymbol{r_h} \left(\boldsymbol{q}_h^{(0)} \right) + \boldsymbol{r_h} \left(\boldsymbol{q}_h^{(1)} \right) \right) \right), \tag{3.18}$$

$$\boldsymbol{q}_h^{n+1} = \boldsymbol{q}_h^{(2)}. \tag{3.19}$$

The Heun scheme combines the trapezoidal rule with an extrapolation at the next time step being a forward Euler step (3.17). The application of the optional slope limiter Π_h in each stage avoids additional oscillations caused by the time-stepping scheme in areas of discontinuities. Therefore, the slope limiter stabilizes the scheme and can be of beneficial use for wetting and drying in the inundation zone. For inundation problems, the method described in the sequel of this chapter applies the velocity based limiter described in [100]. However, in purely wet cases and for smooth solutions, the RK-DG method is not in need of a slope limiter. Concerning stability, the approximate CFL stability constraint is (see [36])

$$\mathrm{CFL} \leq \frac{1}{2k+1}. \tag{3.20}$$

This condition is exact for $k \leq 1$ [33]. For $k \geq 2$, condition (3.20) differs from numerical observed CFL numbers by less than five percent [36].

3.3.3. Local discontinuous Galerkin method for elliptic problems

The LDG method was originally developed [34] as an extension of RK-DG methods for time-dependent non-linear convection-diffusion systems. The main idea is to rewrite these second order systems into larger systems of first order equations that are discretized with the RK-DG method. The term 'local' DG was chosen only to distinguish the scheme from another DG method for parabolic problems being discontinuous in time but not in space.

The treatment of elliptic equations follows the main principle of the LDG method by rewriting the elliptic problem as a system of first order equations being discretized with the DG method. Numerical fluxes need to be chosen carefully in order to obtain a consistent and stable numerical scheme. In RK-DG methods, it is the Riemann solver that determines the numerical fluxes along cell interfaces. The DG method that discretizes the first order system of equations uses a weak formulation that leads to a linear equation system for all unknowns at all degrees of freedom. The details of the derivation are presented in section 3.5.2.

The convergence properties of the LDG method for elliptic equations are important in order to achieve a fully second order scheme. In the literature, convergence properties are usually derived for the Poisson equation $-p_{xx} = f$ equipped with Dirichlet boundary data being the simplest elliptic problem. Rewriting and disregarding the boundary conditions for the moment yields the system of first order equations

$$p_x + u = 0 \qquad \text{on } \Omega, \tag{3.21}$$

$$u_x = f \qquad \text{on } \Omega. \tag{3.22}$$

Therein, the variables p and u are called the *primal variable* and the *flux variable*, respectively. For general domains and the Poisson equation equipped with Dirichlet boundary data, the

primal variable of the Poisson equation will converge with order $k+1$ in the $L^2(\Omega)$-norm, if polynomials of order k are used. This behavior is exactly what we are aiming at. Under the same conditions, the flux variable will converge only with suboptimal order k in the $L^2(\Omega)$-norm [23]. However, the convergence of the flux variable is of optimal order $k+1$, if the computational domain is one-dimensional and under the condition that special numerical fluxes are chosen [20, 24]. In fact, our implementation for the Poisson equation with zero Dirichlet boundary data shows second order of convergence for both the primal and the flux variable. These convergence results are presented in the Appendix in table B.1.

3.4. Pressure-correction method

The pressure-correction method described in this section is based on the background knowledge in section 3.3.1. Present pressure-correction methods for non-hydrostatic equation sets are only of first order of convergence. One aim of this thesis is to introduce a second order convergent discretization of the non-hydrostatic equation set (3.5)–(3.6). The problem of present pressure-correction methods is their non-incremental property as table 3.3 shows. This section derives the semi-discretization of an incremental second order pressure-correction method for the non-hydrostatic extension for shallow water equations (3.5)–(3.6). The first subsection deals with both the first and the third sub-step of the projection method that is the predictor and the corrector step. The second subsection considers the second sub-step that is the solution of the elliptic system of equations. An overview of the algorithm of the second order projection scheme is given at the end of the second subsection.

3.4.1. Predictor and corrector steps

Following [100], the predictor's time stepping is Heun's scheme [50], which is the second order two-stage representative of a standard total-variation diminishing (TVD) Runge-Kutta (RK) method, see subsection 3.5.1 for a detailed explanation. The non-hydrostatic pressure terms in the predictor step should be in compliance with Heun's scheme. The time-discrete corrector step will be chosen accordingly. The consistency errors are denoted with $O(\Delta t^{r+1})$, $r \leq 2$. Let us define

$$\boldsymbol{q}^{eu,n+1} := \boldsymbol{q}^n + \Delta t\, \boldsymbol{r}_{\boldsymbol{sw}}(\boldsymbol{q}^n) + O(\Delta t^2) \tag{3.23}$$

to be a forward Euler step using a time step Δt and the discrete quantity $\boldsymbol{q}^n := \boldsymbol{q}^n(x)$ for all points $x \in \Omega$ at discrete time $t^n := n\Delta t$ at time step n. The quanities of equation (3.5) at

the next time step updated with Heun's scheme may be written as

$$\boldsymbol{h_{sw}} := \boldsymbol{q}^n + \frac{\Delta t}{2}\left(\boldsymbol{r_{sw}}(\boldsymbol{q}^n) + \boldsymbol{r_{sw}}(\boldsymbol{q}^{eu,n+1})\right), \tag{3.24}$$

if non-hydrostatic pressure terms are neglected. We would like to add

$$\frac{\Delta t}{2}\left(\boldsymbol{r_{nh}}((p^{nh},h)^n) + \boldsymbol{r_{nh}}((p^{nh},h)^{n+1})\right) \tag{3.25}$$

to equation (3.24) in order to obtain Heun's scheme in the predictor for the equation (3.5) including non-hydrostatic pressure terms. However, the quantities $(p^{nh})^{n+1}$ and h^{n+1} are not known, when the predictor step is computed. Additionally, the non-hydrostatic pressure is not a dynamical variable of the non-hydrostatic equation set (3.5)–(3.6). This implies that no forward Euler step of the non-hydrostatic pressure is computed in the predictor step, such that it could be used to approximate $(p^{nh})^{n+1}$. Still, it remains possible to add

$$\boldsymbol{h_{nh}} := \frac{\Delta t}{2}\left(\boldsymbol{r_{nh}}((p^{nh},h)^n) + \boldsymbol{r_{nh}}((p^{nh},h)^{ex,n+1})\right) \tag{3.26}$$

to equation (3.24). The expression $(p^{nh})^{ex,n+1}$ denotes an non-hydrostatic pressure that is extrapolated to the next time step $n+1$. We will take care of the actual choice later, and assume a order of consistency r for the extrapolation, meaning

$$(p^{nh})^{ex,n+1} := (p^{nh})^{n+1} + O(\Delta t^{r+1}). \tag{3.27}$$

The quantity $h^{ex,n+1}$ is computed correspondingly. Hence, the time-discrete predictor step including non-hydrostatic pressure terms is

$$\begin{aligned}\widetilde{\boldsymbol{q}}^{n+1} =& \boldsymbol{h_{sw}} + \boldsymbol{h_{nh}} + O(\Delta t^{\min(3,r+2)})\\ =& \boldsymbol{q}^n + \frac{\Delta t}{2}\left(\boldsymbol{r_{sw}}(\boldsymbol{q}^n) + \boldsymbol{r_{sw}}(\boldsymbol{q}^{eu,n+1})\right)\\ &+ \frac{\Delta t}{2}\left(\boldsymbol{r_{nh}}((p^{nh},h)^n) + \boldsymbol{r_{nh}}((p^{nh},h)^{ex,n+1})\right) + O(\Delta t^{\min(3,r+2)}),\end{aligned} \tag{3.28}$$

which is in line with Heun's scheme. The time-discrete corrector step is chosen as

$$\boldsymbol{q}^{n+1} = \widetilde{\boldsymbol{q}}^{n+1} + \Delta t\left(-\boldsymbol{r_{nh}}((p^{nh},h)^{ex,n+1}) + \boldsymbol{r_{nh}}((p^{nh},\widetilde{h})^{n+1})\right) + O(\Delta t^{\min(3,r+2)}) \tag{3.29}$$

in order to correct the error introduced by the choice of extrapolation. Note that the predicted water height $\widetilde{h}^{n+1}$ is not updated in the correction step (3.29), because the continuity equation does not contain any non-hydrostatic pressure terms. Hence, the predicted water height is a

second order approximation to the final water height h^{n+1}, too. This fact does not imply that the water height does not need to be corrected at the end of each time step. A second order scheme requires a correction step for the water height. At the very end of each time step, the computation

$$h^{n+1} = \widetilde{h}^{n+1} + \Delta t \left(\widetilde{(hu)}_x^{n+1} - (hu)_x^{n+1} \right) + O(\Delta t^3), \tag{3.30}$$

of second order accuracy corrects the water height to compensate for the error introduced by the predicted horizontal momentum. This is similar to corrector equation (3.29).

The accuracy of the overall scheme as well as of the predictor step and the corrector step depend on the accuracy of the extrapolation (3.27). Equation (3.29) shows, that a second order consistent extrapolation ($r = 1$) leads to a projection method of second order of convergence. On the contrary, an extrapolation with consistency of first order ($r = 0$) yields a projection method, that is of second order of convergence in all predicted quantities h, hu and hw, but only of first order of convergence in the non-hydrostatic pressure p^{nh}. Results of experimental convergence tests for both cases are visualized in section (3.7.3) and listed in the Appendix in tables B.3 and B.4. Table (3.27) displays a summary of three options to choose the extrapolation including the resulting orders of convergence of the time-discrete predictor and corrector equations.

$(p^{nh})^{ex,n+1}$	total: $\boldsymbol{q}$	total: p^{nh}	projection method	predictor: p^{nh}	corrector: p^{nh}
0	$O(\Delta t)$	$O(\Delta t)$	non-incremental	0	$O(\Delta t)$
$(p^{nh})^n$	$O(\Delta t^2)$	$O(\Delta t)$	incremental	$O(\Delta t)$	$O(\Delta t)$
(3.31)	$O(\Delta t^2)$	$O(\Delta t^2)$	incremental	$O(\Delta t^2)$	$O(\Delta t^2)$

Table 3.4.: Three options to extrapolate the non-hydrostatic pressure at the next time step. These options represent three discretization schemes differing in convergence order.

The minimum accuracy of the predictor step and the corrector step determines the accuracy of the entire scheme. The first option for the extrapolation is trivial and yields a non-incremental projection method of first convergence order. The corrector step with respect to the non-hydrostatic pressure follows the implicit Euler time stepping. The second option is an incremental projection method using an explicit Euler time stepping for non-hydrostatic pressure terms in the predictor and extrapolation of first consistency order in the corrector step. Both schemes suffer from a reduced accuracy in the non-hydrostatic pressure. The third option is the linear extrapolation

$$(p^{nh})^{ex,n+1} := 2(p^{nh})^n - (p^{nh})^{n-1} = (p^{nh})^{n+1} + O(\Delta t^2) \tag{3.31}$$

yielding a projection method that is of second order of convergence in all quantities. This

option replaces the Euler step used in the predictor step for the dynamic variable $\boldsymbol{q}$, such that the predictor step fully respects Heun's scheme. These extrapolations are in line with the insights given in [56] for the Navier-Stokes equations.

3.4.2. Elliptic system of equations

The second sub-step of the projection method for the non-hydrostatic equation set (3.5)–(3.6) is the solution of the elliptic system of time-discrete first order differential equations. The unknowns of this system are the non-hydrostatic pressure and the horizontal momentum at the next time step $n+1$. In projection methods for non-hydrostatic equation sets in the literature (see e.g. [38, 92, 101]), this sub-step contains the solution of an elliptic equation for the non-hydrostatic pressure at the next time step, because the spatial discretizations are finite difference, finite elements and finite volume techniques.

Using DG discretizations, elliptic equations are often rewritten as first order systems (see e.g. [29, 34]). The resulting method is called local discontinuous Galerkin (LDG) method and is explained in detail in subsection 3.5.2. The time-discrete corrector equation (3.29) and the time-discrete divergence constraint

$$\widetilde{h}^{n+1}(hu)_x^{n+1} - (hu)^{n+1}(\widetilde{h}+2b)_x^{n+1} + 2(hw)^{n+1} = 0 \tag{3.32}$$

are rewritten in order to obtain the elliptic system of equations for the non-hydrostatic equation set. The time-discrete corrector equation for the horizontal momentum is rewritten because two different terms including the non-hydrostatic pressure appear in the non-hydrostatic equation set (3.1)–(3.2): The term p^{nh} and the term hp^{nh}. They differ by a factor of the water height h that arises due to Leibniz's integration rule in the derivation (see equation (2.10)). Rewriting and a division by $\widetilde{h}^{n+1}$ eliminates this structural difference to the Poisson equation (3.21)–(3.22). This procedure leads to equation (3.33).

$$\begin{aligned}
&(p^{nh})_x^{n+1} + (\widetilde{h}+f_{\mathsf{nh}}b)_x^{n+1}\frac{(p^{nh})^{n+1}}{\widetilde{h}^{n+1}} + \frac{\rho}{\Delta t}\frac{(hu)^{n+1}}{\widetilde{h}^{n+1}} \\
&\qquad = \frac{\rho}{\Delta t}\frac{\widetilde{(hu)}^{n+1}}{\widetilde{h}^{n+1}} + \frac{((hp^{nh})_x + f_{\mathsf{nh}}b_x p^{nh})^{ex,n+1}}{\widetilde{h}^{n+1}}
\end{aligned} \tag{3.33}$$

$$\begin{aligned}
&(hu)_x^{n+1} + 2f_{\mathsf{nh}}\frac{\Delta t}{\rho}\frac{(p^{nh})^{n+1}}{\widetilde{h}^{n+1}} - (\widetilde{h}+2b)_x^{n+1}\frac{(hu)^{n+1}}{\widetilde{h}^{n+1}} \\
&\qquad = -2\frac{\widetilde{(hw)}^{n+1}}{\widetilde{h}^{n+1}} + 2f_{\mathsf{nh}}\frac{\Delta t}{\rho}\frac{(p^{nh})^{ex,n+1}}{\widetilde{h}^{n+1}}
\end{aligned} \tag{3.34}$$

Inserting the time-discrete corrector equation for the vertical momentum into the time-discrete divergence constraint (3.32) results in equation (3.34), if, in turn, this equation is divided by

$\widetilde{h}^{n+1}$. Hence, the structure regarding the derivatives of the primal and flux variable is the same as the structure of the Poisson equation (3.21)–(3.22). Additional source terms do not complicate the discretization. Therefore, the numerical fluxes in the LDG method [29] for the Poisson equation equipped with Dirichlet boundary conditions can be reused. A derivation of these fluxes is part of section 3.5.3. A summary of the time-discrete algorithm of the pressure-correction scheme for the non-hydrostatic equation set is displayed in table 3.5.

Solve for $(\widetilde{\boldsymbol{q}}, p^{nh}, \boldsymbol{q})^{n+1}$ for all n:	
1. predictor step (3.28)	$\widetilde{\boldsymbol{q}}^{n+1} = \boldsymbol{q}^n + \frac{\Delta t}{2}\left(\boldsymbol{r_{sw}}(\boldsymbol{q}^n) + \boldsymbol{r_{sw}}(\boldsymbol{q}^{eu,n+1})\right)$ $+\frac{\Delta t}{2}\left(\boldsymbol{r_{nh}}((p^{nh}, h)^n) + \boldsymbol{r_{nh}}((p^{nh}, h)^{ex,n+1})\right)$
2. solve elliptic system of equations	$(p^{nh}, hu)^{n+1}$ from (3.33)–(3.34)
3a. corrector step (3.29) for hw	$\boldsymbol{q}^{n+1} = \widetilde{\boldsymbol{q}}^{n+1} - \Delta t\, \boldsymbol{r_{nh}}((p^{nh}, h)^{ex,n+1})$ $+\Delta t\, \boldsymbol{r_{nh}}((p^{nh}, \widetilde{h})^{n+1})$
3b. corrector step (3.30) for h	$h^{n+1} = \widetilde{h}^{n+1} + \Delta t\left(\widetilde{(hu)}_x^{n+1} - (hu)_x^{n+1}\right)$
convergence order of $\boldsymbol{q}$	2
convergence order of p^{nh}	2

Table 3.5.: Incremental pressure-correction scheme for the non-hydrostatic equation set (3.5)–(3.6) on periodic domains as well as with zero Dirichlet boundary data using the extrapolation (3.31).

3.5. Discontinuous Galerkin discretization

All time-discrete components of the projection method are discretized in space with the discontinuous Galerkin (DG) approach. The following two subsections describe the Runge-Kutta DG (RK-DG) approach used for spatial discretization of the time-discrete predictor and corrector equations, and the local discontinuous Galerkin (LDG) method, which is applied to solve the elliptic system of equations (3.33)–(3.34). Introductory descriptions of the RK-DG and the LDG method are given in sections 3.3.2 and 3.3.3.

3.5.1. Runge-Kutta discontinuous Galerkin method

The predictor step is discretized with a second order RK-DG method. RK-DG methods usually discretize the continuous equation set first in space and second in time. However, the time-discrete equations (3.28)–(3.30) are discretized in space in this section. The adjusted order

of description of time and space discretization does not change the properties of the RK-DG method as described in section 3.3.2.
Let I_h be a discretization of the bounded computational domain $\Omega \subset \mathbb{R}$, such that Ω is decomposed into a number of m cells I_i of the same spatial grid size Δx. A weak DG formulation is obtained by multiplying equation (3.5) with smooth test functions

$$\varphi \in \mathcal{V} := \{\varphi \in L_2(\Omega) : \varphi|_{I_i} \in H^1(I_i)\ \forall I_i \in I_h\}. \tag{3.35}$$

For the purpose of shorter notation, let us define the combined flux and source terms in equation (3.28) as

$$\boldsymbol{f} := \frac{1}{2}\left(\boldsymbol{f_{sw}}(\boldsymbol{q}^n) + \boldsymbol{f_{sw}}(\boldsymbol{q}^{eu,n+1})\right), \tag{3.36}$$

$$\begin{aligned}\boldsymbol{s} :=& \frac{1}{2}\left(\boldsymbol{s_{sw}}(\boldsymbol{q}^n) + \boldsymbol{s_{sw}}(\boldsymbol{q}^{eu,n+1}) + \boldsymbol{s_{nh}}(p^{nh})^n + \boldsymbol{s_{nh}}(p^{nh})^{ex,n+1}\right) \\ & - \frac{1}{2}\left(\boldsymbol{f_{nh}}((p^{nh},h)^n) + \boldsymbol{f_{nh}}((p^{nh},h)^{ex,n+1})\right)_x,\end{aligned} \tag{3.37}$$

such that the flux term of the predictor is the same as in the shallow water equations. A rewriting of the time-discrete predictor equations yields

$$\widetilde{\boldsymbol{q}}^{n+1} = \boldsymbol{q}^n + \Delta t\left(-\boldsymbol{f}_x + \boldsymbol{s}\right), \tag{3.38}$$

in which the accuracy term is omitted. A multiplication with test function φ, separate integration over each cell I_i, and integration by parts of the flux term leads to the weak DG formulation

$$\int_{I_i} \widetilde{\boldsymbol{q}}^{n+1}\varphi\,\mathrm{d}x = \int_{I_i} \boldsymbol{q}^n\varphi\,\mathrm{d}x + \Delta t\left(\int_{I_i} \boldsymbol{f}\varphi_x\,\mathrm{d}x - \left[\boldsymbol{f}^*\varphi n_h\right]_{\partial I_i} + \int_{I_i} \boldsymbol{s}\varphi\,\mathrm{d}x\right) \quad \forall\ I_i \in I_h, \tag{3.39}$$

which is valid for all $\varphi \in \mathcal{V}$ and n_h is the outward pointing normal at the boundary of each cell I_i. The interface flux $\boldsymbol{f}^*$ is not defined by default, because the solution is not uniquely defined along interfaces of adjacent cells. This problem is circumvented in the discretization by using the (approximate) solution of the corresponding Riemann problem. The simulations in this thesis apply the Rusanov solver [85, 99]

$$\boldsymbol{f}^*(\boldsymbol{q}) := \boldsymbol{f}^*_{\mathsf{rus}}(\boldsymbol{q}) = \frac{1}{2}(\boldsymbol{f}(\boldsymbol{q}^-) + \boldsymbol{f}(\boldsymbol{q}^+) - l_{\mathsf{max}}(\boldsymbol{q}^+ - \boldsymbol{q}^-)), \tag{3.40}$$

whereas l_{max} is the maximum eigenvalue of $\boldsymbol{f}'(\boldsymbol{q})$ and $\boldsymbol{q}^-$ and $\boldsymbol{q}^+$ denote the values on the left and right side of the discrete function at the cell interface (see definition (3.57)). The Rusanov solver is a cheap approximative linear solver that still ensures good monotonicity properties

and high-order accuracy. In case of the non-linear shallow water equations, the maximum eigenvalue is $l_{\mathsf{max}} = u + \sqrt{gh}$, as well as if the passive tracer hw is taken into account. The linearized shallow water equations have the maximum eigenvalue $l_{\mathsf{max}} = \sqrt{gd}$. In case of the non-hydrostatic equation set, the same maximum eigenvalues are applicable, because all non-hydrostatic pressure terms in the predictor equation are treated as source terms as equations (3.36)–(3.37) show.

The aim of a fully discrete second order scheme leads to the choice of linear polynomials as basis functions with compact support in each cell I_i. This step continues the discretization of the weak DG formulation (3.39). In detail, the basis functions are in the space

$$\mathcal{V}_h := \{\varphi \in L_2(\Omega) : \varphi|_{I_i} \in P_k(I_i)\ \forall I_i \in I_h\} \subset \mathcal{V}, \tag{3.41}$$

where $P_k(I_i)$ denotes the space of polynomials with degree less or equal to k. In this case, it is $k = 1$. A global discontinuous finite element space

$$\mathcal{Q}_h := \bigotimes_{I_i \in I_h} Q_h(I_i) \tag{3.42}$$

is constructed through a direct sum of local finite element spaces $Q_h(I_i)$ on each cell I_i, in which a local Galerkin approach is applied. This approach leads to local continuous finite element solutions

$$(\boldsymbol{q}_h)_i(t^n, x) = (\boldsymbol{q}_h)_i^n(x) = \sum_{j=0}^{k} ((\boldsymbol{q}_h)_i)_j^n \varphi_j(x) \in Q_h(I_i) \qquad \text{for } x \in I_i \tag{3.43}$$

with local vectors of degrees of freedom $(\boldsymbol{q}_h)_i^n(t)$ at time step n and basis functions $\varphi_j \in P_k(I_i)$. The quantity $((\boldsymbol{q}_h)_i)_j^n$ denotes the j-th degree of freedom of the local vector $(\boldsymbol{q}_h)_i^n(t)$. The basis functions φ_j are nodal Lagrange functions [51, 57] with respect to Gauss-Lobatto quadrature points (see e.g. [58]) including the boundary points of each interval, which is helpful for flux computations. These quadrature points reduce to both points on each cell's boundary, if one spatial dimension and linear polynomials are considered. A l-point Gauss-Legendre quadrature (see e.g. [58]) being exact up to polynomials of degree $2l - 1$ is applied for the purpose of potential generalizations to two spatial dimensions, efficiency reasons for higher order schemes and well-balancing. Choosing $\varphi = \varphi_j$ in equation (3.39), this spatial discretization leads to a fully discrete predictor equation for the local vector of degrees of freedom

$$\widetilde{(\boldsymbol{q}_h)_i}^{n+1} = \int_{I_i} \boldsymbol{m}^{-1} (\boldsymbol{q}_h)_i^n \,\mathrm{d}x - \Delta t \Big[\boldsymbol{m}^{-1} \boldsymbol{f}_i^* n_h\Big]_{\partial I_i} + \Delta t \left(\int_{I_i} \boldsymbol{m}_x^{-1} \boldsymbol{f}_i + \boldsymbol{m}^{-1} \boldsymbol{s}_i \,\mathrm{d}x \right), \tag{3.44}$$

which is valid for all cells I_i, and $\boldsymbol{m}^{-1} := \boldsymbol{m}^{-1}(\varphi_j)_j$ with $\boldsymbol{m} = (\boldsymbol{m})_{jl} = \int_{I_i} \varphi_j \varphi_l \, \mathrm{d}x$ denotes the local mass matrix. Equation (3.44) establishes connections among cells I_i through the definition of the numerical interface flux $\boldsymbol{f}_i^*$. In the same manner, the time-discrete correction equations (3.29)–(3.30) are discretized in space with the DG method. The resulting discretization of the corrector equations for the vertical momentum is

$$((hw)_h)_i^{n+1} = \int_{I_i} \boldsymbol{m}^{-1} \widetilde{((hw)_h)_i}^{n+1} + \boldsymbol{m}^{-1} \Delta t \frac{f_{\mathsf{nh}}}{\rho} \left(((p^{nh})_h^{n+1})_i - ((p^{nh})_h^{ex,n+1})_i \right) \mathrm{d}x. \quad (3.45)$$

Note that the correction step for the horizontal momentum is included in the elliptic system of equations (3.33)–(3.34). The discretized correction of the water height is

$$\begin{aligned} (h_h)_i^{n+1} = &\int_{I_i} \boldsymbol{m}^{-1} \widetilde{(h_h)_i}^{n+1} - \boldsymbol{m}_x^{-1} \Delta t \left(\widetilde{((hu)_h)_i}^{n+1} - ((hu)_h)_i^{n+1} \right) \mathrm{d}x \\ &- \left[\boldsymbol{m}^{-1} \Delta t \left(\widetilde{((hu)_h)_i}^{n+1} - ((hu)_h)_i^{n+1} \right)^* n_h \right]_{\partial I_i} \quad \forall \; I_i \in I_h, \end{aligned} \quad (3.46)$$

whereas $(h_h)_i$ is the local vector of degrees of freedom in each cell I_i and $()^*$ denotes the numerical flux at cell interfaces. The numerical flux is computed with the Rusanov solver (3.40) used in the predictor. The corresponding values for the water height and the vertical momentum, that are needed to compute the numerical flux, are the predicted water height, and a zero vertical momentum, because equation (3.46) uses the first component of the flux computation only.

3.5.2. Local discontinuous Galerkin method

The elliptic system of equations (3.33)–(3.34) is solved with the local discontinuous Galerkin (LDG) method. A short description is given in section 3.3.3, in which the convergence properties are mentioned to be of second order for the one-dimensional problem. The elliptic system of equations (3.33)–(3.34) is a system of linear equations with respect to the unknowns $(hu, p^{nh})^{n+1}$ with non-linear and non-constant coefficients. In each time step, a linear equation system is constructed using the LDG method for both unknowns at all degrees of freedom. This system of size $2m(k+1)$ is solved by means of a restarted GMRES algorithm for sparse matrices.

This subsection presents the derivation of the LDG method with a focus on the stability of numerical fluxes used for three types on boundary conditions. Derivations of how to include Dirichlet boundary data for the simple elliptic problem being the Poisson equation discretized with the LDG method is given in [22, 29]. We follow the description, correct some sign mistakes and extend it twofold: To a general elliptic system of equations with the shape as the elliptic system of equations (3.33)–(3.34) and to periodic and reflecting boundary conditions,

if possible. The case of Poisson's equation is treated, too. We restrict the analysis of the elliptic system of equations to the case of constant bathymetry, because the more involved analysis for the case of non-constant bathymetry is not in the scope of this thesis. However, numerical tests on non-constant bathymetry are presented in section 3.7 and show appropriate and especially stable results. In order to simplify the notation, let us define a more general elliptic system of equations

$$p_x + g_1 p + h_1 u = f_1 \qquad \text{on } \Omega, \tag{3.47}$$
$$u_x + h_2 p + g_2 u = f_2 \qquad \text{on } \Omega \tag{3.48}$$

for the pressure $p \in H^1(\Omega)$ and the velocity $u \in H^1(\Omega)$ with functions f_i, $i = 1, 2$, on the right hand side. The coefficients are functions $g_i = g_i(x)$ and $h_i = h_i(x)$. The *model system* (3.47)–(3.48) is discretized in space with a DG approach. Hence, the requirement on the functions is $f_i, g_i, h_i \in L^2(\Omega)$ for $i = 1, 2$. The model system (3.47)–(3.48) can serve to describe both the elliptic system of equations (3.33)–(3.34) and the Poisson equation (3.21)–(3.22), if we assume relevant structure properties for its coefficients. The structure properties are displayed in table 3.6. Note that the condition $g_1 + g_2 = 0$ and $h_1 > 0$ is true in case of both specifications of the model system (3.47)–(3.48). In both cases, three types of boundary data are considered: Dirichlet data, periodic and reflecting boundary conditions. The

system of equations	$g_1 + g_2$	h_1	h_2
Poisson (3.21)–(3.22)	0	1	0
non-hydrostatic $b_x = 0$ (3.33)–(3.34)	0	> 0	> 0

Table 3.6.: Specified structure properties of the model system (3.47)–(3.48).

entire problem of defining the LDG method for a specific set of equations including boundary conditions reduces to the problem of finding appropriate numerical fluxes that lead to a stable algorithm and a uniquely defined solution. This is common in all DG methods, as numerical fluxes appear by reason of the local Galerkin approach in each cell and the global solution is not uniquely defined at inner cells interfaces and at the boundary. A weak formulation forms the start of the derivation of the numerical scheme. The model system (3.47)–(3.48) is multiplied with a test function $\varphi \in \mathcal{V}$ (see equation (3.35)) and the equations are integrated over each cell I_i separately. Integration by parts in order to transfer the derivative to the test function

leads to the weak formulation to find $p_h, u_h \in \mathcal{V}_h$ (see equation (3.41)), such that

$$\int_{\partial I_i} \hat{p}_h \varphi n_h \, ds + \int_{I_i} -p_h \varphi_x + g_1 p_h \varphi + h_1 u_h \varphi \, dx = \int_{I_i} f_1 \varphi \, dx, \tag{3.49}$$

$$\int_{\partial I_i} \hat{u}_h \varphi n_h \, ds + \int_{I_i} -u_h \varphi_x + h_2 p_h \varphi + g_2 u_h \varphi \, dx = \int_{I_i} f_2 \varphi \, dx, \tag{3.50}$$

which is valid for all $\varphi \in \mathcal{V}$ and all cells I_i. The variables $\hat{p}_h$ and $\hat{u}_h$ denote the numerical fluxes that need to be defined along inner cell interfaces and at the boundary. Instead of taking $\varphi \in \mathcal{V}$, the Galerkin approach is completed by taking $\varphi \in \mathcal{V}_h \subset \mathcal{V}$. Inserting of $\varphi = u_h$ in the first equation and $\varphi = p_h$ in the second equation results after a summation of both equations in

$$\Theta_{i,h} + \int_{I_i} h_1 u_h^2 + h_2 p_h^2 + (g_1 + g_2) p_h u_h \, dx = \int_{I_i} f_1 u_h + f_2 p_h \, dx \tag{3.51}$$

with

$$\Theta_{i,h} := \int_{\partial I_i} \hat{p}_h u_h n_h + \hat{u}_h p_h n_h - p_h u_h n_h \, ds, \tag{3.52}$$

for which another step of integration by parts is conducted. A summation over all cells and an application of the property $g_1 + g_2 = 0$ result in

$$\Theta_h + \sum_{I_i} \int_{I_i} h_1 u_h^2 + h_2 p_h^2 \, dx = \sum_{I_i} \int_{I_i} f_1 u_h + f_2 p_h \, dx \tag{3.53}$$

with

$$\Theta_h := \sum_{i=1}^{m} \Theta_{i,h}. \tag{3.54}$$

In order to define suitable numerical fluxes, this weak formulation is compared to its analytical counterpart. Hence, the first equation of the model system (3.47)–(3.48) is multiplied by u and the second equation by p. Integration over the domain Ω and a summation of both resulting equations yields

$$\int_{\Omega} p_x u + u_x p + h_1 u^2 + h_2 p^2 + (g_1 + g_2) p u \, dx = \int_{\Omega} f_1 u + f_2 p \, dx, \tag{3.55}$$

$$=> \int_{\partial\Omega} p u n_h \, ds + \int_{\Omega} h_1 u^2 + h_2 p^2 \, dx = \int_{\Omega} f_1 u + f_2 p \, dx, \tag{3.56}$$

for which, in turn, the property $g_1 + g_2 = 0$ and integration by parts is applied. The result of the numerical derivation (3.53) and the result of the analytical derivation (3.56) are similar and it is possible to extract two criteria on numerical fluxes:

1. The first criterion is necessary to ensure stable numerical fluxes along inner cell interfaces and at the boundary, denoted by the terms *inner numerical fluxes* and *numerical boundary fluxes*. This is expressed in the requirement $\Theta_h \geq \int_{\partial\Omega} pun_h \, ds$.

2. The second criterion on the numerical fluxes shall guarantee an existent unique discrete solution for the model system (3.47)–(3.48). This model system is linear. Thus, setting $f_1 = f_2 = 0$ in equation (3.53) should imply $p_h = u_h = 0$ on Ω.

3.5.3. Numerical fluxes for the LDG method

The fulfillment of both criteria above continues with the definition of inner numerical fluxes and with the deduction of two constraints for numerical boundary fluxes. We set the inner numerical fluxes (following [29, 34]) to be the same for Dirichlet, periodic and reflecting boundary conditions. Therefore, the first criterion reduces to a constraint for numerical boundary fluxes. Similarly, the second criterion is reduced to a second constraint afterwards. The combination of both constraints together with possible boundary conditions and model system specifications is considered in subsequent subsections.

At (inner) cell interfaces $e = \overline{\partial I_i} \cap \overline{\partial I_j}$ with $i \neq j$ and $I_i, I_j \in I_h$, let us define averages and jumps of the global discontinuous solution using the notations

$$[\![u_h]\!] := u_h^- - u_h^+, \qquad \{u_h\} := \frac{1}{2}(u_h^- + u_h^+), \qquad u_h^\pm(x) := \lim_{\epsilon \to 0} u_h(x \pm \epsilon), \qquad \forall x \in \mathcal{E}_h, \tag{3.57}$$

whereas $\mathcal{E}_h$ and $\mathcal{E}_{h,in}$ denote the set of cell interfaces (including boundary edges) and the set of inner cell interfaces, respectively. A rewriting of Θ_h yields

$$\begin{aligned}
\Theta_h =& \sum_{e \in \epsilon_h} \int_e [\![\hat{p}_h u_h + \hat{u}_h p_h - p_h u_h]\!] \, ds \\
=& \sum_{e \in \epsilon_{h,in}} \int_e \hat{p}_h [\![u_h]\!] + \hat{u}_h [\![p_h]\!] - [\![p_h u_h]\!] \, ds + \int_{\partial\Omega} \hat{p}_h u_h n_h + \hat{u}_h p_h n_h - p_h u_h \, ds \\
=& \sum_{e \in \epsilon_{h,in}} \int_e (\hat{u}_h - \{u_h\})[\![p_h]\!] + (\hat{p}_h - \{p_h\})[\![u_h]\!] \, ds + \int_{\partial\Omega} p_h(\hat{u}_h - u_h) n_h + \hat{p}_h u_h n_h \, ds \\
=:& \Theta_{h,in} + \Theta_{h,ou}.
\end{aligned} \tag{3.58}$$

The choice of $\Theta_{h,in} \geq 0$ helps to ensure the first criterion $\Theta_h \geq \int_{\partial\Omega} pun_h \, ds$. This choice is satisfied by defining (following [29, 34])

$$\hat{u}_h := \{u_h\} + c_{11}[\![p_h]\!] + c_{12}[\![u_h]\!] \qquad \text{on } \mathcal{E}_{h,in}, \tag{3.59}$$

$$\hat{p}_h := \{p_h\} - c_{12}[\![p_h]\!] + c_{22}[\![u_h]\!] \qquad \text{on } \mathcal{E}_{h,in}, \tag{3.60}$$

where $c_{11}, c_{22} \geq 0$. With respect to the parameter c_{12}, these inner numerical fluxes (3.59)–(3.60) mean that upwind fluxes for both u and p are taken, but in opposite directions. This is essential for stability. The parameters c_{11} and c_{22} are introduced to further stabilize the scheme. The parameter c_{11} serves to penalize jumps in p and can be thought to be an artificial dissipation coefficient, when rewriting the DG scheme as a mixed finite element method [29]. A unified analysis of different DG methods including mixed finite elements is shown in [4]. A comparison of performance is given in [21]. The parameter c_{22} is usually set to zero in the LDG method ([22, 34]), as the discussion in the subsections treating boundary conditions shows. With the definitions above in mind, two constraints on $\Theta_{h,ou}$ are deduced:

1. The first criterion yields the first constraint

$$\Theta_{h,ou} = \int_{\partial\Omega} p_h(\hat{u}_h - u_h)n_h + \hat{p}_h u_h n_h \, ds \geq \int_{\partial\Omega} pun_h \, ds. \tag{3.61}$$

2. The second criterion considers equation (3.53) with $f_1 = f_2 = 0$. The definition of inner numerical fluxes leads to

$$\sum_{e \in \epsilon_{h,in}} \int_e c_{22}[\![u_h]\!]^2 + c_{11}[\![p_h]\!]^2 + \Theta_{h,ou} + \sum_{I_i} \int_{I_i} h_1 u_h^2 + h_2 p_h^2 \, dx = 0. \tag{3.62}$$

   If it is possible to conclude $p_h = 0$ and $u_h = 0$ on the entire domain Ω, the discrete solution is existent and unique. This is the second constraint on $\Theta_{h,ou}$.

Both constraints are treated in the subsections. The subsections are devoted to the definition of numerical boundary fluxes for three kinds of boundary conditions being Dirichlet boundary data, periodic and reflecting boundary conditions, combined with both the Poisson equation (3.21)–(3.22) and the elliptic system of equations (3.33)–(3.34). In summary, Poisson's equation (3.21)–(3.22) allows numerical boundary fluxes for Dirichlet boundary data but not for periodic and reflecting boundary conditions. However, the elliptic system of equations (3.33)–(3.34) allows for suitable numerical fluxes for all three types.

3.5.3.1. Dirichlet boundary

This case is shown in [29] for the Poisson equation and repeated here. In case of a zero Dirichlet boundary, we know $p = 0$ on $\partial\Omega$. Therefore, it is $\int_{\partial\Omega} pun_h \, ds = 0$ and the definition of numerical fluxes

$$\hat{u}_h := u_h + c_{11} p_h n_h \qquad \text{on } \partial\Omega, \tag{3.63}$$

$$\hat{p}_h := 0 \qquad \text{on } \partial\Omega, \tag{3.64}$$

reduces the first constraint (3.61) to $\Theta_{h,ou} = \int_{\partial\Omega} c_{11} p_h^2 \, ds \geq 0$. Hence, the first constraint is fulfilled for both specifications of the model system.

The second constraint yields $u_h = 0$ on Ω, $[\![p_h]\!] = 0$ on $\mathcal{E}_{h,in}$ and $p_h = 0$ on $\partial\Omega$ for Poisson's equation ($h_1 = 1$, $h_2 = 0$). It does not yield all information needed. This is independent of the choice of c_{22}, which allows to take $c_{22} = 0$ to reduce the amount of computational work. Equation (3.21) in its weak formulation in each cell I_i helps to obtain more information in order to get the second constraint satisfied. It yields

$$\int_{I_i} (p_h)_x \varphi + h_1 u_h \varphi \, dx = 0 \quad \forall \varphi \in P_k(I_i), \tag{3.65}$$

and with the information $u_h = 0$ on Ω, it is

$$\int_{I_i} (p_h)_x \varphi \, dx = 0 \quad \forall \varphi \in P_k(I_i). \tag{3.66}$$

We conclude $(p_h)_x = 0$ on Ω because φ, $(p_h)_x \in P_k(I_i)$. Knowing $p_h = 0$ on $\partial\Omega$ yields $p_h = 0$ on Ω.

In case of the elliptic system of equations (3.33)–(3.34), the second constraint is fulfilled even without this extra argument, because $h_2 > 0$. Therefore, stable numerical fluxes lead to a stable numerical scheme for both equations. The choice for the parameters is $c_{22} = 0$ and $c_{11} = c_{12} = 1$.

3.5.3.2. Periodic boundary

Periodic boundaries are characterized by the condition that p and u are equal on both sides of $\partial\Omega$, and thus, it is $\int_{\partial\Omega} pun_h \, ds = 0$. We choose numerical boundary fluxes to be the same as the inner numerical fluxes (3.59)–(3.60). Hence, the integral $\Theta_{h,ou}$ does not appear in equation (3.58), and $\Theta_{h,ou} := 0$. Therefore, the first constraint (3.61) is fulfilled for both specifications of the model system.

The second constraint (3.62) yields $[\![p_h]\!] = 0$ on $\mathcal{E}_{h,in}$ and $u_h = 0$ on Ω, providing $c_{11} > 0$ and $c_{22} = 0$ as before. In case of the elliptic system of equations (3.33)–(3.34), its property

$h_2 > 0$ allow the conclusion $p_h = 0$ on Ω and the second constraint is fulfilled. In contrast, the Poisson equation (3.21)–(3.22) defines the coefficient $h_2 = 0$ and the boundary flux term $\Theta_{h,ou}$ is missing, such that it is not possible to conclude $p_h = 0$ on Ω. The help of the extra argument gained from (3.66) does not improve the situation, because the exact value of p_h on the boundary is missing. Another choice of c_{22} doesn't solve the problem either. Therefore, periodic boundaries are not suitable for the Poisson equation. The choice for the parameters is the same as in case of Dirichlet boundary conditions.

3.5.3.3. Reflecting boundary

A physically reasonable definition of a reflecting boundary is a pressure behaving in the same way as the water height, i.e. it accumulates at the wall, and the velocity changes its direction during reflection. The corresponding definition of numerical boundary fluxes would be

$$\hat{u}_h := -u_h \qquad \text{on } \partial\Omega, \tag{3.67}$$

$$\hat{p}_h := p_h \qquad \text{on } \partial\Omega. \tag{3.68}$$

But this leads to the constraint $\Theta_{h,ou} = -\int_{\partial\Omega} p_h u_h n_h \, ds \geq -\int_{\partial\Omega} p u n_h \, ds$, which is not always fulfilled and these numerical boundary fluxes do not lead to a stable numerical solution. Hence, it may be worth to take the velocity to be zero at the at wall, while the pressure still accumulates. The corresponding numerical boundary fluxes are

$$\hat{u}_h := 0 \qquad \text{on } \partial\Omega, \tag{3.69}$$

$$\hat{p}_h := p_h \qquad \text{on } \partial\Omega, \tag{3.70}$$

which results in a fulfilled first constraint $\Theta_{h,ou} \geq \int_{\partial\Omega} p u n_h \, ds$, because both terms vanish. Therefore, these numerical boundary fluxes lead to stable numerical solutions for both systems of equations.

The second constraint holds only for the elliptic system of equations (3.33)–(3.34), but not in case of the Poisson equation (3.21)–(3.22) by using the same argumentation given for periodic boundary conditions. The choice for the parameters is the same as in case of Dirichlet boundary conditions.

3.6. Implementation details

This section deals with important details about the implementation as the setup of convergence tests and the inundation treatment. These informations prepare the presentation of numerical results in the next section.

3.6.1. Convergence tests

There are two common strategies to conduct convergence tests for numerical methods for partial differential equations. Both are visualized in figure 3.2 for hyperbolic equations. Therein, each dot represents a simulation run using a specific combination of step sizes Δt and Δx. The first strategy is to use a constant CFL number, and both Δt and Δx are cut by half within each refinement step. The second strategy needs two tests with fixed spacial grid size Δx or fixed time step Δt, such that the accuracy of the time stepping or space discretization are studied separately, respectively. In this case, the non-fixed step size is reduced by half. Of course, the CFL condition needs to be respected to avoid unstable simulation runs. The fixed step size need to be very small, such that the corresponding constant consistency error is small compared to the splitting and discretization error under study and its influence on the experimental order of convergence is negligible.

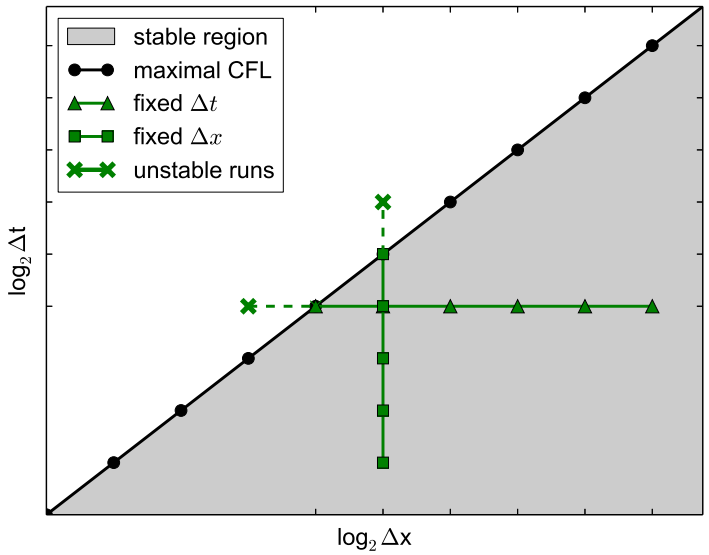

Figure 3.2.: CFL number inspection for two strategies for convergence tests: The first strategy (black) uses a constant maximal CFL number. The second strategy (green) aims at conducting tests for time discretization and space discretization individually, whereas the stability condition needs to be respected. Simulation runs (dots, squares, triangles, crosses) are displayed as a specific combination of step sizes Δt and Δx.

However, there are some disadvantages coming with the latter strategy: First, there is always the question of what choice of fixed step size is small enough, and this choice needs to be done very carefully. Second, the second strategy seems to be more advantageous mainly

because of efficiency reasons. In case of studying convergence to the complete equation set, this is misleading as very small step sizes and two separate runs are needed. Therefore, we choose the first strategy and conduct convergence tests with constant CFL number.

Besides the set up of the convergence test, the reference solution is to be defined as well. If an analytical solution of the underlying continuous set of equations is known, it can serve as the reference solution. However, this information is not available in many cases. Hence, the convergence tests is conducted with respect to a finest numerical solution, which is a numerical solution with finer resolution than of all other simulation runs considered. On the other hand, the convergence test with respect to the finest numerical solution is less significant, because this convergence implies that the numerical model is convergent to some discrete equations, but it may be not convergent to the set of analytical equations or the order of convergence may be reduced.

In case of the system of equations (3.5)–(3.6), the equivalence provides analytical solutions on constant bathymetry using the quadratic vertical profile (see section 2.3). This equivalence is applicable in the conservative formulation (3.5)–(3.6), too, because it is equivalent to the primitive formulation (2.23)–(2.26) if the solutions are smooth. All analytical solutions considered in this thesis fulfill this property. Convergence tests of the numerical model are conducted on constant bathymetry only. The validation including non-constant bathymetry is left to sections 3.7.5–3.7.7.

Let the reference solution q_{ref} be one of the unknown quantities in the non-hydrostatic equation set (3.5)–(3.6). The experimental error of one simulation run with m cells is computed compared to a reference solution q_{ref} with respect to the $L^2(\Omega)$-norm and the $L^\infty(\Omega)$-norm. It is evaluated at a specific time t^{test} on the entire domain. The accuracy of the time discretization is taken into account through implicit accumulation over time. The experimental error is

$$e_m = \|q_m^{n_{\mathsf{test}}(m)} - q_{\mathsf{ref}}(t^{\mathsf{test}})\|, \tag{3.71}$$

in which $q_m^{n_{\mathsf{test}}(m)}$ is the discrete solution of the quantity q_{ref} obtained by a simulation run using m cells at time step $n_{\mathsf{test}}(m)$. This time step is a function of the total number m of cells, because each simulation run has the same CFL number. The discrete solution $q_m^{n_{\mathsf{test}}(m)}$ and the reference solution $q_{\mathsf{ref}}(t^{\mathsf{test}})$ at time step $n_{\mathsf{test}}(m)$ are prolongated to a finer spatial grid in equation (3.71). This finer grid is the finest grid in the convergence study. The error norm $\|\cdot\|$ is chosen among the discrete $L^2(\Omega)$- and $L^\infty(\Omega)$-norms. Let m_c and m_f be two different total numbers of cells and $(\Delta_x)_c$ and $(\Delta_x)_f$ their spatial resolutions, respectively. The experimental order of convergence of the corresponding simulation runs is

$$\gamma_{m_f}^{m_c} = \frac{\mathsf{log}(e_{m_c}/e_{m_f})}{\mathsf{log}((\Delta_x)_c/(\Delta_x)_f)}. \tag{3.72}$$

If the discretization scheme is convergent and the total number of cells is increased, whereas

the fraction $\frac{m_f}{m_c}$ and the CFL number are constant, the experimental order of convergence shows the correct convergence order. The definitions above serve to describe the results of the experimental convergence tests in section 3.7.

3.6.2. Inundation treatment

The wet-dry treatment in the non-hydrostatic model is build upon the wetting and drying limiter of the predictor described in [100]. The limiter is applied in in each Runge-Kutta stage (see equations (3.13)–(3.15)). The inundation scheme considers a fixed grid method. The crucial part is the determination of dry and wet cells in the computational domain. A newly computed water height calculated on the basis of the water height and the horizontal momentum serves as a criterion to determine locations where to set the horizontal momentum to zero. If the newly computed water height at one degree of freedom in a cell is below a given wet-dry tolerance, the horizontal momentum is set to zero throughout the cell.

A local version of the non-hydrostatic model helps to solve the elliptic system of equations (3.33)–(3.34) in completely wet cells only. Therefore, the local approach assures the regularity of the matrix of the linear equation system. The predictor is still solved on the entire computational domain. Hence, an inundation procedure is possible although dry cells in the non-hydrostatic model are excluded. The boundary conditions for the local wet area are considered to be zero Dirichlet data, as it is done in the predictor for the entire computational domain. More details about the local version of the non-hydrostatic extension for shallow water equations are the topic of chapter 4 of this work.

The non-hydrostatic model needs two further adjustments in order to be suitable for inundation problems. The vertical momentum is set to zero in the predictor step along with the horizontal momentum according to the same wet-dry criterion. Additionally, the limiter is applied in turn to guarantee limited quantities at the end of each time step. The wet-dry tolerance is constant during the time of simulation and is set to 10^{-8}.

3.7. Numerical results

The validation of the numerical model uses test cases with known analytical solution, convergence tests with respect to analytical solutions, and laboratory data. The gravitational acceleration constant is set to $g = 9.80616\,\mathrm{m/s^2}$. The descriptions for the linear standing wave test and the propagating solitary wave test are adapted while mainly following [60, 61]. The results on constant bathymetry presented therein are in line with those presented in this section.

3.7.1. Periodic standing wave

The analytical solution for the linear standing wave test according to section 2.4.3.1 is adapted to one spacial dimension and to the conservative formulation. This analytical solution for the linearized version non-hydrostatic equation set (3.5)–(3.6) is

$$h(x,t) = d - a\sin(\kappa x)\cos(\kappa ct)\,, \tag{3.73}$$
$$hu(x,t) = ac\cos(\kappa x)\sin(\kappa ct)\,, \tag{3.74}$$
$$hw(x,t) = -\frac{d}{2}(hu)_x = \frac{a}{2}dc\kappa\sin(\kappa x)\sin(\kappa ct)\,, \tag{3.75}$$
$$p^{nh}(x,t) = \frac{d}{f_{\text{nh}}}(hw)_t = \frac{a}{2f_{\text{nh}}}d(c\kappa)^2\sin(\kappa x)\cos(\kappa ct)\,. \tag{3.76}$$

In different simulation runs, we vary the water depth d while keeping the wave length $\lambda = \frac{2\pi}{\kappa} = 20\,\text{m}$ and the maximal amplitude $a = 0.01\,\text{m}$ constant to get ratios for $\frac{d}{\lambda}$ between 0.05 and 1.0, and ratios for $\frac{a}{d}$ between 0.01 and 0.005, respectively. The computational domain

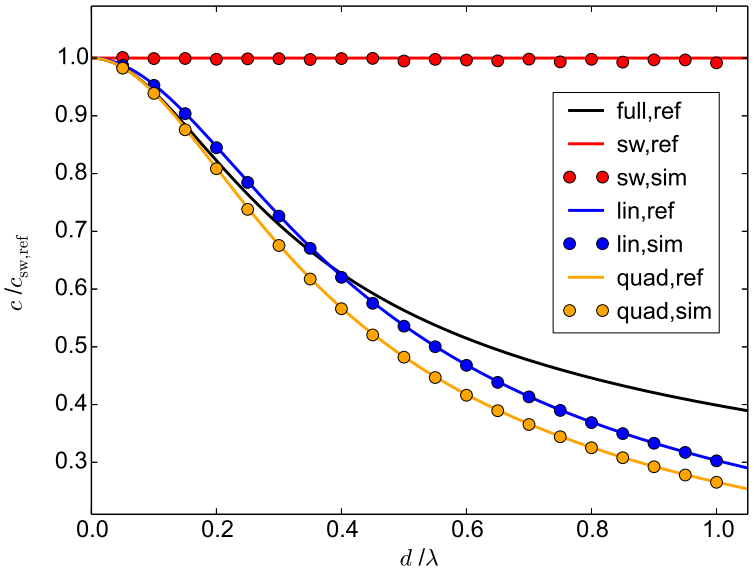

Figure 3.3.: Periodic standing wave: Comparison of simulated hydrostatic and non-hydrostatic phase velocities with analytic reference values for all simulations.

is divided into $m = 80$ cells and a time step of $\Delta t = 0.0075\,\text{s}$ is used. This sets the CFL number to CFL ≈ 0.3 (see equation (3.20)) for the run with largest depth and also highest phase speed. The simulation time is chosen long enough to measure one wave period. We impose periodic boundary conditions on a grid length of one wave length. Furthermore, zero

Dirichlet boundary conditions are also possible. The results are the same and therefore not shown here. For a longer simulation time of 50 seconds, figure 3.4 shows a time series of the surface elevation for both the linear and the quadratic vertical pressure profile evaluated at a specific grid point whereas a ratio of depth to wavelength of 0.5 is employed. The numerical computations yield accurate evolutions of the water height for both pressure profiles compared with the corresponding analytical evolutions. The resulting normalized phase velocities for the shallow water model and the non-hydrostatic equation set with either the linear or the quadratic vertical pressure are displayed in figure 3.3. Furthermore, they are compared to their analytical reference phase velocities and the full reference phase velocity as derived in section 2.4.1. All numerical dispersion relations match the corresponding analytical ones precisely.

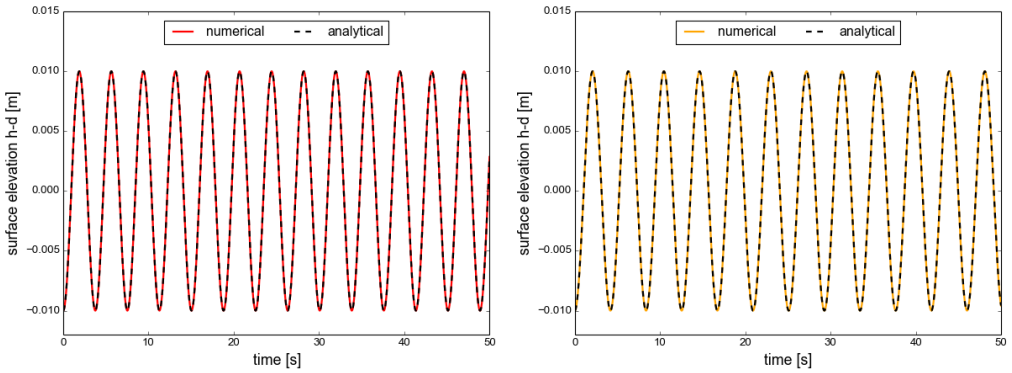

Figure 3.4.: Periodic standing wave: Comparison of the simulated (colored) and analytical (black dashed) surface elevation with linear (left) and quadratic (right) vertical profile for a propagation time of 50 seconds at location $x = 5$m with 80 cells and $\frac{d}{\lambda} = 0.5$.

3.7.2. Periodic solitary wave

This test considers the analytical propagating solitary wave solution according to equation (2.48)–(2.52) with the ratio $\frac{a}{d} = 0.2$, a constant depth $d = 10\,\text{m}$ and displacement $x_0 = l/4$ on a domain of length $l = 800\,\text{m}$. The one-dimensional analytical solution for conservative variables is

$$h(x,t) = d + a\cosh^{-2}(K(x - ct - x_0)), \tag{3.77}$$
$$hu(x,t) = c\,(h(x,t) - d), \tag{3.78}$$
$$hw(x,t) = -0.5h(x,t)(hu)_x(x,t), \tag{3.79}$$
$$th(x,t) := \tanh(K(x - ct - x_0)). \tag{3.80}$$
$$p^{nh}(x,t) = (cdK)^2\frac{h(x,t) - d}{h(x,t)f_{\text{nh}}}\left(2d\frac{th(x,t)}{h(x,t)} - \frac{h(x,t) - d}{a}\right), \tag{3.81}$$

A reasonable choice for boundary conditions are zero Dirichlet boundary data, at least as long as the wave is no approaching the boundary. These results are the same (not shown) as the results below. We impose periodic boundary conditions on the computational domain in order to test our model's behavior during longer simulation times without enlarging the computational domain much. Thus, we assume that essentially non-periodic solitary wave solution is periodic on the given computational domain. If it is large enough to cover most important parts of the solitary wave, only small errors are introduced that do not disturb the solution as shown in figure 3.5. Results of convergence tests are presented in section 3.7.3. The simulation time is 50 seconds. The total number of cells is $m = 200$ and the time step is $\Delta t = 0.1\,\text{s}$ resulting in a CFL number of 0.27. Figure 3.5 compares our numerical computations with the analytical solution at different simulation times. The numerical result using the quadratic pressure profile shows a very good agreement with the analytical solution. In contrast, the application of the linear pressure profile yields a threefold mismatch arising from the inconsistency in initial conditions with the underlying equation system: Small amplitude waves propagate to the opposite direction, the wave height increases because of weaker dispersion of the linear profile, and trailing waves start to establish. In [92, 101, 105], different solitary waves are computed with non-hydrostatic models using the traditional linear vertical pressure profile. Therein, these mismatches are also visible, except that their amplitudes tend to diminish than to amplify. Their aim to compute the solitary waves was merely to show that non-hydrostatic models produce similar results as Boussinesq-type models.

The result shown in figure 3.5 is consistent with the analysis in section 2.4.3.2. It was observed that the linear pressure profile causes the maximal amplitude to be increased and the length of the solitary wave to be diminished, while an embryo of a secondary wave system is apparent at the rear end. It should be noted that the wave is still evolving at the last time shown.

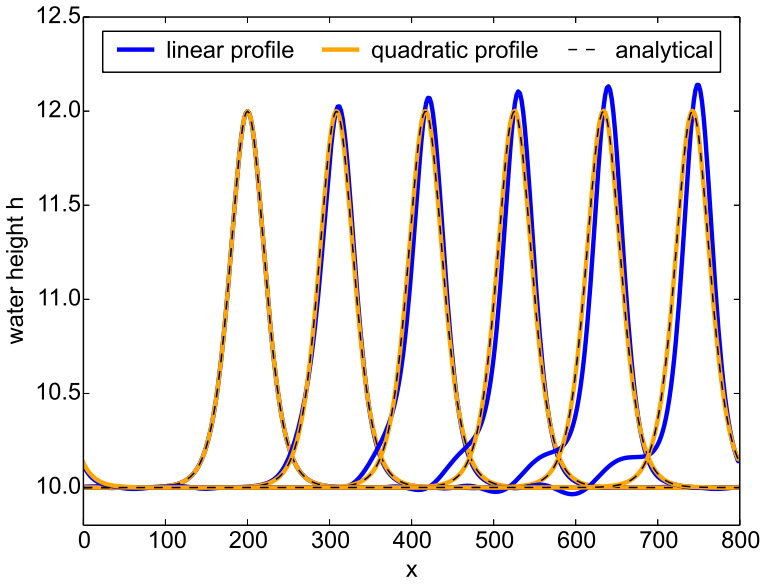

Figure 3.5.: Periodic solitary wave: Comparison of the analytical (black dashed) water height of the solitary wave with the simulation results of the quadratic (yellow) and linear (blue) initial vertical profile and those obtained after a propagation time of 10, 20, 30, 40 and 50 seconds to the right.

3.7.3. Convergence tests showing second order convergence

A convergence test with constant CFL number is conducted. Reasons and notations are given in subsection 3.6.1. Figures 3.6 and 3.7 show experimental errors and orders of convergence with respect to analytical solutions for both aforementioned analytical test cases, namely the periodic linear standing wave and the periodic non-linear propagating solitary wave. The numerical model is fully second order convergent to the analytical solution in both test cases. Exact values of experimental errors and orders of convergence for both tests are presented in the Appendix in tables B.2 and B.3. Experimental convergence test results applying the case $r = 0$ in table 3.4 for the solitary wave test are given in the Appendix in table B.4.

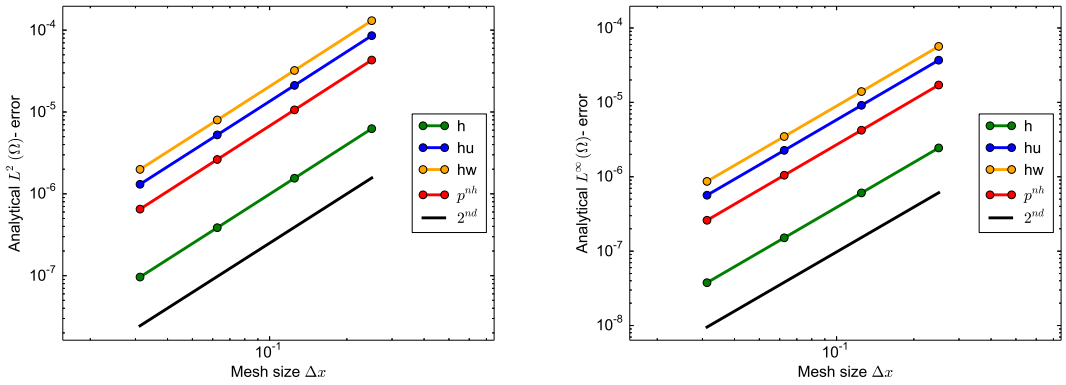

Figure 3.6.: Periodic standing wave: Results of convergence test with $L^2(\Omega)$-norm (left) and $L^\infty(\Omega)$-norm (right) after a simulation time of $3\,\mathrm{s}$.

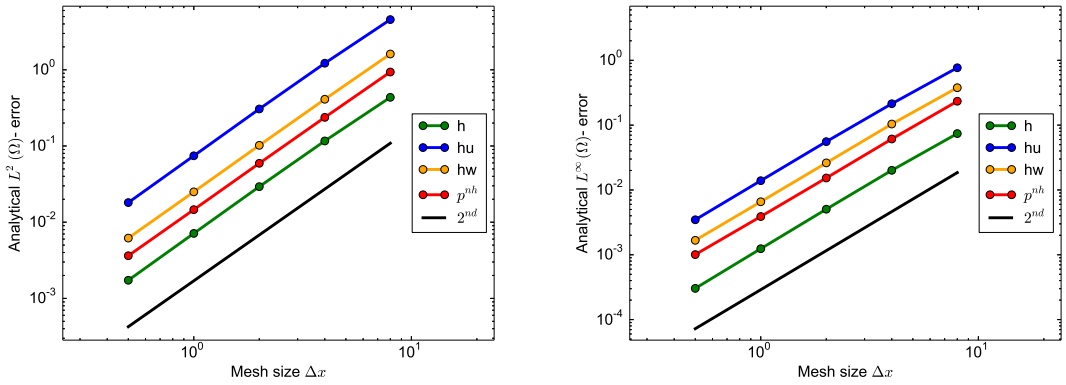

Figure 3.7.: Periodic solitary wave: Results of convergence test with $L^2(\Omega)$-norm (left) and $L^\infty(\Omega)$-norm (right) after a simulation time of $50\,\mathrm{s}$.

3.7.4. Reflecting standing wave

The aim of the reflecting standing wave test is to verify the reflecting boundary conditions in section 3.5.3.3 in case of the linearized non-hydrostatic equation set as is is under study in section 3.7.5. The reflecting standing wave is an analytical solution of both the hydrostatic and the non-hydrostatic linearized equation set. The maximal amplitude a, the phase velocity c, the still water depth d and the wave number κ are defined as given in 3.7.1 for the periodic standing wave. The water height h and the horizontal momentum hu are

$$h(x,t) = d - a\cos(\kappa x)\cos(\kappa c t)\,, \tag{3.82}$$

$$hu(x,t) = -ac\sin(\kappa x)\sin(\kappa c t)\,. \tag{3.83}$$

The dispersive quantities hw and p^{nh} are computed accordingly as section 3.7.1 shows.

Convergence results using the first and second order non-hydrostatic model are shown in figures 3.8 and 3.9. The first order non-hydrostatic model shows first order of convergence as expected. The second order non-hydrostatic model is only able to preserve the second order of convergence for the horizontal momentum. The other three quantities still converge at order one in the $L^\infty(\Omega)$-norm and at order 1.5 in the $L^2(\Omega)$-norm. This results may be improved, but it will suffice for the purpose to show that the implementation of reflecting boundary conditions serves basic expectations of convergence behavior. Exact values of experimental errors and orders of convergence for both tests are presented in the Appendix in tables B.5 and B.6.

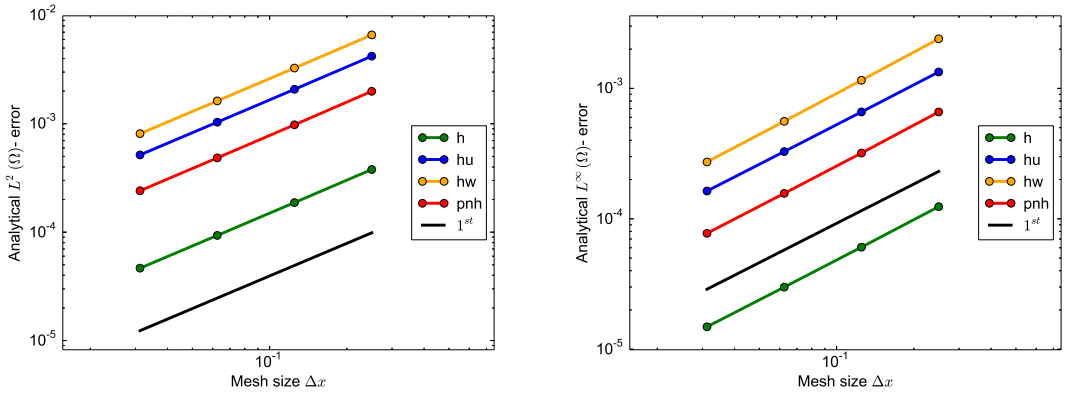

Figure 3.8.: Reflecting standing wave: Results of convergence test with $L^2(\Omega)$-norm (left) and $L^\infty(\Omega)$-norm (right) and first order scheme after a simulation time of $t = 3\,\mathrm{s}$.

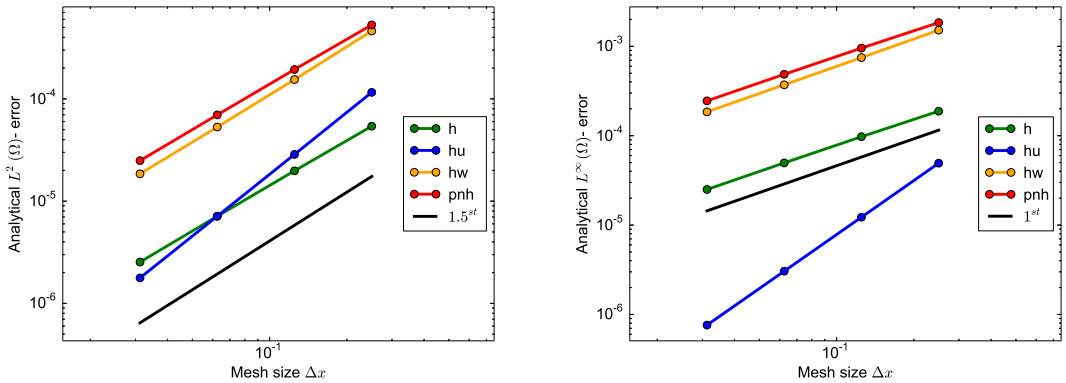

Figure 3.9.: Reflecting standing wave: Results of convergence test with $L^2(\Omega)$-norm (left) and $L^\infty(\Omega)$-norm (right) and second order scheme after a simulation time of $t = 3\,\mathrm{s}$.

3.7.5. Linear solitary wave on a composite beach

After confirming the accurate behavior of the numerical model on constant bathymetry and with three types of boundary conditions, the focus is shifted to problems including a non-zero bathymetry gradient. The bathymetry of this test approximates the geometry of Revere Beach, located close to Boston in the City of Revere, Massachusetts, and was studied in a laboratory experiment [102] to address beach erosion and severe flooding problems. The approximation consists of four segments having piecewise constant slope, whereas the first piece is constant and the other segments differ in length and in their positive slope gradients. Figure 3.10 displays the corresponding setup including the initial condition, which is a solitary wave entering the region with sloping bathymetry from the left and propagates towards a vertical wall on the right. After reflection, the wave moves back till it reaches its starting point. The water elevation is measured at eight different positions including the vertical wall. This signal is compared to an analytical solution, that was derived [63] for the linearized shallow water equations including piecewise linear bathymetry, and proposed to be used as a benchmark in [94]. The analytical solution is similar to the laboratory data, but slight increases in amplitude and phase speed including phase shifts occur after reflection. The laboratory data provide three different specifications varying in initial amplitude a and distance L from gauge G4 to gauge G5. We will consider case A with $a = 0.039d$ and $L = 2.4\,\text{m}$. We use the initial condition

$$h(x,t) = d - b + a\cosh^{-2}(K(x - ct - x_0)), \tag{3.84}$$

$$hu(x,t) = c(h - d + b), \tag{3.85}$$

that is the non-linear solitary wave presented in section 3.7.2, but it is adapted to the non-constant bathymetry b measured from the ground level at gauge G4. This gauge is the point of maximal amplitude at initial state. The non-hydrostatic quantities hw and p^{nh} are set to zero and will adjust during the computation of the first time step.

The hydrostatic as well as the non-hydrostatic numerical model are considered for validation. The domain length is enlarged to 30 meters to ensure that no waves reflected at the left wall disturb the results. The simulation time is 20 seconds. Reflecting boundary conditions are imposed at both boundaries of the computational domain. We use $m = 1601$ cells and a time step of $\Delta t = 0.0025\,\text{s}$ leading to a CFL number of 0.21 at initial state. A desirable CFL number of ca. 0.3 doesn't lead to a stable scheme anymore.

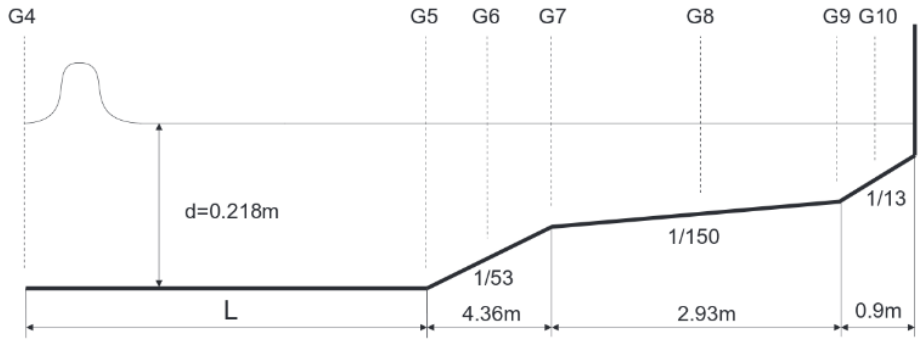

Figure 3.10.: Linear solitary wave on a composite beach: Description of setup [63]

Figures (3.11) and (3.13) depict the results of the linearized shallow water model and the results of the linearized non-hydrostatic equation set with both pressure profiles, respectively. The comparison to the laboratory data is shown in figures 3.12 and 3.14. Note that the results are shifted by 271.5 seconds to match the initial analytical wave at gauge G4.

The results of the hydrostatic shallow water model are in very good agreement with the analytical solution. At gauges G9 and G10 closest to the wall, numerical and analytical solutions differ most, but not strongly. The incoming and the reflected wave signal interact with each other at these gauges. After reflection, the wave amplitude is reduced slightly, but this decrease depends on the spatial grid size and is diminished with refinement. The differences of the hydrostatic model results to the laboratory data in figure 3.12 are the same as of the analytical solution compared to the laboratory data.

The results of the non-hydrostatic equation set show a coincidence in phase of the maximal amplitude of the analytical solution, but not in the amplitude. The influence of the bathymetry causes a reduction in amplitude and the generation of wave trains following the main surface elevation. Both effects intensify during propagation into shallower water. The wave train is artificial as the comparison to the laboratory data in figure 3.14 shows.

This indicates that the choice of the initial condition is accurate enough for the non-hydrostatic case, as it does not influence the result much. The non-linear and first order version of the non-hydrostatic model give very similar results. Other studies (e.g. [103]) of non-hydrostatic models applying the linear pressure profile show very good results under the conditions of this test case. No artificial wave train arises. Hence, the differences to the analytical solution are not likely an outcome of the assumption $f_{\mathrm{d}} = 0$ that was made in the derivation the non-hydrostatic model, because it is not included in other non-hydrostatic models either. The discontinuity in the bathymetry gradient may be the cause for the reduction in amplitude and the artificial wave train. However, a routine to smooth the bathymetry is left for future study. Another reason may be the implementation of the reflecting boundary

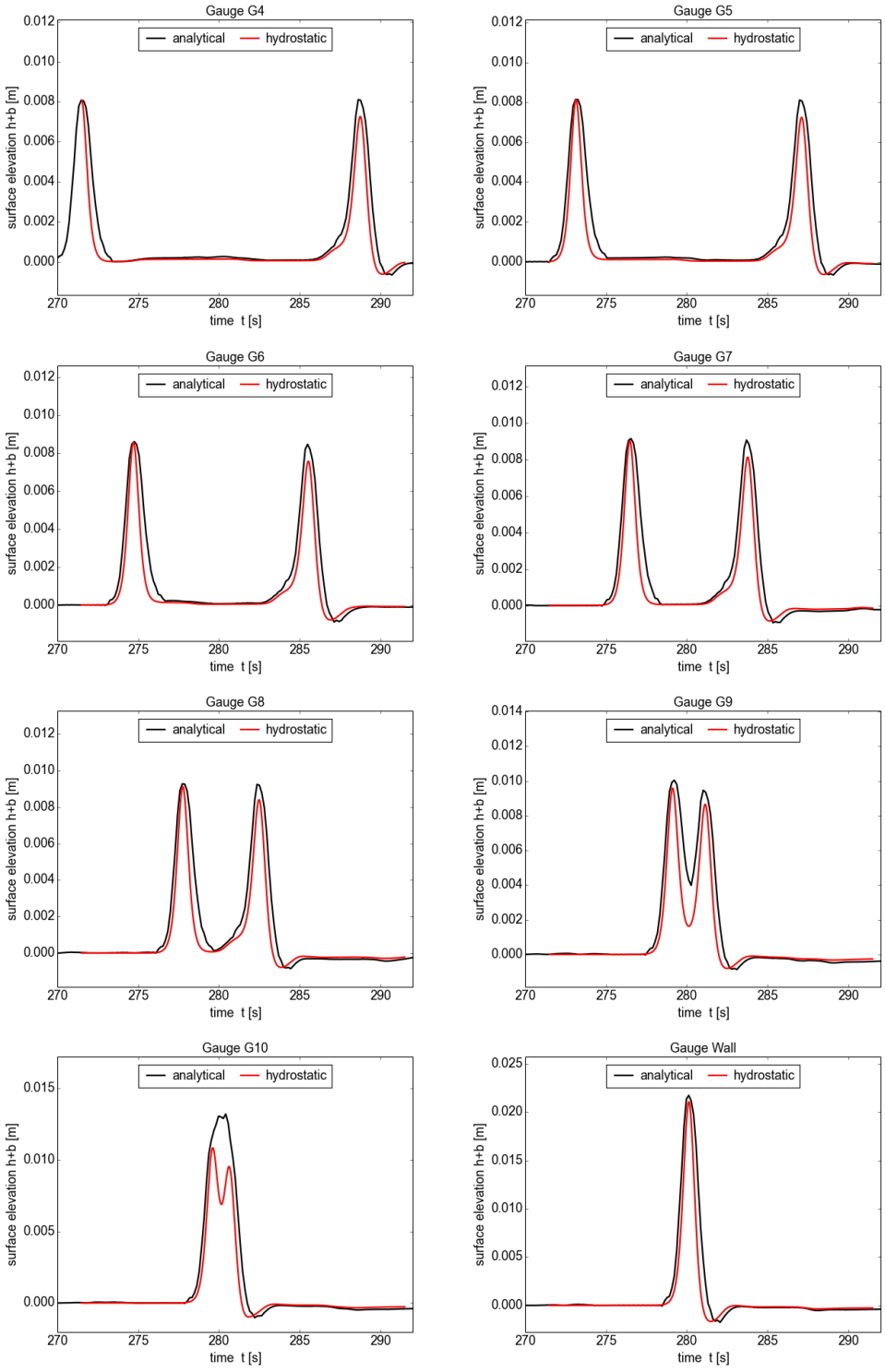

Figure 3.11.: Linear solitary wave on a composite beach: Comparison of the analytical (black) surface elevation of the solitary wave with the simulation results of linearized shallow water equations (red).

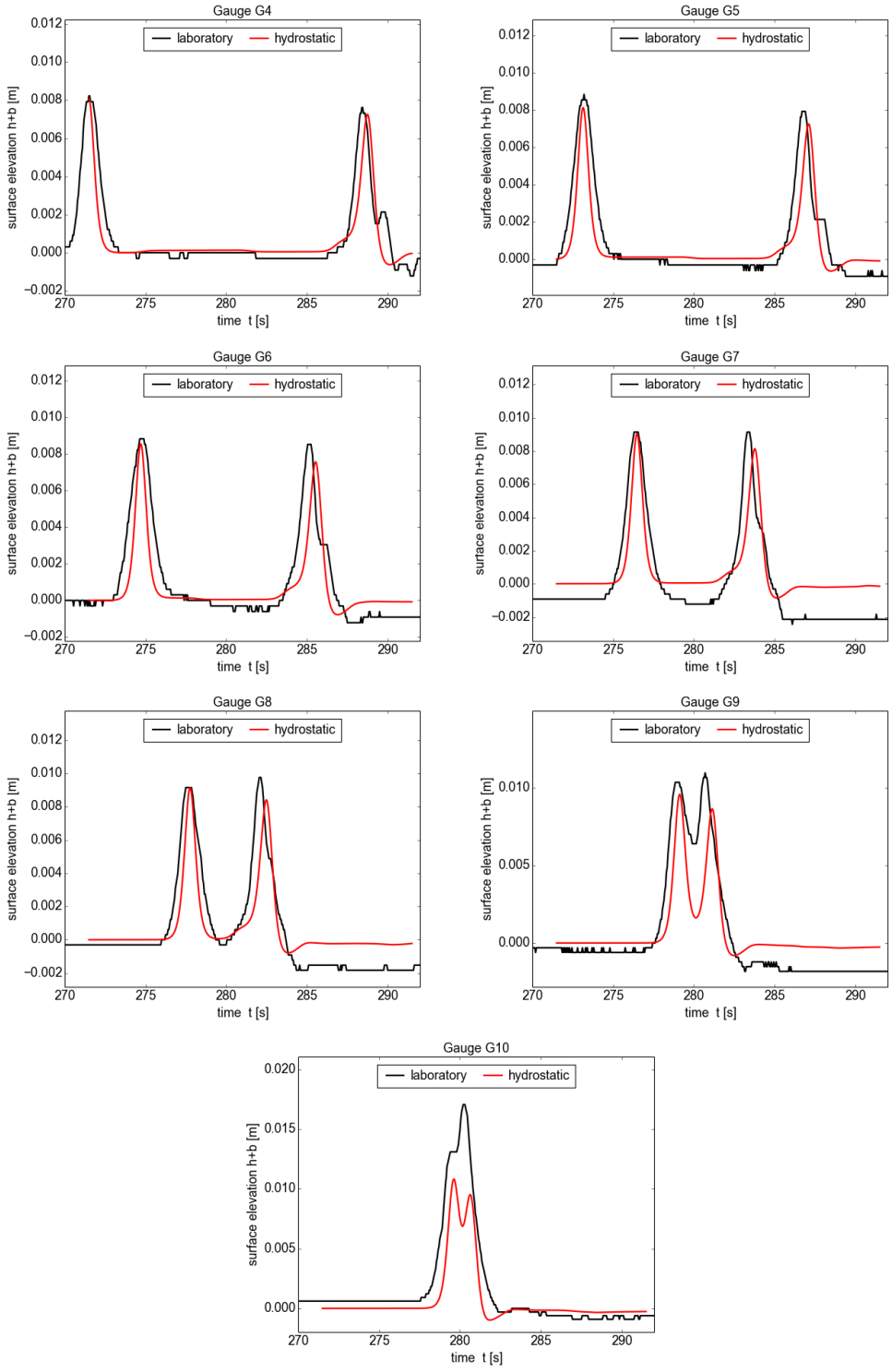

Figure 3.12.: Linear solitary wave on a composite beach: Comparison of the laboratory (black) surface elevation of the solitary wave with the simulation results of linearized shallow water equations (red).

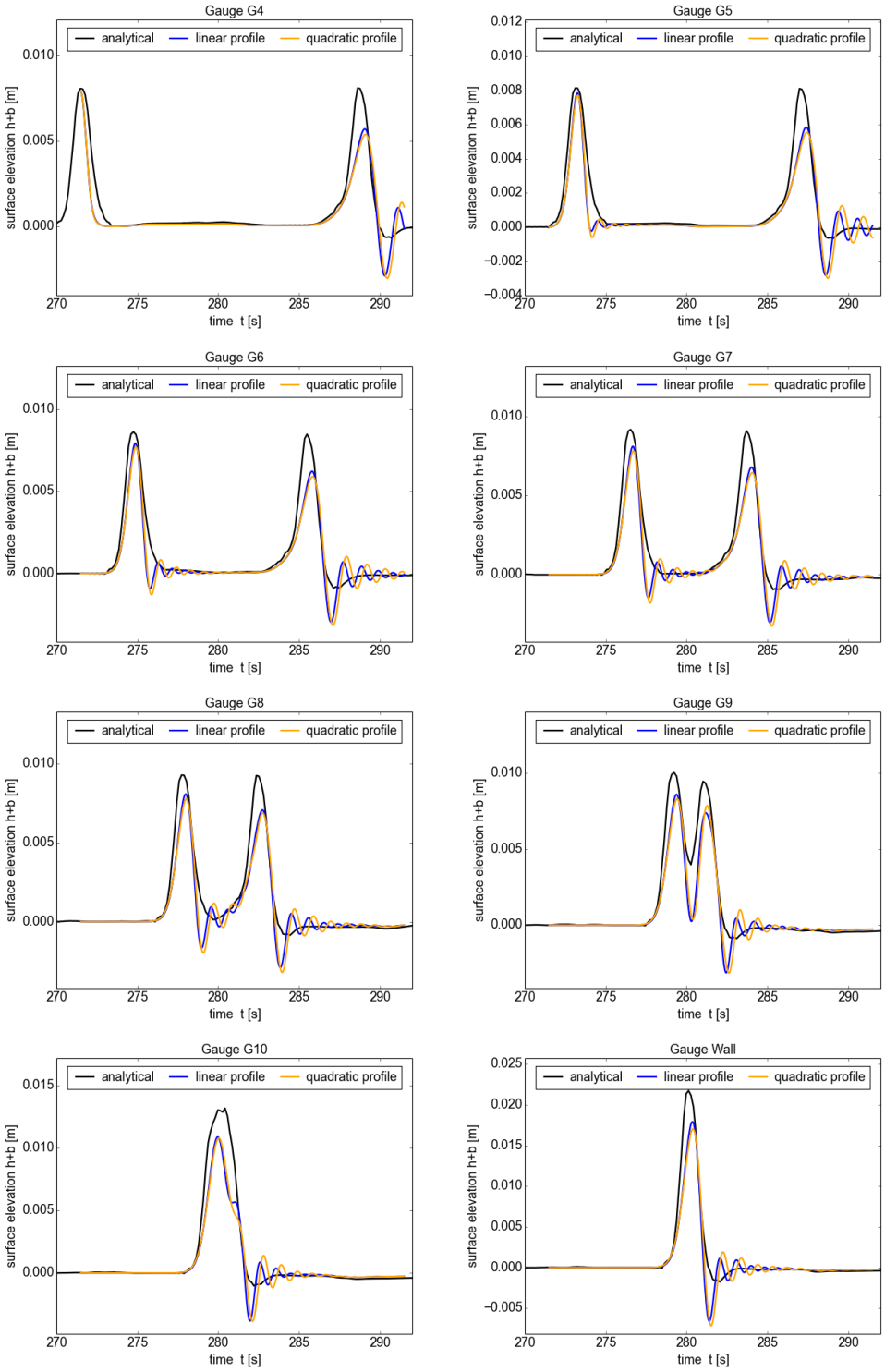

Figure 3.13.: Linear solitary wave on a composite beach: Comparison of the analytical (black) surface elevation of the solitary wave with the simulation results of the linearized non-hydrostatic extension for shallow water equations with linear (blue) and quadratic (yellow) vertical pressure profile.

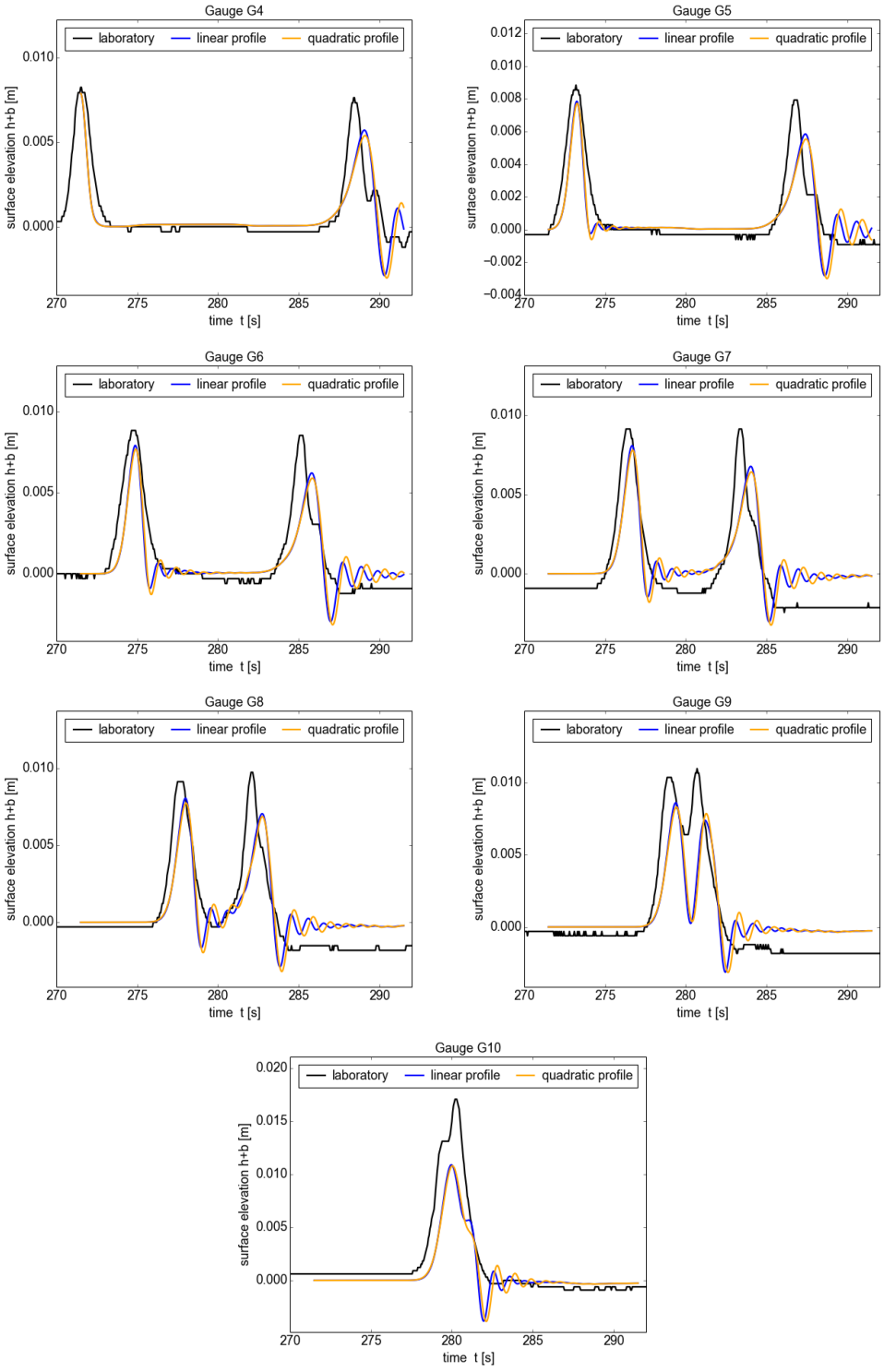

Figure 3.14.: Linear solitary wave on a composite beach: Comparison of the laboratory (black) surface elevation of the solitary wave with the simulation results of the linearized non-hydrostatic extension for shallow water equations with linear (blue) and quadratic (yellow) vertical pressure profile.

condition that fulfills basic properties as convergence, but shows a reduction in convergence order (see section 3.7.4). Furthermore, the maximal CFL number leading to a stable scheme is diminished. It is not clear how to better define a reflecting boundary condition for the non-hydrostatic extension for shallow water equations if the LDG method is applied. This fact represents a disadvantage of the presented approach compared to Boussinesq-type models.

It is remarkable that the choice of the vertical pressure profile has only a tiny impact on the numerical result. This may be due to larger sources of error as described above. Still, the fact that the linear profile leads to higher maximal amplitudes than the quadratic profile seems to be visible also in the results of this test case.

3.7.6. Periodic waves over a submerged obstacle

This test provides laboratory data on non-constant bathymetry to validate the numerical model. A periodic wave train is generated at the left boundary and travels over an underwater trapezoidal bar while measurements of the water elevation are taken at eight wave gauges. Similar experiments were reported in [7] and [69]. We use the data generated in [69], but scaled by a factor of two to the setup of [7], as described in [40]. This combination is often used for validation for Boussinesq-type as well as for non-hydrostatic models (e.g. [48, 92, 101]), and especially with great success for higher order Boussinesq-type models (e.g. [8, 43, 107]).

Figure 3.15 displays the setup for the simulations. The underwater obstacle clearly deforms the shape of the initially periodic wave. Higher harmonics are generated on the upward slope because of non-linear shoaling, and the fissioning process starts due to the dependency of phase speed on the wave length. Peaked waves become visible on the bar. Higher harmonics are released during propagation downward the slope and behind the bar resulting in a multi-frequency irregular wave pattern. Three different cases are described in [40] differing in wave period T and initial amplitude a. It is stated that the non-breaking wave in case A is enough to reveal main differences among a large amount of dispersive numerical models, so we conduct this test only. Case A is determined by a wave period of $T = 2.02\,\mathrm{s}$ and an initial amplitude of $a = 0.01\,\mathrm{m}$. Purely hydrostatic models typically exhibit some unrealistic sawtooth-shape behavior (see e.g. [48]) because of missing dispersion properties needed to counterbalance the inherent non-linearity. The initial condition is the unperturbed state. The boundary condition is described as an incident wave at the left boundary of the computational domain. The incident height profile is

$$h(t,0) = d + a\sin\left(\frac{2\pi t}{T}\right)$$

and the horizontal momentum is set accordingly to wave characteristics of the non-linear shallow water model. The non-hydrostatic quantities hw and p^{nh} adapt during the first time step. Transparent outgoing boundary conditions are imposed on the right boundary in the

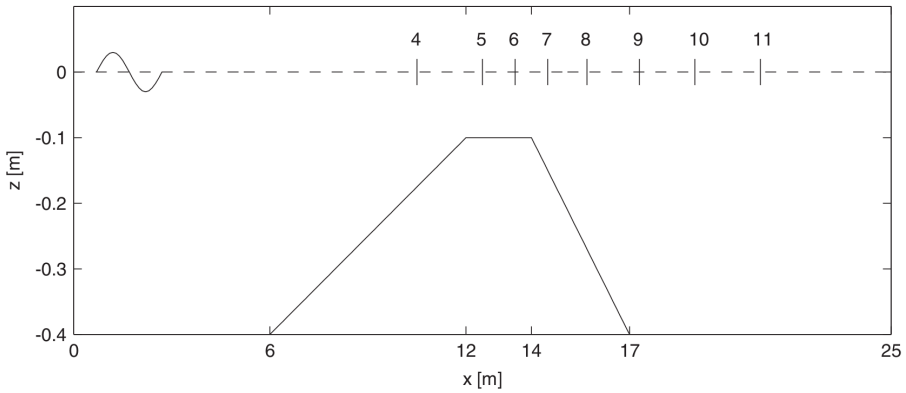

Gauge	G4	G5	G6	G7	G8	G9	G10	G11
x [m]	10.5	12.5	13.5	14.5	15.7	17.3	19.0	21.0

Figure 3.15.: Periodic waves over a submerged obstacle: Setup of the experiment [92]

same manner. We choose a domain length of $40\,\mathrm{m}$, a number of $m = 1200$ cells and a time step of $\Delta t = 0.005\,\mathrm{s}$ to achieve a CFL number of CFL ≈ 0.3.

The results of the non-hydrostatic model applying the linear and the quadratic pressure profile are presented in figure 3.16. Both pressure profiles yield similar results that are close to experimental data until the wave reaches gauge G7. A possible explanation for slight differences are due to the linear dispersion relation (see section 2.4.1 and figure 3.3). The reason is that the incident wave is close to the long-wave regime ($\frac{d}{\lambda} \approx 0.1$), and shifted even more towards the long-wave regime on top of the obstacle. Hence, the phase speed is large and high harmonics are generated by non-linearity and bathymetry. These higher harmonics need longer travel distances to become visible. We observe a slower propagation speed of the quadratic pressure profile compared to the linear profile and a tendency of the linear profile to generate higher amplitudes. This is similar to observations in above test cases. However, the propagation speed of the linear profile unfolds to be closer to the experimental data than the one of the quadratic profile. But the quadratic profile better approximates the experimental data with respect to the wave amplitude.

Gauges G8 to G11 show another behavior, because the fast increase in depth causes the difference in propagation speed of higher harmonics and long waves become obvious. As stated in [40], these are the gauges pointing clearly to distinctions of numerical models, what is especially true in our case. The linear pressure profile nearly coincides with experimental data with respect to the propagation speed, and the quadratic profile generates too slow waves, such that the time shift in wave profiles increases with propagation distance. Additionally, the wave amplitude of the quadratic profile shows a closer coincidence compared to experimental data. The linear profile does not yield high enough wave amplitudes. This is the opposite to

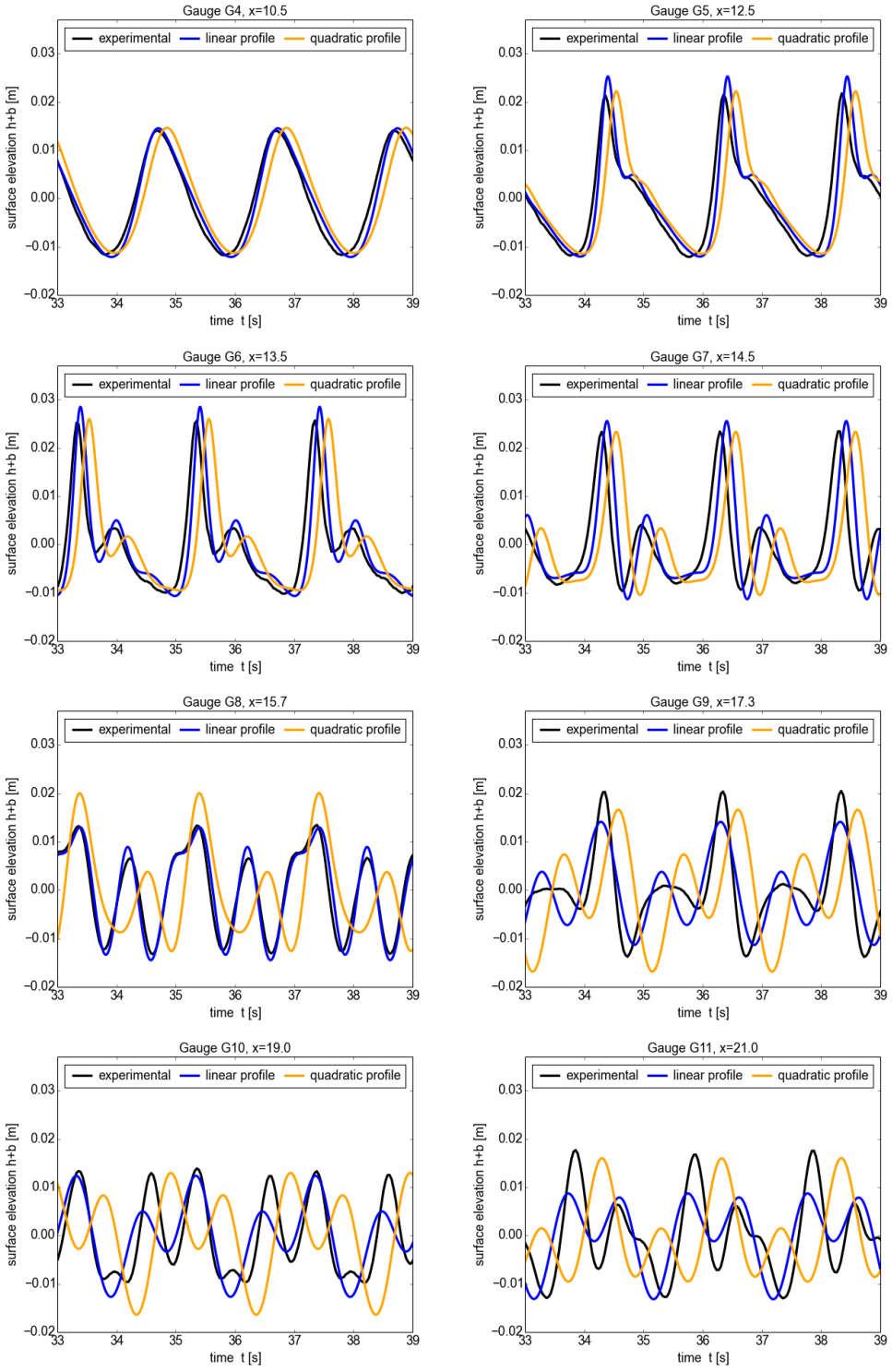

Figure 3.16.: Periodic waves over a submerged obstacle: Comparison of the experimental (black) surface elevation with the non-hydrostatic simulation results with both the linear (blue) and the quadratic pressure profile (yellow).

the observations at gauges G4 to G7. In summary, the results of this test case provide the information that the dispersion properties of both vertical pressure profile differ clearly in case of high non-linearity and non-constant bathymetry. This was not obvious when considering their linear dispersion relations singly in section 3.7.1. However, the influence of the scalar f_d is not included in the results. Other studies [67, 79, 107] that approximate the Green-Naghdi equations and use the same experimental data achieve much better results. Hence, we suppose that the numerically missing scalar f_d is responsible for the worse behavior of the quadratic profile than the linear profile in this test. The results obtained with the linear pressure profile are close to results obtained with other non-hydrostatic models (see e.g. [48, 92]).

3.7.7. Solitary wave on an inundated simple beach

This analytical test case serves to validate the model's behavior close to the shoreline, especially during run-up and run-down in the inundation zone. A solitary wave propagates over a constant bathymetry, until it reaches a linear sloping beach. The wave inundates the dry area and the offtake starts after the wave reached the maximum run-up point. The analytic test case considers a non-breaking wave and yields comparison data in terms of snap-shots in time as well as data at two specific locations. An analytical solution is given in [95, 96]. The setup and fixed parameters therein are shown in figure 3.17. Dispersive as well as hydrostatic simulations are conducted. The initial condition is prescribed as the analytic solitary wave solution as in (2.48)–(2.52), but parameters are chosen according to figure 3.17. The propagation speed c is chosen as $c = -c_\mathrm{sw}$ and $c = -\sqrt{g(d+a)}$ for the hydrostatic and non-hydrostatic model runs, respectively. Note that the solitary wave has a negative propagation speed as the sign of the x-

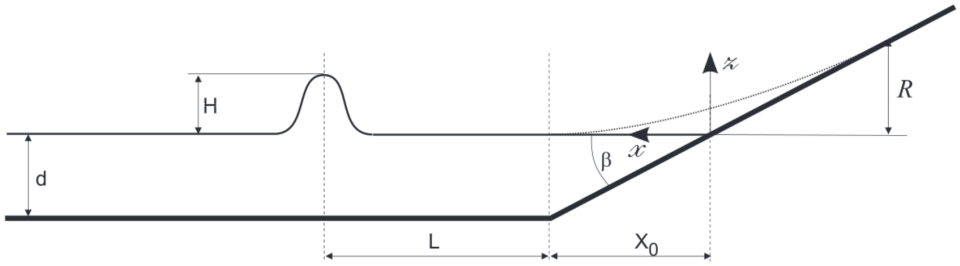

x_0	L	X_0	β	$H = a$
$L + X_0$	$\frac{\operatorname{arccosh}(\sqrt{20})}{(Kd)}$	$d\cot(\beta)$	$\operatorname{arccot}(19.85)$	$0.019d$

Figure 3.17.: Solitary wave on an inundated simple beach: Description of setup depending on the maximal water depth d.

axis changed compared to the solitary wave definitions in sections 3.7.5 and 3.7.2. We choose the water depth to be $d = 1$ m and further parameters according to 3.17. The computational domain is $[-30, 70]$ m and the simulation time is set to 40 seconds. For $m = 400$ cells, we use a time step of $\Delta t = 0.02$ s, such that the CFL number is CFL≈ 0.26. The wet-dry treatment in the non-hydrostatic model follows the description in 3.6.2.

Figures 3.18 and 3.19 compare the analytic solution to the hydrostatic as well as to the non-hydrostatic model results. The snap-shots in figure 3.18 are taken at six different non-dimensional times $t/\sqrt{\frac{d}{g}}$ using a mesh with $m = 400$ cells. Hydrostatic and non-hydrostatic simulation results are not distinguishable from each other, and both provide a very good coincidence with the analytical solution. Figure 3.19 shows time series of the water height at two locations in the inundation zone. The first location at $x/d = 9.95$ is wet throughout the simulation time, whereas the second location at $x/d = 0.25$ falls dry and is flooded again. The results are displayed showing four different resolutions with same constant CFL number CFL≈ 0.26. The graphs also serve to show convergence to the analytical solution. The convergence is visible for the hydrostatic as well as for the non-hydrostatic model results, whereas the hydrostatic model converges faster than the non-hydrostatic model. Both pressure profiles yield very similar wave profiles, that are only slightly distinguishable except at the time shortly before drying. This test case including inundation shows that the second order non-hydrostatic model is well capable of simulating wetting and drying processes.

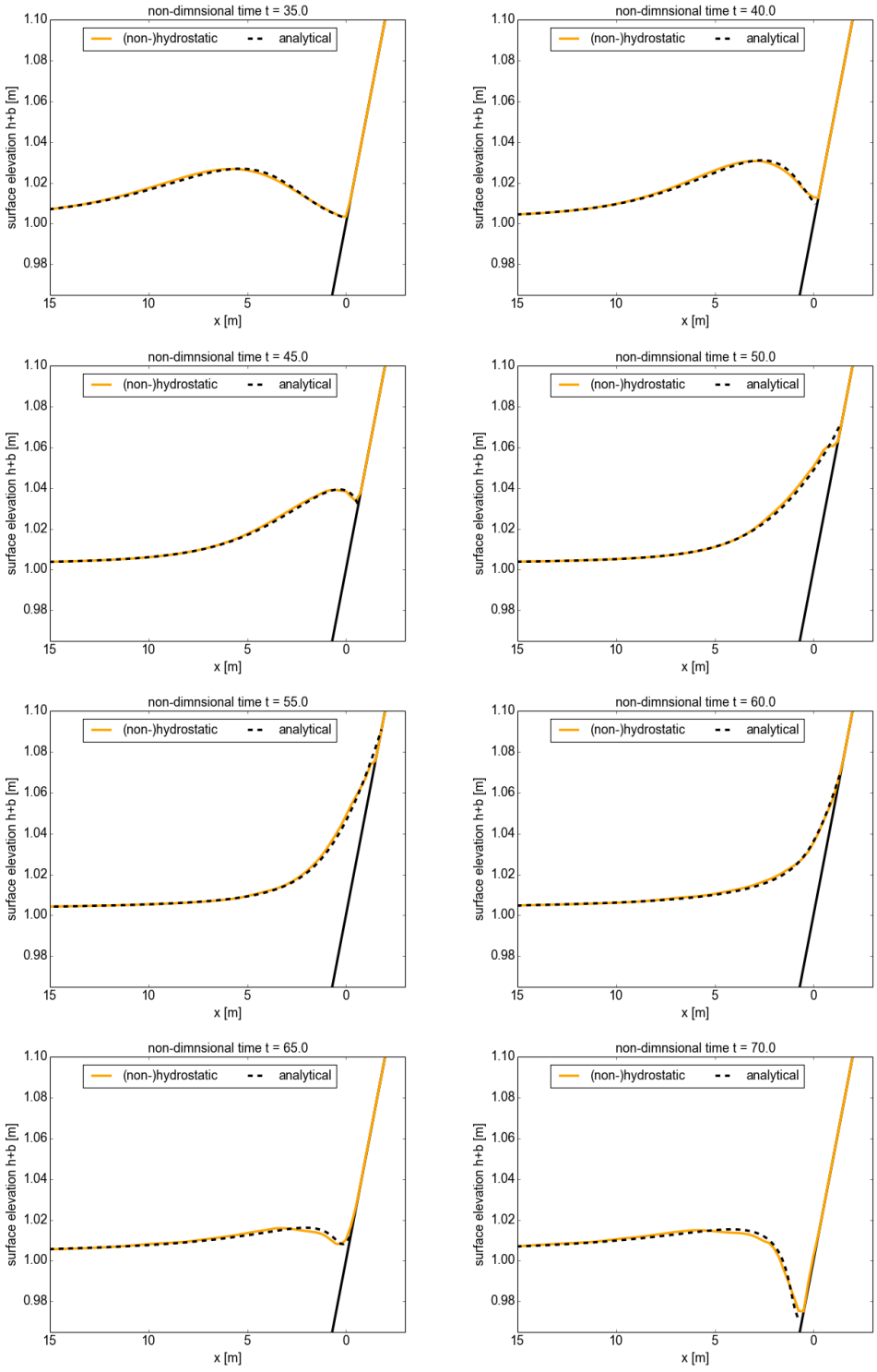

Figure 3.18.: Solitary wave on an inundated simple beach: Comparison of the analytical (black) surface elevation with simulation results (yellow), whereas there is no visible difference between hydrostatic and non-hydrostatic model results.

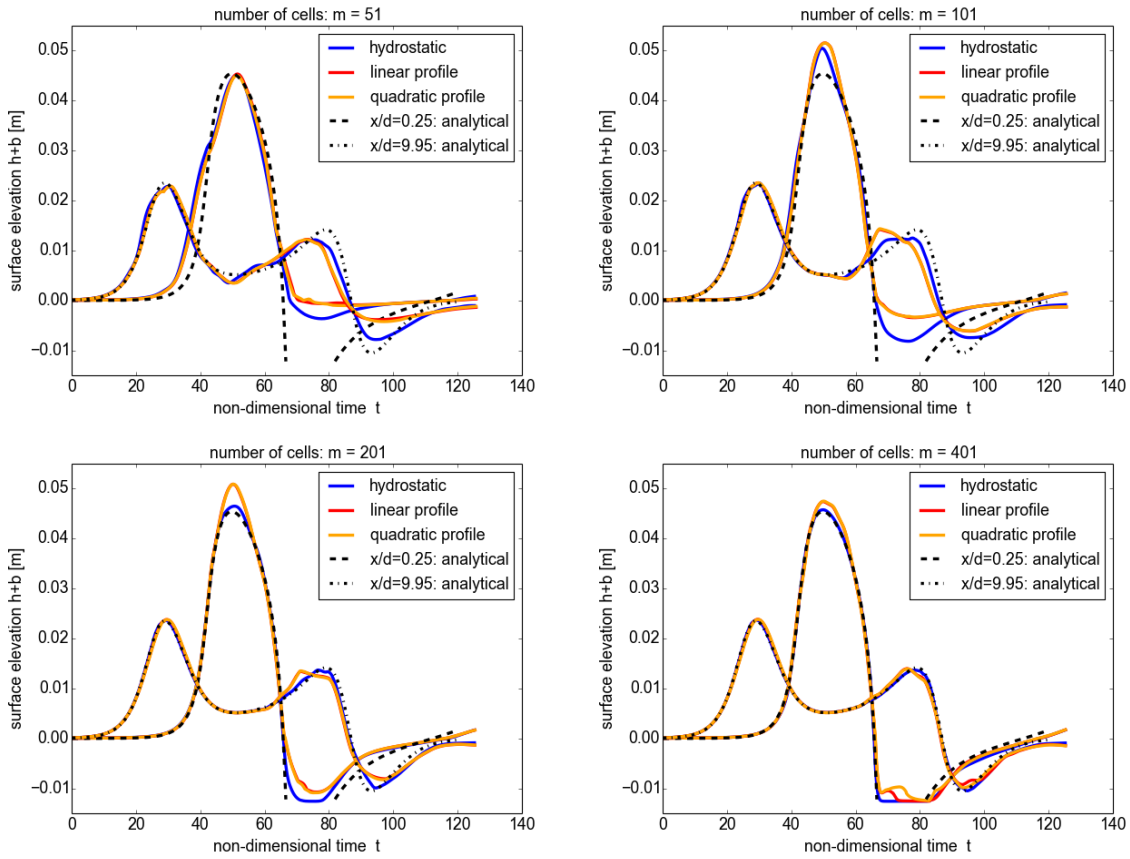

Figure 3.19.: Solitary wave on an inundated simple beach: Convergence plots at two points on the shoreline. Convergence plots are generated with constant CFL number as described in section 3.7.3.

4 Local non-hydrostatic extension for shallow water equations

4.1. Abstract

A local version of the non-hydrostatic extension for shallow water equations described in chapter 3 is presented. The aim of this local approach is to provide a more efficient but not convergent method for the non-hydrostatic equation set. The idea is to split the computational domain into a hydrostatic and a non-hydrostatic region which are determined using a simple splitting criterion based on linear theory. An introductory example serves to illustrate the need for such an efficiency improvement in case of larger computational domains. Preliminary numerical results show appropriate functionality that suggests to consider the local approach for more detailed future investigations.

4.2. Efficiency comparison

The second order method in chapter 3 was developed in order to obtain a more accurate numerical method. However, the concern about efficiency of higher order methods arises when thinking towards real-world applications. A large computational domain leads to an increase in the total number of cells used in the numerical model to keep the resolution reasonably small to simulate features of interest. An increase of the total number of cells leads to larger computational cost. The efficiency of the (global) hydrostatic model as well as the (global) first order and the (global) second order non-hydrostatic model is illustrated in the following. Both non-hydrostatic models are described in section 3.4.1 and table 3.4 gives an overview. Figure 4.1 illustrates the computational time of these three models using the propagating solitary wave test (see section 3.7.2) depending on the total number of cells. Averages of three different model runs are shown for each model. Routines as plotting routines or convergence tests that produce additional computational overhead are omitted during computation. The non-hydrostatic models use the quadratic pressure profile, but an application of the linear pressure

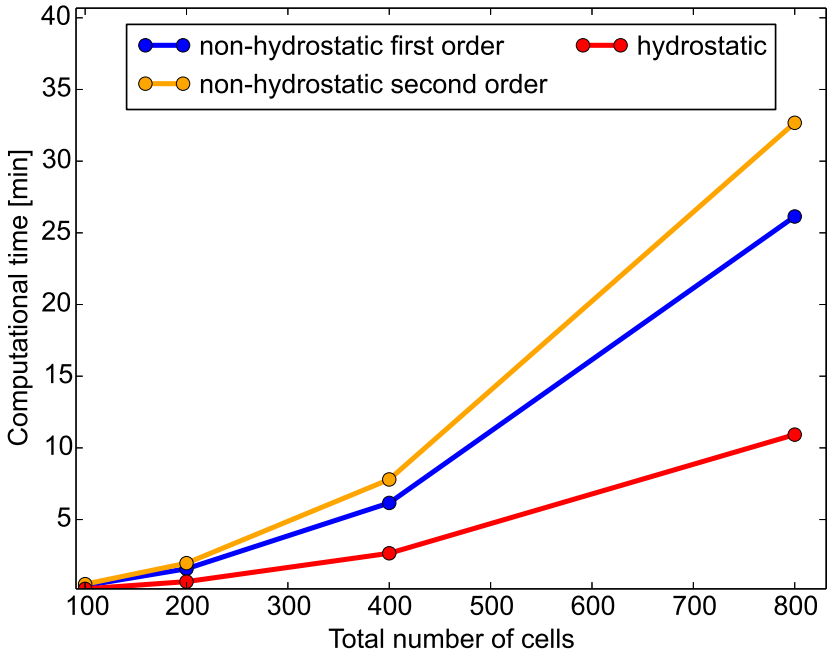

cell number	t^{comp}_{nh2nd} [min]	t^{comp}_{nh1st} [min]	t^{comp}_{hy} [min]	t^{comp}_{nh2nd} / t^{comp}_{hy}	t^{comp}_{nh1st} / t^{comp}_{hy}
100	0.49	0.40	0.16	3.02	2.40
200	1.96	1.57	0.67	2.92	2.33
400	7.80	6.16	2.65	2.95	2.33
800	32.7	26.1	10.9	2.99	2.39

Figure 4.1.: Computational time depending on the total number of cells for the solitary wave test (see section 3.7.2) including a hydrostatic computation. Displayed values are averages of three model runs.

profile would not change the results.

The computational costs of the second order non-hydrostatic model exceed the cost of the shallow water model by a factor of 3.0, approximately, if the same resolution is considered. The first order non-hydrostatic model shows a factor of 2.4 in this case. The reason for the larger computational cost of the second order compared to the first order non-hydrostatic model are additional source terms and the calculation of an additional equation (the water height update (3.30)) in case of the second order model. The additional source terms are the terms including the extrapolated non-hydrostatic pressure $(p^{nh})^{ex,n+1}$ in the predictor and corrector equations (3.28)–(3.29) and in the elliptic system of equations (3.33)–(3.34).

The first order model is the better choice in terms of efficiency playing a dominating role if large computational domains are considered. Additionally, the splitting criterion described in the next section will be another source of accuracy error introduced into the model. Hence, the non-hydrostatic model considered throughout this chapter is the first order model.

4.3. Splitting criterion

The splitting criterion applied is a simple on-off criterion for the non-hydrostatic extension. The criterion splits the computational domain into two (maybe not connected) subsets: The subset, where the complete non-hydrostatic model is used, is called the *non-hydrostatic region*. Similarly, the *hydrostatic region* is defined to be the subset, where the execution of the shallow water model takes place only and the projection method is not in use.

The first guess for such a splitting criterion may be the well-known criterion $\frac{d}{\lambda} < 0.05$ for the validity of the hydrostatic assumption. However, a finite wave length is not determined easily for every situation, e.g. if the wave is a solitary wave having an infinite length by definition or if a wave train is considered. Additionally, the criterion $\frac{d}{\lambda} < 0.05$ may yield that the entire computational domain is the non-hydrostatic region, what is true in the physical sense, but useless to define a splitting criterion. Hence, the aim is to define a splitting criterion such that the non-hydrostatic pressure is small in the hydrostatic region. This is the case at least, if the horizontal and vertical velocities and the water elevation are small enough. This argument helps to avoid the computation of the non-hydrostatic pressure in advance. The splitting criterion is chosen to depend on the water surface elevation $\xi = h + b - d$ only. For small quantities, it is reasonable to restrict to linear theory. The splitting criterion is defined as

$$\frac{\xi}{d} \leq k_{nh} \ll 1, \qquad \text{with fixed } k_{nh} > 0. \tag{4.1}$$

A study to determine suitable values for the splitting parameter k_{nh} is included in section 4.4. This criterion implicitly defines zero Dirichlet boundary conditions for the elliptic system of equations in the non-hydrostatic region. The simple splitting criterion introduces additional errors at the interfaces of both regions because this boundary condition is an approximation. These errors become visible in parts of the results presented in section 4.4. However, it may be possible to control the errors in some cases and long simulation times. It is the aim of this chapter to determine preliminary suitable combinations of splitting criterion and resolution. Other criteria are left for future study.

This approach differs from previous ones in two aspects: First, the resolution is kept the same in the entire computational domain whereas it needs to be fine enough to keep numerical dispersion small, of course. Second, the model based on a projection method is very well suited to split the domains into a non-hydrostatic and a hydrostatic region, because the model has the

same accuracy and discretization properties as the non-hydrostatic extension as no higher order derivatives are inherent in the non-hydrostatic extension. Hence, possible coupling problems related to different discretization schemes do not arise and there is no extra computational work because of higher order discretizations that are not needed in the hydrostatic region. Hence, the numerical model is especially suitable in hydrostatic regions individually, if the non-hydrostatic extension is turned off. The opposite case may appear in a Boussinesq-type model.

4.4. Preliminary numerical results

This section presents numerical results of the local version of the non-hydrostatic extension for shallow water equations. Two test cases of section 3.7 are adjusted and results depending on different splitting parameters (see equation 4.1) and resolutions are shown. Emphasis is placed on computational efficiency improvement and adequate results in case of longer simulation times. Both tests consider the quadratic vertical pressure profile and the first order non-hydrostatic model only. All computations are performed on a single core of a 2.0 GHz Intel i5-4310U processor.

4.4.1. Propagating solitary wave

This test continues the introductory example in section 4.2 and adds the computational times gained with the local approach. Furthermore, the behavior of the model applying the local approach in case of a longer simulation time of 10 minutes is examined.

Table 4.1 shows computational times after a simulation time of 50 seconds. The results of the non-hydrostatic model in its global version, the results of the local version applying four splitting parameters k_{nh} as well as the results of the purely hydrostatic model are presented. The computational overhead of the global version and all local versions of the non-hydrostatic model are compared to the hydrostatic model. All values are presented for four different resolutions. The splitting parameter k_{nh} clearly influences the computational time of the non-hydrostatic model. The influence of the splitting parameter is more distinct in case of increasing cell numbers. The computational efficiency benefits from a larger splitting parameter, because the concrete value of the splitting parameter determines the size of the non-hydrostatic region. Large computational domains lead to the necessity to guarantee that the error accumulated over time does not destroy the quality of results.

Hence, figure 4.2 illustrates the shape of the solitary wave after a longer propagation time of 10 minutes in a larger computational domain of size $l = 8000\,\text{m}$. The initial displacement is $x_0 = 200\,\text{m}$. Non-hydrostatic and hydrostatic regions are marked for three splitting parameters $k_{nh} \in \{0.001, 0.004, 0.007\}$. All splitting parameters show clearly distinguished results. The

two larger splitting parameters are not able to preserve the shape of the initial wave profile. The wave amplitude is reduced smoothly over time until the wave is vanishing. The speed of this damping effect increases with resolution and increasing splitting parameter.

cell nr.	t^{comp}_{nh1st}[min]	$t^{comp}_{0.001}$[min]	$t^{comp}_{0.004}$[min]	$t^{comp}_{0.007}$[min]	$t^{comp}_{0.01}$[min]	t^{comp}_{hy}[min]
100	0.39	0.22	0.21	0.20	0.20	0.16
200	1.57	0.90	0.83	0.81	0.80	0.67
400	6.16	3.85	3.51	3.30	3.22	2.65
800	26.1	20.3	15.8	14.5	13.6	10.9

cell nr.	$t^{comp}_{nh1st}/t^{comp}_{hy}$	$t^{comp}_{0.001}/t^{comp}_{hy}$	$t^{comp}_{0.004}/t^{comp}_{hy}$	$t^{comp}_{0.007}/t^{comp}_{hy}$	$t^{comp}_{0.01}/t^{comp}_{hy}$
100	2.40	1.38	1.30	1.25	1.23
200	2.33	1.35	1.24	1.20	1.19
400	2.33	1.46	1.33	1.25	1.21
800	2.39	1.86	1.44	1.33	1.24

cell nr.	$1-t^{comp}_{0.001}/t^{comp}_{nh1st}$	$1-t^{comp}_{0.004}/t^{comp}_{nh1st}$	$1-t^{comp}_{0.007}/t^{comp}_{nh1st}$	$1-t^{comp}_{0.01}/t^{comp}_{nh1st}$	$1-t^{comp}_{hy}/t^{comp}_{nh1st}$
100	0.42	0.45	0.48	0.49	0.58
200	0.42	0.47	0.49	0.49	0.57
400	0.37	0.43	0.46	0.48	0.57
800	0.22	0.4	0.45	0.48	0.58

Table 4.1.: Propagating solitary wave applying the local approach after a simulation time of 50 seconds: Computational time depending on resolution (upper table) of the global first order non-hydrostatic model, the local approach with four splitting parameters $k_{nh} \in \{0.001, 0.004, 0.007, 0.01\}$ and the hydrostatic model. All values are averages of three model runs. The overhead compared to hydrostatic computations (middle table) and the efficiency gain compared to global non-hydrostatic computations (lower table) are shown.

In opposite, the application of the splitting parameter $k_{nh} = 0.001$ yields the same graphical results for 2000 and 4000 cells with good shape preserving properties. In case of too coarse resolution (1000 cells), the model does not reproduce the initial wave profile accurately and a small wave train develops that enlarges the non-hydrostatic region. However, there is only one connected non-hydrostatic region in all cases. Hence, the splitting into hydrostatic and non-hydrostatic regions behaves appropriately.

This test shows that the choice of the splitting parameter needs to be done carefully in order to maintain good wave propagation properties. Both adequate combinations of resolution and splitting parameters are more efficient compared to the global non-hydrostatic run as table 4.1 shows. The computational efficiency gain of the local approach compared to the non-hydrostatic model run is $37 - 42\%$ for a simulation time of 50 seconds with given shape of

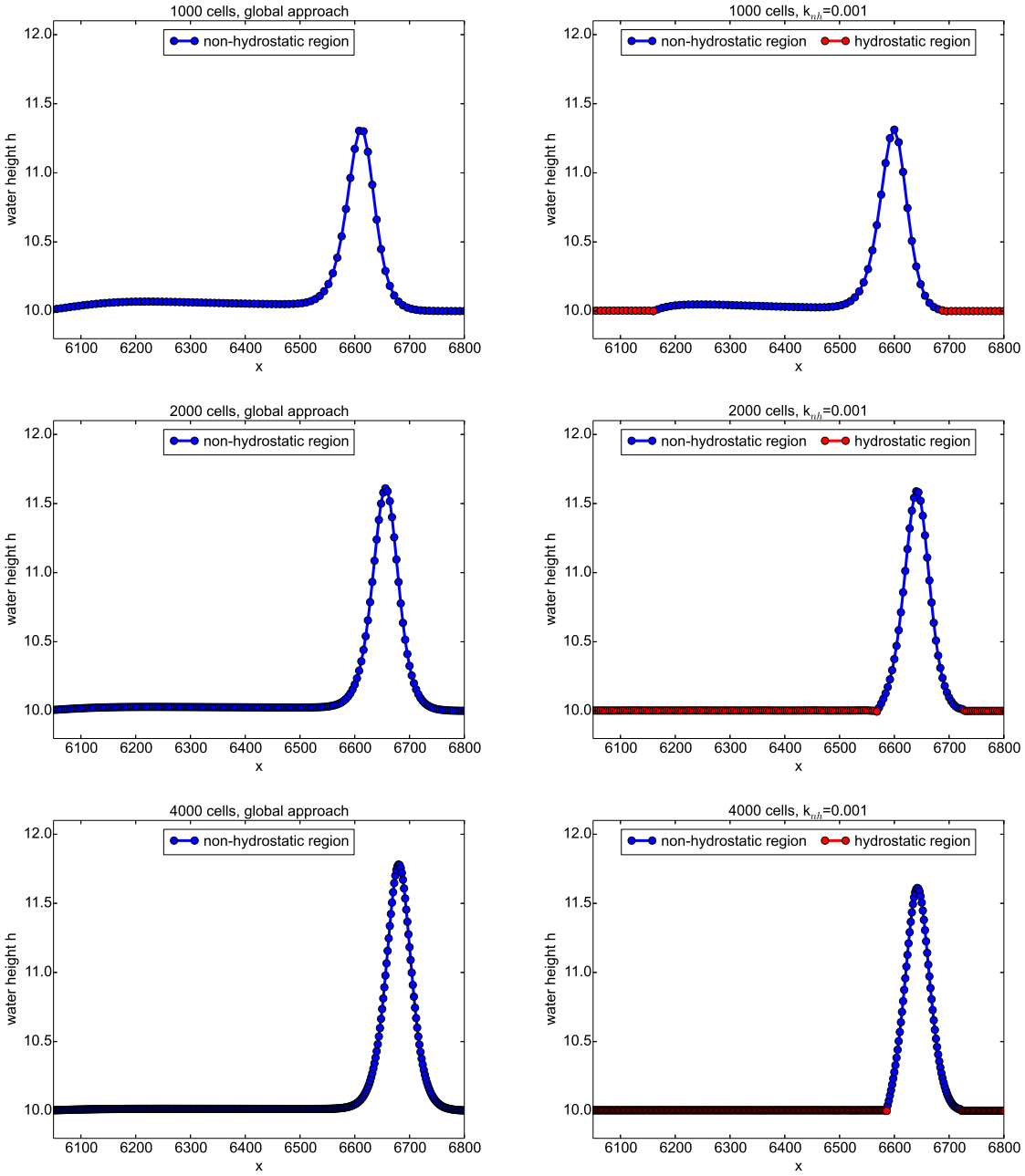

Figure 4.2.: Propagating solitary wave applying the local approach after a simulation time of 10 minutes: Three resolutions with $1000, 2000$ and 4000 cells are combined with the simulation results of the global approach and the local approach with the splitting parameter $k_{nh} = 0.001$.

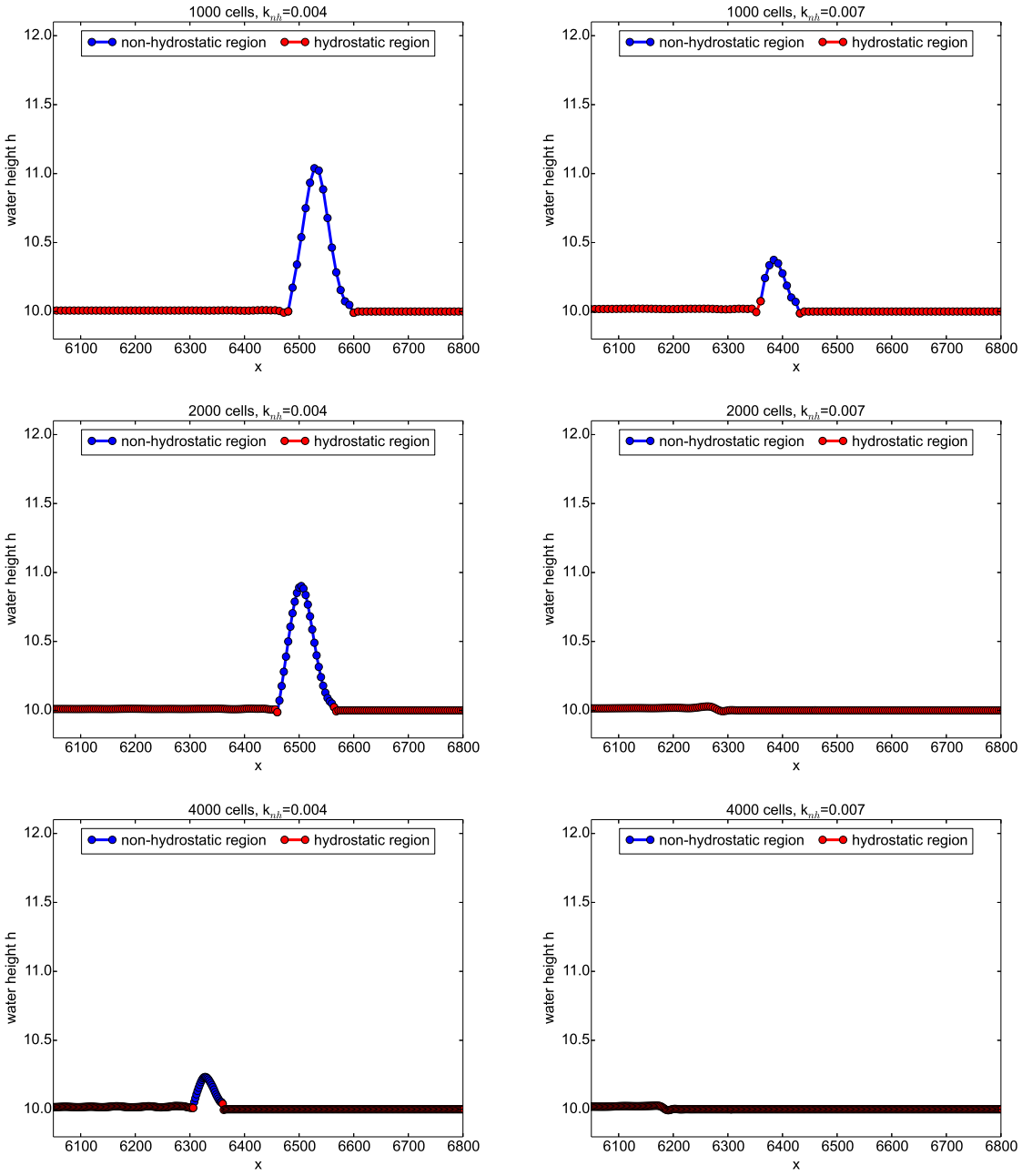

Figure 4.3.: Propagating solitary wave applying the local approach after a simulation time of 10 minutes: Three resolutions with $1000, 2000$ and 4000 cells are combined with two splitting parameters $k_{nh} \in \{0.004, 0.007\}$.

a solitary wave. The computational efficiency gain of the hydrostatic model run compared to the non-hydrostatic model run is approximately 60%. Hence, the local approach saves $2/3$ of the overhead of the non-hydrostatic extension. In case of larger computational domains and longer simulation times, the improvement may be even higher.

4.4.2. Solitary wave on an inundated simple beach

The description of this inundation test is given in section 3.7.7. Its adaptation to the local approach considers the splitting parameter $k_{nh} = 0.001$. This choice is made according to the results presented in section 4.4.1. The efficiency results of this test are depicted in table 4.2, that is the analogue to table 4.1. The computational efficiency gain of the local approach compared to the non-hydrostatic model run is at least 14%. The computational efficiency

cell number	t^{comp}_{nh1st}[min]	$t^{comp}_{0.001}$[min]	t^{comp}_{hy}[min]
50	0.22	0.19	0.12
100	0.95	0.82	0.46
200	5.86	4.01	1.75
400	83.42	39.28	7.52

cell number	$t^{comp}_{nh1st}/t^{comp}_{hy}$	$t^{comp}_{0.001}/t^{comp}_{hy}$
50	1.83	1.58
100	2.05	1.77
200	3.34	2.29
400	11.09	5.22

cell number	1-$t^{comp}_{0.001}/t^{comp}_{nh1st}$	1-$t^{comp}_{hy}/t^{comp}_{nh1st}$
50	0.14	0.45
100	0.14	0.51
200	0.32	0.7
400	0.53	0.91

Table 4.2.: Propagating simple wave on an inundated simple beach applying the local approach: Computational time depending on resolution (upper table) of the global first order non-hydrostatic model, the local approach with the splitting parameter $k_{nh} = 0.001$ and the hydrostatic model. All values are averages of three model runs. The overhead compared to hydrostatic computations (middle table) and the efficiency gain compared to non-hydrostatic computations in section 3.7.7 (lower table) are shown.

gain of the hydrostatic model run compared to the non-hydrostatic model run is at least 45%. Hence, the local approach saves 30% of the overhead of the non-hydrostatic extension for this test case if the coarsest resolution is considered. This is less than the percentage of approximately 66% for the solitary wave test in the previous section 4.4.1. The reason is the wet-dry treatment in the inundation test that excludes dry cells from the computational domain. An increasing number of cells leads to a similar saving of $0.53/0.91 = 58\%$ in the overhead of the non-hydrostatic extension for this test case.

Figure 4.4 and 4.5 display the results of the local approach and are the analogue to figures 3.18 and 3.19 in section 3.7.7. The results are very similar. The clearest difference is seen in figure 3.18 at non-dimensional time $t = 65$ during drawback process. This test shows appropriate results of the local approach also in combination with a non-constant bathymetry and the inundation process.

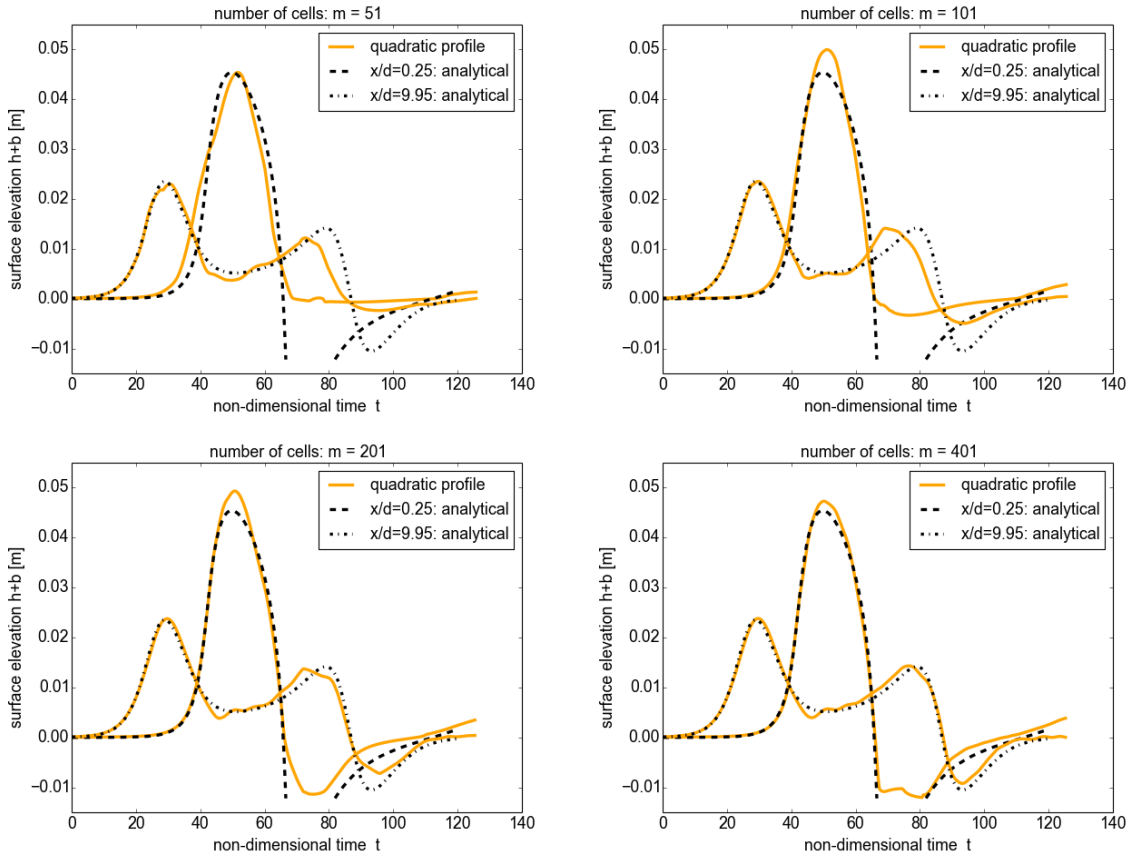

Figure 4.4.: Solitary wave on an inundated simple beach applying the local approach: Convergence plots at two points on the shoreline. Convergence plots are generated with constant CFL number as described in section 3.7.3.

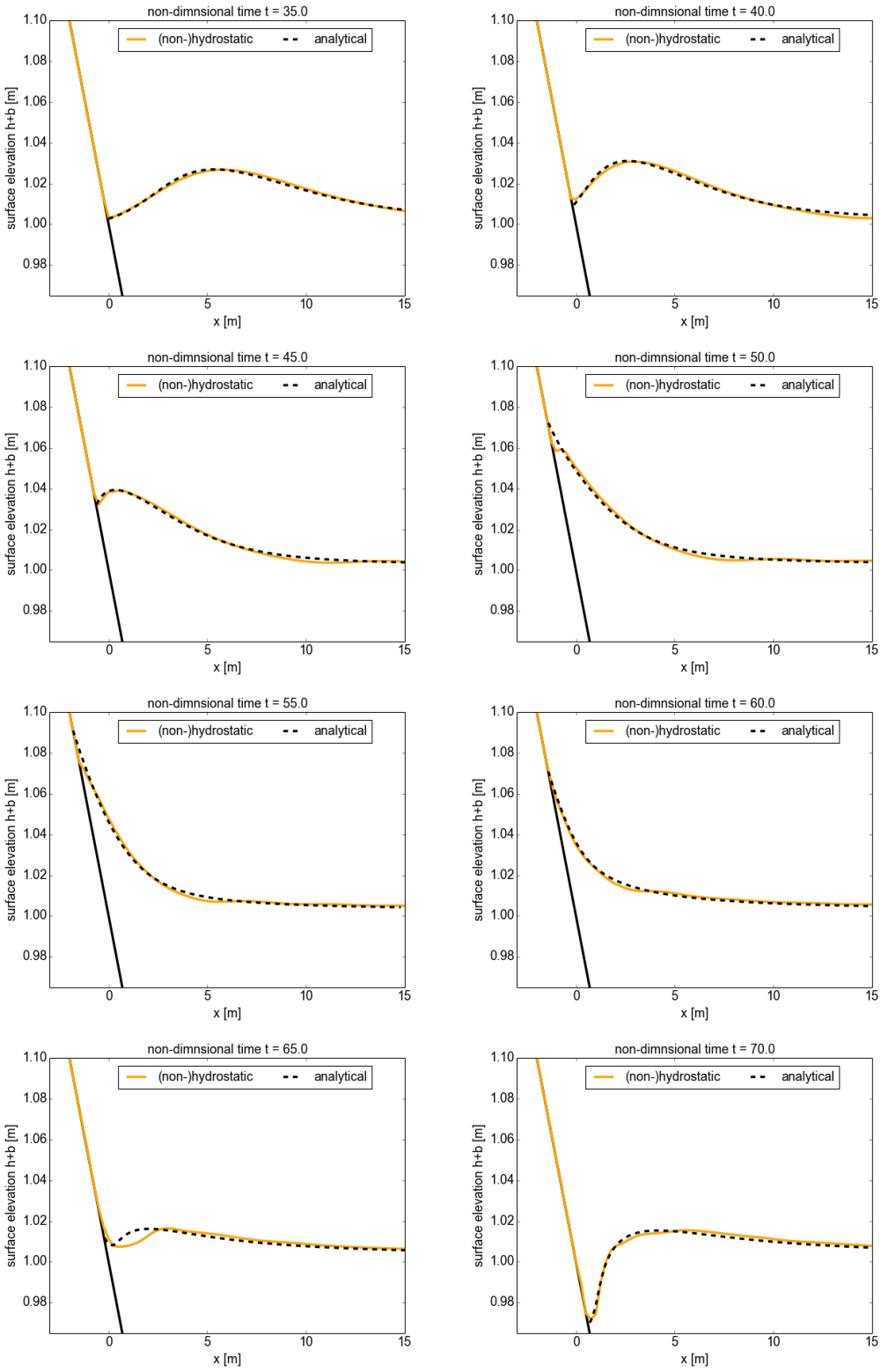

Figure 4.5.: Solitary wave on an inundated simple beach applying the local approach: Comparison of the analytical (black) surface elevation with simulation results (yellow).

5 Conclusions and future research

This thesis provided new contributions to the research field that is concerned with the modeling of dispersive shallow water flows. These contributions are of analytical as well as of numerical nature. The analytical results treat the different underlying physical assumptions inherent in depth-averaged Boussinesq-type equations and the depth-averaged non-hydrostatic extension for shallow water equations. The different physical assumption is the vertical profile of the non-hydrostatic pressure. We derived an equivalence of the non-hydrostatic extension for shallow water equations to well-known Boussinesq-type equations through adaptation of the vertical pressure profile. Numerically, we constructed a discretization for the non-hydrostatic equation set that is a for the first time both a discontinuous Galerkin model and second order convergent compared to analytical solutions. These solutions were known from Boussinesq-type equations and the previous shown equivalence enabled their usage for the non-hydrostatic extension for shallow water equations, too. Efficiency concerns were treated with the idea of solving dispersive equations on local regions only and resorting to the hydrostatic equations otherwise. The details of analytical and numerical contributions are elaborated in the following.

The distinguishing physical assumption between the depth-averaged non-hydrostatic equation set and Boussinesq-type equations was shown to be the vertical profile of the non-hydrostatic pressure. Existing non-hydrostatic equation sets apply a linear vertical profile, whereas Boussinesq-type equations consider a quadratic vertical profile. However, we found that it is the quadratic pressure profile that is consistent with vertical profiles of all other quantities arising in the Euler equations of motion. The linear profile lacks this important property. We showed that the linear pressure profile inherits weaker linear dispersion than the quadratic pressure profile. Additionally, the quadratic pressure profile is the correct one in the long wave limit ($\frac{d}{\lambda} \to 0$). Because of weaker dispersion, the linear profile yields too short and too high solitary waves. However, in the region of $\frac{d}{\lambda} > 0.25$ approximately, the model using a linear profile matches better with the dispersion relation of full linearized equations.

Applying the quadratic vertical profile to the non-hydrostatic equation set yields equivalence to specific Boussinesq-type equations. These are the Serre equations on constant bathymetry and the Green-Naghdi equations on non-constant bathymetry. The non-hydrostatic equation set is a rewriting of the equivalent Boussinesq-type equations as a system of first order partial

differential equations. Hence, no mixed space-time derivatives and no higher order derivatives occur, but two additional quantities are introduced. These quantities are the vertical velocity or vertical momentum and the non-hydrostatic pressure. The change of the vertical pressure profile resorts to the adaptation of one single parameter in case of the non-hydrostatic equation set on constant bathymetry. On non-constant bathymetry, more terms including the bathymetry gradient need to be taken into account to obtain equivalence to Green-Naghdi equations. The equivalence to the Serre and Green-Naghdi equations enabled us to known analytical solutions for the non-hydrostatic extension for shallow water equations. Hence, convergence tests of numerical models for the non-hydrostatic equation set compared to analytical solutions are possible. Existent numerical models for the non-hydrostatic equation set were usually not tested for convergence. Instead, graphical comparisons served to argue that properties of the numerical model were sufficient. We recommend to use the quadratic pressure profile in non-hydrostatic models instead of the linear pressure profile to make sure that the models have appropriate convergence properties compared to analytical solutions. However, for validation of the non-hydrostatic model the pressure profile may be adapted and studied further.

We were able to numerically demonstrate the equivalence to Serre equations through the adaptation of one single parameter that is responsible for switching the pressure profile. On non-constant bathymetry the numerical counterpart of the equivalence is more involved, because a difficulty arise in the second extra parameter, which includes a time-derivative. It is not clear, how to include this time-derivative into the fractional step method, because it appears on the right-hand side of the non-hydrostatic equation set.

For the first time, we derived a second order model for the non-hydrostatic extension for shallow water equations. Convergence was tested compared to analytical standing and solitary wave solutions gained from the equivalence. We restricted ourselves to the one-dimensional case. We found that the principle of deriving second order projection methods for incompressible Navier-Stokes equations applies to fractional step methods for the non-hydrostatic equation set, too. This is true for periodic and Dirichlet boundary conditions at least. The non-hydrostatic pressure terms need to be included in the predictor in combination with a linear extrapolation to the next time step. The corrector equations correct the error made in this extrapolation.

The second order model is a discontinuous Galerkin (DG) discretization in one spatial dimension. This is the first DG scheme for the non-hydrostatic extension for shallow water equations. The predictor applies the Runge-Kutta DG method with linear polynomials and Heun's scheme. The elliptic system for the non-hydrostatic pressure is solved as a system of first order equations using the local discontinuous Galerkin (LDG) method. Additionally to zero Dirichlet boundary conditions found in the literature, we derived numerical fluxes to discretize problems with periodic and reflecting boundary conditions and proofed their stable behavior. The implemented reflecting boundary condition was not able to maintain the second

order convergence though. The test case of the linear solitary wave on a composite beach revealed the difficulty of defining a suitable reflecting boundary condition in combination with the LDG approach for the non-hydrostatic extension for shallow water equations. This is a disadvantage considering the projection method compared to Boussinesq-type models. However, the ease of extending an existent shallow water model to include dispersive effects remains as the main advantage of projection methods.

Numerical tests confirm the stable and accurate behavior of the second order DG model. We validated the non-hydrostatic model with analytical solutions and experimental data using Dirichlet, periodic and reflecting boundary conditions completed with an inundation scheme. The non-hydrostatic model showed accurate properties on constant bathymetry and during the inundation process. The influence of the vertical pressure profile on model results followed analytical considerations described above. The non-hydrostatic model may produce clearly distinguishable results on non-constant bathymetry depending on the choice of vertical pressure profile. The linear pressure profile may yield results that excel the results applying the quadratic profile compared to experimental data. The literature provides studies of the discretized Green-Naghdi equations that perform better than the model results applying both pressure profiles. Hence, we supposed that the reason is the parameter f_{d}, that is not included in the non-hydrostatic model so far.

A local approach of the non-hydrostatic model was presented in order to improve the computational efficiency. The local approach considered a splitting of the computational domain into non-hydrostatic and hydrostatic regions. The full non-hydrostatic equation set were solved in the non-hydrostatic region whereas the purely hydrostatic equations were solved in the hydrostatic regions. The domain splitting used a simple splitting criterion according to linear theory and was based on the surface elevation. The inner domain boundary conditions of both regions were considered to be zero Dirichlet boundary data. The non-hydrostatic model in combination with the non-incremental projection method, that leads to the first order convergent non-hydrostatic model, was considered for the local approach. Preliminary feasibility and efficiency studies were conducted. The combination of a small value of the splitting criterion and rather coarse resolution was found to be most beneficial for appropriate representation of the wave profile and efficient computation in case of long propagation times. The local approach was tested with the solitary wave test case and an inundation test. Both cases led to a saving of approximately 60% of the computational overhead of the non-hydrostatic model compared to the hydrostatic model.

The above specified results permit further research on each topic. First of all, the numerical counterpart of the analytical findings is established on a constant bathymetry only. The numerical treatment of the terms inherent in the parameter f_{d} provides an interesting research topic for the future. The problem related to the time-derivative may be treated with a technique following [67]. Hence, the material derivative of the velocity may be replaced with its shallow water approximation or with a more accurate dispersive approximation. After including this

term into the non-hydrostatic model, one could conduct convergence tests in case of non-constant bathymetry, too.

A second extension of this work may the performance of more tests, especially with non-constant bathymetry. Tests including smooth bathymetries could further explain different behaviors of both pressure profiles. More realistic scenarios may be considered to show that the non-hydrostatic model is suitable under even more demanding circumstances. The development of a two-dimensional version of our one-dimensional non-hydrostatic model would be appropriate for this purpose. However, when including the two-dimensional non-hydrostatic equation set into an existing shallow water model, the issue of efficiency will play a major role than in the one-dimensional case. The LDG method applied in this thesis to solve the system of elliptic equations may be replaced with the compact discontinuous Galerkin (CDG) method [15, 81]. This method is an improvement regarding matrix sparsity of the LDG method. Both methods are identical if they are reduced to one spatial dimension. The choice of the solver may also be reconsidered. Results of a detailed efficiency inspection [48] regarding solution strategies for the linear equation system in non-hydrostatic models using a finite element discretization may be transferable to our DG discretization.

The local approach may be tested for efficiency and feasibility under more complicated situations, too. The splitting criterion may be adapted in order to consider bathymetry gradients or wave steepness for example. The zero Dirichlet inner boundary condition may be replaced by inflow and outflow boundary conditions that may reduce the splitting error at the inner boundaries. A domain decomposition approach similar to [9] may be considered, too.

A comparison study with Boussinesq-type models could be undertaken, after improving the efficiency of the non-hydrostatic model. In this thesis, we started the comparison with respect to analytical properties and through broadening the similarities of non-hydrostatic models compared to state-of-the-art Boussinesq-type models. Both model types are expected [92] to be computationally comparable. Although the definition of suitable criteria may not be obvious, a detailed answer could contribute to the development of dispersive models for large scale and realistic applications.

Acknowledgments

The completion of this thesis would not have been possible without the support of number of people. First of all, I would like to express my gratitude to my supervisors, Prof. Dr. Jörn Behrens and Dr. Stefan Vater, for the opportunity to realize this doctoral project, for helpful scientific advice and continuous encouragement. Thank you, Jörn, for letting me try things out and for the possibility to attend several interesting international conferences, and in particular, the research stay in New York City. Thank you, Stefan, for your constructive criticism on a variety of details. My work benefited a lot from it.

Furthermore, I address special thanks to Prof. Dr. Geir Pedersen for the productive and pleasant collaboration. Thank you, Geir, for your freely offered advice and many helpful insights in different scientific directions.

Many thanks are also due to my panel chair Prof. Dr. Johanna Baehr who was asking the right questions to advance my work combined with a large portion of humor. In this regard, I gratefully acknowledge the support of the School of Integrated Climate System Sciences for providing the helpful organizational structure for the PhD project and for all enjoyable networking meetings with PhD students from various disciplines.

I am grateful for the awesome opportunity Prof. Dr. Kyle Mandli gave me to join his group at Columbia University in New York City for a couple of weeks. Thank you, Kyle, very much for the inviting atmosphere and the great possibility to join the comparison project.

I would like to thank all present and former members of our working group for all vivid scientific discussions, regular meetings and the distraction especially during lunch breaks. Thank you, Anusha and Yumeng, for sharing good and difficult times of a PhD life. Special thanks go to Susanne - thank you for the inspiring off-topic conversations and everything else. Likewise, I would like to thank the members of the SIAM Student Chapter Hamburg for lively conversations during PhD lunches, field trips and officer meetings.

I am indebted to Dr. Stefan Vater and Dr. Susanne Beckers for proofreading. Furthermore, I thank all free software developers for the great work they are doing.

I owe my deepest gratitude to my husband, my family and my friends, who supported and encouraged me patiently throughout the PhD time. And last but not least, I thank the One who knows me best and is continuously guiding my life according to His endless grace.

Bibliography

[1] Aïssiouene, N. "Numerical analysis and discrete approximation of a dispersive shallow water model". PhD thesis. Pierre et Marie Curie, Paris VI, 2016.

[2] Aïssiouene, N. et al. "A combined finite volume - finite element scheme for a dispersive shallow water system". In: *Networks & Heterogeneous Media* 11.1 (2016), pp. 1–27. DOI: 10.3934/nhm.2016.11.1.

[3] Aïssiouene, N. et al. "Application of a Combined Finite Element - Finite Volume Method to a 2D Non-hydrostatic Shallow Water Problem". In: *Finite Volumes for Complex Applications VIII - Hyperbolic, Elliptic and Parabolic Problems*. 2017, pp. 219–226.

[4] Arnold, D. N. et al. "Unified analysis of discontinuous Galerkin methods for elliptic problems". In: *SIAM Journal on Numerical Analysis* 39.5 (2002), pp. 1749–1779.

[5] Bai, Y. and Cheung, K. F. "Depth-integrated free-surface flow with parameterized non-hydrostatic pressure". In: *International Journal for Numerical Methods in Fluids* 71.4 (2013), pp. 403–421. DOI: 10.1002/fld.3664.

[6] Bai, Y. and Cheung, K. F. "Dispersion and kinematics of multi-layer non-hydrostatic models". In: *Ocean Modelling* 92 (2015), pp. 11–27. DOI: 10.1016/j.ocemod.2015.05.005.

[7] Beji, S. and Battjes, J. "Experimental investigation of wave propagation over a bar". In: *Coastal Engineering* 19.1 (1993), pp. 151–162. DOI: http://dx.doi.org/10.1016/0378-3839(93)90022-Z.

[8] Beji, S. and Battjes, J. "Numerical simulation of nonlinear wave propagation over a bar". In: *Coastal Engineering* 23.1 (1994), pp. 1–16. DOI: http://dx.doi.org/10.1016/0378-3839(94)90012-4.

[9] Blayo, E. and Rousseau, A. "About Interface Conditions for Coupling Hydrostatic and Nonhydrostatic Navier-Stokes Flows". In: *Discrete and Continuous Dynamical Systems-Series S* 9.5 (2016), pp. 1565–1574.

[10] Bonneton, P. et al. "A splitting approach for the fully nonlinear and weakly dispersive Green-Naghdi model". In: *Journal of Computational Physics* 230.4 (2011), pp. 1479–1498.

[11] Bonneton, P. et al. "Recent advances in Serre-Green Naghdi modelling for wave transformation, breaking and runup processes". In: *European Journal of Mechanics-B/Fluids* 30.6 (2011), pp. 589–597.

[12] Botelho, D. et al. "A hydrostatic/non-hydrostatic grid-switching strategy for computing high-frequency, high wave number motions embedded in geophysical flows". In: *Environmental Modelling & Software* 24.4 (2009), pp. 473–488.

[13] Boussinesq, J. "Théorie des ondes et des remous qui se propagent le long d'un canal rectangulaire horizontal, en communiquant au liquide contenu dans ce canal des vitesses sensiblement pareilles de la surface au fond." In: *J. Mathématiques Pures et Appliquées* 17 (1872), pp. 55–108.

[14] Boussinesq, J. "Théorie générale des mouvements qui sont propagés dans un canal rectangulaire horizontal." In: *C. R. Acad. Sci* Paris 73 (1871), pp. 256–260.

[15] Brdar, S., Dedner, A., and Klöfkorn, R. "Compact and stable Discontinuous Galerkin methods for convection-diffusion problems". In: *SIAM Journal on Scientific Computing* 34.1 (2012), A263–A282.

[16] Bristeau, M.-O. et al. "An energy-consistent depth-averaged Euler system: Derivation and properties". In: *Discrete & Continuous Dynamical Systems* (2015).

[17] Brocchini, M. "A reasoned overview on Boussinesq-type models: An interplay between physics, mathematics and numerics". In: *Proceeding Royal Society A, London* 469.2160 (2013).

[18] Brown, D. L., Cortez, R., and Minion, M. L. "Accurate projection methods for the incompressible Navier-Stokes equations". In: *Journal of computational physics* 168.2 (2001), pp. 464–499.

[19] Butcher, J. C. *The numerical analysis of ordinary differential equations: Runge-Kutta and general linear methods*. Wiley-Interscience, 1987.

[20] Castillo, P. "An optimal estimate for the local discontinuous Galerkin method". In: *Discontinuous Galerkin Methods: Theory, Computation and Applications*. Ed. by Cockburn, B., Karniadakis, G. E., and Shu, C.-W. Berlin, Heidelberg: Springer Berlin Heidelberg, 2000, pp. 285–290. DOI: 10.1007/978-3-642-59721-3_23.

[21] Castillo, P. "Performance of discontinuous Galerkin methods for elliptic PDEs". In: *SIAM Journal on Scientific Computing* 24.2 (2002), pp. 524–547.

[22] Castillo, P. "A review of the local discontinuous Galerkin (LDG) method applied to elliptic problems". In: *Applied Neurophysiologyumerical Mathematics* 56.10-11 (2006), pp. 1307–1313.

[23] Castillo, P. et al. "An a priori error analysis of the local discontinuous Galerkin method for elliptic problems". In: *SIAM Journal on Numerical Analysis* 38.5 (2000), pp. 1676–1706.

[24] Castillo, P. et al. "Optimal a priori error estimates for the hp-version of the local discontinuous Galerkin method for convection-diffusion problems". In: *Mathematics of Computation* 71.238 (2002), pp. 455–478.

[25] Castro, M., Escalante, C., and Luna, T. M. de. "Modelling and Simulation of Non-hydrostatic Shallow Flows". In: *International Conference on Finite Volumes for Complex Applications*. Springer. 2017, pp. 119–126.

[26] Casulli, V. and Stelling, G. "Numerical Simulation of 3D Quasi-Hydrostatic, Free-Surface Flows." In: *Journal of Hydraulic Engineering* 124.7 (1998), pp. 678–686.

[27] Casulli, V. "A semi-implicit finite difference method for non-hydrostatic, free-surface flows". In: *International Journal for Numerical Methods in Fluids* 30.4 (1999), pp. 425–440.

[28] Chorin, A. "Numerical Solution of the Navier-Stokes Equations". In: *Mathematics of Computation* 22.104 (1968), pp. 745–762. DOI: 10.2307/2004575.

[29] Cockburn, B. "Discontinuous Galerkin methods". In: *Zeitschrift für Angewandte Mathematik und Mechanik* 83.11 (2003), pp. 731–754. DOI: 10.1002/zamm.200310088.

[30] Cockburn, B., Hou, S., and Shu, C.-W. "The Runge-Kutta local projection discontinuous Galerkin finite element method for conservation laws IV. The multidimensional case". In: *Mathematics of Computation* 54.190 (1990), pp. 545–581.

[31] Cockburn, B., Lin, S.-Y., and Shu, C.-W. "TVB Runge-Kutta local projection discontinuous Galerkin finite element method for conservation laws III: One-dimensional systems". In: *Journal of Computational Physics* 84.1 (1989), pp. 90–113.

[32] Cockburn, B. and Shu, C.-W. "TVB Runge-Kutta local projection discontinuous Galerkin finite element method for conservation laws II. General framework". In: *Mathematics of Computation* 52.186 (1989), pp. 411–435.

[33] Cockburn, B. and Shu, C.-W. "The Runge-Kutta local projection P^1-discontinuous Galerkin finite element method for scalar conservation laws". In: *ESAIM: Mathematical Modelling and Numerical Analysis* 25.3 (1991), pp. 337–361.

[34] Cockburn, B. and Shu, C.-W. "The local discontinuous Galerkin method for time-dependent convection-diffusion systems". In: *SIAM Journal on Numerical Analysis* 35.6 (1998), pp. 2440–2463.

[35] Cockburn, B. and Shu, C.-W. "The Runge-Kutta discontinuous Galerkin method for conservation laws V: Multidimensional systems". In: *Journal of Computational Physics* 141.2 (1998), pp. 199–224.

[36] Cockburn, B. and Shu, C.-W. "Runge-Kutta discontinuous Galerkin methods for convection-dominated problems". In: *Journal of scientific computing* 16.3 (2001), pp. 173–261.

[37] Cui, H. "A new numerical model for simulating the propagation of and inundation by tsunami waves". PhD thesis. TU Delft, Delft University of Technology, 2013.

[38] Cui, H., Pietrzak, J., and Stelling, G. "Optimal dispersion with minimized Poisson equations for non-hydrostatic free surface flows". In: *Ocean Modelling* 81 (2014), pp. 1–12. DOI: 10.1016/j.ocemod.2014.06.004.

[39] Dias, F. and Milewski, P. "On the fully-nonlinear shallow-water generalized Serre equations". In: *Physics Letters A* 374.8 (2010), pp. 1049–1053. DOI: 10.1016/j.physleta.2009.12.043.

[40] Dingemans, M. "Comparison of computations with Boussinesq-like models and laboratory measurements". In: *Memo in framework of MAST project (G8-M), Delft Hydraulics memo H1684. 12* (1994).

[41] Donahue, A. S. et al. "A Boussinesq-scaled, pressure-Poisson water wave model". In: *Ocean Modelling* 86 (2015), pp. 36–57.

[42] Dumbser, M. and Facchini, M. "A space-time discontinuous Galerkin method for Boussinesq-type equations". In: *Applied Mathematics and Computation* 272, Part 2 (2016), pp. 336–346. DOI: 10.1016/j.amc.2015.06.052.

[43] Engsig-Karup, A. P. et al. "Nodal DG-FEM solution of high-order Boussinesq-type equations". In: *Journal of engineering mathematics* 56.3 (2006), pp. 351–370.

[44] Escalante, C., Luna, T. M. de, and Castro, M. "Non-Hydrostatic Pressure Shallow Flows: GPU Implementation Using Finite-Volume and Finite-Difference Scheme". In: *arXiv preprint arXiv:1706.04551* (2017).

[45] Eskilsson, C. and Sherwin, S. J. "Spectral/hp discontinuous Galerkin methods for modelling 2D Boussinesq equations". In: *Journal of Computational Physics* 212.2 (2006), pp. 566–589.

[46] Fringer, O., Gerritsen, M., and Street, R. "An unstructured-grid, finite-volume, nonhydrostatic, parallel coastal ocean simulator". In: *Ocean Modelling* 14.3 (2006), pp. 139–173.

[47] Fringer, O. B., McWilliams, J. C., and STREET, R. L. "Hybrid Model". In: *Oceanography* 19.1 (2006), p. 64.

[48] Fuchs, A. "Effiziente parallele Verfahren zur Lösung verteilter, dünnbesetzter Gleichungssysteme eines nichthydrostatischen Tsunamimodells". PhD thesis. AWI, Universität Bremen, 2013.

[49] Gallacher, P. C., Hebert, D. A., and Schaferkotter, M. R. "Nesting a nonhydrostatic model in a hydrostatic model: The boundary interface". In: *Ocean Modelling* 40.2 (2011), pp. 190–198.

[50] Gear, C. *Numerical initial value problems in ordinary differential equations*. Prentice-Hall series in automatic computation. Prentice-Hall, 1971.

[51] Giraldo, F. X. and Warburton, T. "A high-order triangular discontinuous Galerkin oceanic shallow water model". In: *International Journal for Numerical Methods in Fluids* 56.7 (2008), pp. 899–925. DOI: 10.1002/fld.1562.

[52] Glimsdal, S. et al. "Dispersion of tsunamis: Does it really matter?" In: *Natural Hazards and Earth System Sciences* 13.6 (2013), pp. 1507–1526.

[53] Gottlieb, S., Shu, C.-W., and Tadmor, E. "Strong stability-preserving high-order time discretization methods". In: *SIAM review* 43.1 (2001), pp. 89–112.

[54] Green, A. E. and Naghdi, P. M. "A derivation of equations for wave propagation in water of variable depth". In: *Journal of Fluid Mechanics* 78 (02 1976), pp. 237–246. DOI: 10.1017/S0022112076002425.

[55] Grimshaw, R. "The solitary wave in water of variable depth. Part 2". In: *Journal of Fluid Mechanics* 46 (1971), pp. 611–622.

[56] Guermond, J.-L., Minev, P., and Shen, J. "An overview of projection methods for incompressible flows". In: *Computer Methods and Programs in Biomedicineethods in Applied Mechanics and Engineering* 195.44 (2006), pp. 6011–6045.

[57] Hesthaven, J. S. and Warburton, T. *Nodal Discontinuous Galerkin Methods: Algorithms, Analysis, and Applications*. Springer, 2008. DOI: 10.1007/978-0-387-72067-8.

[58] Hildebrand, F. B. *Introduction to Numerical Analysis*. Courier Corporation, 1987.

[59] Horrillo, J., Kowalik, Z., and Shigihara, Y. "Wave Dispersion Study in the Indian Ocean-Tsunami of December 26, 2004". In: *Marine Geodesy* 29.3 (2006), pp. 149–166. DOI: 10.1080/01490410600939140.

[60] Jeschke, A., Vater, S., and Behrens, J. "A Discontinuous Galerkin Method for Non-hydrostatic Shallow Water Flows". In: *International Conference on Finite Volumes for Complex Applications*. Springer. 2017, pp. 247–255.

[61] Jeschke, A. et al. "Depth-averaged Non-hydrostatic Extension for Shallow Water Equations with Quadratic Vertical Pressure Profile: Equivalence to Boussinesq-type Equations". In: *International Journal for Numerical Methods in Fluids* (2017). DOI: 10.1002/fld.4361.

[62] Kanarska, Y., Shchepetkin, A., and McWilliams, J. C. "Algorithm for non-hydrostatic dynamics in the Regional Oceanic Modeling System". In: *Ocean Modelling* 18 (2007), pp. 143–174. DOI: 10.1016/j.ocemod.2007.04.001.

[63] Kânoğlu, U. and Synolakis, C. E. "Long wave runup on piecewise linear topographies". In: *Journal of Fluid Mechanics* 374 (1998), pp. 1–28. DOI: 10.1017/S0022112098002468.

[64] Kirby, J. T. et al. *FUNWAVE 1.0: Fully nonlinear Boussinesq wave model - Documentation and user's manual*. Tech. rep. University of Delaware, 1998.

[65] Kutta, M. W. "Beitrag zur näherungsweisen Integration totaler Differentialgleichungen". In: *Zeitschrift für Mathematik und Physik* 46 (1901), pp. 435–453.

[66] Lannes, D. and Bonneton, P. "Derivation of asymptotic two-dimensional time-dependent equations for surface water wave propagation". In: *Physics of Fluids* 21.1 (2009), p. 016601.

[67] Lannes, D. and Marche, F. "A new class of fully nonlinear and weakly dispersive Green-Naghdi models for efficient 2D simulations". In: *Journal of Computational Physics* 282 (2015), pp. 238–268.

[68] Løvholt, F., Lynett, P., and Pedersen, G. "Simulating run-up on steep slopes with operational Boussinesq models; capabilities, spurious effects and instabilities". In: *Nonlinear Processes in Geophysics* 20.3 (2013), pp. 379–395. DOI: 10.5194/npg-20-379-2013.

[69] Luth, H. R., Klopman, G., and Kitou, N. *Project 13G: Kinematics of waves breaking partially on an o shore bar; LDV measurements for waves with and without a net onshore current*. Tech. rep. Delft Hydraulics, 1994.

[70] Lynett, P. and Liu, P. L. "A multi-layer approach to wave modeling". In: *Proceeding Royal Society London, A* 460 (2004), pp. 2637–2669.

[71] Lynett, P. and Liu, P. L. "A two-layer approach to wave modeling". In: *Proceeding Royal Society London, A* 460 (2004), pp. 2637–2669.

[72] Ma, G., Shi, F., and Kirby, J. T. "Shock-capturing non-hydrostatic model for fully dispersive surface wave processes". In: *Ocean Modelling* 43 (2012), pp. 22–35. DOI: 10.1016/j.ocemod.2011.12.002.

[73] Madsen, P. A. and Schäffer, H. "Higher-order Boussinesq-type equations for surface gravity waves: Derivation and analysis". In: *Philosophical Transactions of The Royal Society A* 356 (1998), pp. 3123–3184.

[74] Madsen, P. A. and Sørensen, O. R. "A new form of the Boussinesq equations with improved linear dispersion characteristics. Part 2. A slowly-varying bathymetry". In: *Coastal Engineering* 18.3 (1992), pp. 183–204. DOI: https://doi.org/10.1016/0378-3839(92)90019-Q.

[75] Marshall, J. et al. "A finite-volume, incompressible Navier-Stokes model for studies of the ocean on parallel computers". In: *Journal of Geophysical Research: Oceans* 102.C3 (1997), pp. 5753–5766.

[76] Marshall, J. et al. "Hydrostatic, quasi-hydrostatic, and nonhydrostatic ocean modeling". In: *Journal of Geophysical Research: Oceans* 102.C3 (1997), pp. 5733–5752.

[77] Mei, C. C. *The Applied Dynamics of Ocean Surface Waves*. World Scientific: Singapore, 1989.

[78] Musumeci, R. E., Svendsen, I. A., and Veeramony, J. "The flow in the surf zone: A fully nonlinear Boussinesq-type of approach". In: *Coastal Engineering* 52.7 (2005), pp. 565–598. DOI: 10.1016/j.coastaleng.2005.02.007.

[79] Panda, N. et al. "Discontinuous Galerkin methods for solving Boussinesq-Green-Naghdi equations in resolving non-linear and dispersive surface water waves". In: *Journal of Computational Physics* 273 (2014), pp. 572–588.

[80] Penner, J. E. et al. "Development of an atmospheric climate model with self-adapting grid and physics". In: *Journal of Physics: Conference Series*. Vol. 16. 1. 2005, p. 353.

[81] Peraire, J. and Persson, P.-O. "The compact discontinuous Galerkin (CDG) method for elliptic problems". In: *SIAM Journal on Scientific Computing* 30.4 (2008), pp. 1806–1824.

[82] Peregrine, D. H. "Equations for water waves and the approximations behind them". In: *Waves on beaches and resulting sediment transport* (1972), pp. 95–121.

[83] Reed, W. and Hill, T. "Triangular mesh methods for the neutron transport equation". In: Los Alamos report LA-UR-73-479, 1973.

[84] Runge, C. "Über die numerische Auflösung von Differentialgleichungen". In: *Mathematische Annalen* 46.2 (1895), pp. 167–178.

[85] Rusanov, V. V. "The calculation of the interaction of non-stationary shock waves with barriers". In: *Zh. Vychisl. Mat. Mat. Fiz.* 1:2 (1961), 267–279. [English transl.: U.S.S.R. Comput. Math. Math. Phys., 1:2 (1962), 304–320].

[86] Seabra-Santos, F. J., Renouard, D. P., and Temperville, A. M. "Numerical and experimental study of the transformation of a solitary wave over a shelf or isolated obstacle". In: *Journal of Fluid Mechanics* 176 (Mar. 1987), pp. 117–134. DOI: 10.1017/S0022112087000594.

[87] Serre, F. "Contribution à l'étude des écoulements permanents et variables dans les canaux". In: *La Houille Blanche* 3 (1953), pp. 374–388.

[88] Shu, C.-W. "Total-variation-diminishing time discretizations". In: *SIAM Journal on Scientific and Statistical Computing* 9.6 (1988), pp. 1073–1084.

[89] Shu, C.-W. and Osher, S. "Efficient Implementation of Essentially Non-oscillatory Shock-Capturing Schemes". In: *Journal of Computational Physics* 77.2 (1988), pp. 439–471. DOI: 10.1016/0021-9991(88)90177-5.

[90] Son, S., Lynett, P. J., and Kim, D.-H. "Nested and multi-physics modeling of tsunami evolution from generation to inundation". In: *Ocean Modelling* 38.1-2 (2011), pp. 96–113.

[91] Stansby, P. K. and Zhou, J. G. "Shallow-water flow solver with non-hydrostatic pressure: 2D vertical plane problems". In: *International Journal for Numerical Methods in Fluids* 28.3 (1998), pp. 541–563.

[92] Stelling, G. and Zijlema, M. "An accurate and efficient finite-difference algorithm for non-hydrostatic free-surface flow with application to wave propagation". In: *International Journal for Numerical Methods in Fluids* 43.1 (2003), pp. 1–23. DOI: 10.1002/fld.595.

[93] Stelling, G. S. and Busnelli, M. M. "Numerical simulation of the vertical structure of discontinuous flows". In: *International Journal for Numerical Methods in Fluids* 37.1 (2001), pp. 23–43.

[94] Synolakis, C. et al. "Standards, criteria, and procedures for NOAA evaluation of tsunami numerical models". In: *Report No. NOAA Tech. Memo. OAR PMEL-135, NOAA/Pacific Marine Environmental Laboratory, Seattle, WA* (2007).

[95] Synolakis, C. E. "The runup of long waves". PhD thesis. California Institute of Technology, Pasadena, California, 1986.

[96] Synolakis, C. E. "The runup of solitary waves". In: *Journal of Fluid Mechanics* 185 (1987), pp. 523–545. DOI: 10.1017/S002211208700329X.

[97] Temam, R. "Sur l'approximation de la solution des équations de Navier-Stokes par la méthode des pas fractionnaires (II)". In: *Archive for Rational Mechanics and Analysis* 33.5 (1969), pp. 377–385.

[98] Tissier, M. et al. "A new approach to handle wave breaking in fully non-linear Boussinesq models". In: *Coastal Engineering* 67 (2012), pp. 54–66. DOI: https://doi.org/10.1016/j.coastaleng.2012.04.004.

[99] Toro, E. F. *Riemann Solvers and Numerical Methods for Fluid Dynamics: A Practical Introduction*. 3rd ed. Springer, 2009.

[100] Vater, S., Beisiegel, N., and Behrens, J. "A Limiter-Based Well-Balanced Discontinuous Galerkin Method for Shallow-Water Flows with Wetting and Drying: One-Dimensional Case". In: *Advances in Water Resources* 85 (2015), pp. 1–13. DOI: 10.1016/j.advwatres.2015.08.008.

[101] Walters, R. A. "A semi-implicit finite element model for non-hydrostatic (dispersive) surface waves". In: *International Journal for Numerical Methods in Fluids* 49.7 (2005), pp. 721–737. DOI: 10.1002/fld.1019.

[102] Ward, D. L. *Physical model study of Revere Beach, Massachusetts*. Tech. rep. Coastal Engineering Research Center Vicksburg MS, 1995.

[103] Wei, Z. and Jia, Y. "Simulation of nearshore wave processes by a depth-integrated non-hydrostatic finite element model". In: *Coastal Engineering* 83 (2014), pp. 93–107.

[104] Whitham, G. B. *Linear and Nonlinear Waves*. John Wiley & Sons, New York, 1974.

[105] Yamazaki, Y., Kowalik, Z., and Cheung, K. F. "Depth-integrated, non-hydrostatic model for wave breaking and run-up". In: *International Journal for Numerical Methods in Fluids* 61.5 (2009), pp. 473–497. DOI: 10.1002/fld.1952.

[106] Yan, J. and Shu, C.-W. "Local discontinuous Galerkin methods for partial differential equations with higher order derivatives". In: *Journal of Scientific Computing* 17.1-4 (2002), pp. 27–47.

[107] Zhang, Y. et al. "Boussinesq–Green-Naghdi rotational water wave theory". In: *Coastal Engineering* 73 (2013), pp. 13–27.

[108] Zijlema, M., Stelling, G., and Smit, P. "SWASH: An operational public domain code for simulating wave fields and rapidly varied flows in coastal waters". In: *Coastal Engineering* 58.10 (2011), pp. 992–1012. DOI: http://dx.doi.org/10.1016/j.coastaleng.2011.05.015.

List of Figures

List of Tables

List of symbols

Abbreviations

CFL	Courant-Friedrichs-Lewy
CDG	compact discontinuous Galerkin
DG	discontinuous Galerkin
G4, ..., G10	wave gauges
KdV	Korteweg-de-Vries
LDG	local discontinuous Galerkin
local approach	local non-hydrostatic extension for shallow water equations
global approach	first order non-hydrostatic model
model system	general elliptic system of equations (3.47)–(3.48)
non-hydrostatic equation set	non-hydrostatic extension for shallow water equations (2.23)–(2.26), (3.1)–(3.2) or (3.5)–(3.6)
(non-)hydrostatic region	subset of the computational domain Ω in which the (non-)hydrostatic equation set is solved
non-hydrostatic model	discretized non-hydrostatic equation set
RK-DG(2)	(second order) Runge-Kutta discontinuous Galerkin method
SSP	strong stability-preserving
TVD	total-variation diminishing

Notations

a	maximal wave amplitude
α_{ml}	Runge-Kutta coefficients
Ai	Airy function
$b(x)$, $-d(\boldsymbol{x})$	bathymetry
β_{ml}	Runge-Kutta coefficients

c, c_{nh}, c_{sw}	phase velocity, of the non-hydrostatic model, of the shallow water model
c_{11}, c_{12}, c_{22}	stability parameters in LDG method
d	still water level
$\boldsymbol{d} \cdot \boldsymbol{q} = 0$	divergence constraint (3.9)
Δt, Δx	time step, spatial grid size
$(\Delta x)_c$, $(\Delta x)_f$	spatial grid size of a triangulation with coarser, finer resolution
e	cell interface (including boundary edges)
e_m	error w. r. t. the $L^2(Omega)$- or L^∞-norm of a simulation run using a triangulation with m cells
$\boldsymbol{E_z} \in \mathbb{R}^3$	unit vector in z-direction
$\mathcal{E}_h$, $\mathcal{E}_{h,in}$	set of cell interfaces (including boundary edges), set of inner cell interfaces
η	expansion coefficient for the wave number
$\Theta_{i,h}$, Θ_h	integral over cell boundary ∂I_i according to (3.52), over all cells according to (3.54)
f_1, f_2	right hand sides of the model system (3.47)–(3.48)
$\boldsymbol{F}$	source term of external forces
$\boldsymbol{f}$, $\boldsymbol{f}'(\boldsymbol{q})$	combined time-discrete flux term of non-hydrostatic equation set (see (3.36)), its derivative
$\boldsymbol{f}^*$	numerical interface flux between two adjacent cells of the RK-DG method
$\boldsymbol{f}^*_{\mathsf{rus}}(\boldsymbol{q})$	numerical interface flux computed with the Rusanov solver
f_{nh}, f_{d}	scalars to choose the vertical pressure profile
$\boldsymbol{f_{nh}}(p^{nh}, h)$	flux vector of non-hydrostatic pressure terms
$\boldsymbol{f_{sw}}(\boldsymbol{q})$	flux vector of shallow water equations
g	gravitational acceleration
g_1, g_2, h_1, h_2	coefficients of the model system (3.47)–(3.48)
$\gamma_{m_f}^{m_c}$	experimental convergence order computed out of two simulation runs with a coarser (m_c) and a finer (m_f) resolution
Γ	abbreviation (2.29)
h	water depth
$(\cdot)_h$	quantity discretized in space
$(\cdot)_i$	quantity in cell I_i
$\boldsymbol{h_{sw}}$, $\boldsymbol{h_{nh}}$	one time step with Heun' scheme for shallow water equations, for non-hydrostatic pressure terms
I_h, I_i, ∂I_i	triangulation I_h of computational domain Ω into cells I_i, boundary of cell I_i

k	polynomial order of approximation
k_{nh}	splitting parameter of local approach
K	scale factor for the solitary wave
$\kappa = \frac{2\pi}{\lambda}$	wave number
l	domain length
l_{max}	maximum eigenvalue of $\boldsymbol{f}'(\boldsymbol{q})$
λ	wave length
m	number of cells I_i in computational domain Ω
$\boldsymbol{m}$	local mass matrix
m_c, m_f	cell number of a triangulation with coarser and finer resolution
n, $n^{\mathsf{test}}(m)$	time step, time step to evaluate the convergence test
n_h	outwards pointing normal of cell I_i
ν	kinematic viscosity
ξ	surface elevation
$(\cdot)_\xi$, $(\cdot)_{-d}$	function evaluated at the water surface $z = \xi$, at the bathymetry $z = -d$
$\omega = \frac{2\pi}{T}$	wave frequency
$\omega_{\mathsf{nh,quad}}$, $\omega_{\mathsf{nh,lin}}$	wave frequency of the non-hydrostatic equation set with quadratic pressure profile and linear pressure profile
ω_{Se}, $\omega_{\mathsf{nh,full}}$	wave frequency of the Serre equations and the full linearized inviscid equations
Ω	computational domain
q, q_{ref}	either h, hu, hw, or p^{nh}, and its reference solution
$\boldsymbol{q}$, $\boldsymbol{q}^{eu,n+1}$	vector of variables $(h, hu, hw)^T$, explicit Euler step at time step $n+1$
p, p_h, $\hat{p}_h$	pressure, its discretized counterpart and its numerical LDG flux in the model system (3.47)–(3.48)
p^{nh}, $(p^{nh})^{ex,n+1}$	depth-averaged non-hydrostatic pressure, extrapolated according to (3.27) to time step $n+1$
P, P^{hy}, P^{nh}	total, hydrostatic, non-hydrostatic pressure
$P_k(I_i)$	space of polynomials with degree less or equal to k on cell I_i
Π_h	limiter
$\mathcal{Q}_h$, $Q_h(I_i)$	global discontinuous finite element space, local finite element space on cell I_i
r	approximation order of extrapolation (3.27)
$\boldsymbol{r_{nh}}(p^{nh})$	right hand side vector of the non-hydrostatic equation set restricted to non-hydrostatic pressure terms

$\boldsymbol{r_h}(\boldsymbol{q}_h)$	right hand side vector of equation (3.12)
$\boldsymbol{r_{sw}}(\boldsymbol{q})$	right hand side vector of the non-hydrostatic equation set excluding non-hydrostatic pressure terms
ρ	density
$\boldsymbol{s}$	combined time-discrete source term of non-hydrostatic equation set, see (3.37)
$\boldsymbol{s_{nh}}(p^{nh})$	source vector of non-hydrostatic pressure terms
$\boldsymbol{s_{sw}}(\boldsymbol{q})$	source vector of shallow water equations
$\partial_t \cdot$, $\frac{\partial}{\partial t}\cdot$, $(\cdot)_t$	partial time derivative
t	time
$t^{\text{comp}}_{\text{nh2nd}}$, $t^{\text{comp}}_{\text{nh1st}}$, $t^{\text{comp}}_{\text{hy}}$	computational time of second order non-hydrostatic first order non-hydrostatic and hydrostatic model
$t^{\text{comp}}_{k_{nh}}$	computational time of first order non-hydrostatic model with local approach and specified value of splitting parameter k_{nh}
t^{test}	time to evaluate the convergence test
T	wave period
u, u_h, $\hat{u}_h$	velocity, its discretized counterpart and its numerical LDG flux in the model system (3.47)–(3.48)
$\boldsymbol{u}(x,y) = (u,v)^T(x,y)$	depth-averaged horizontal velocity
$\boldsymbol{U}(x,y,z) = (U,V)^T(x,y,z)$	horizontal velocity
$\boldsymbol{V}(x,y,z) = (U,V,W)^T(x,y,z)$	velocity
$\mathcal{V}$, $\mathcal{V}_h$	space of test functions (see (3.35)), space of basis functions (see (3.41))
$w(x,y)$	depth-averaged vertical velocity
φ, φ_j	test function or basis function
Φ	abbreviation (2.30)
$\boldsymbol{x} = (x,y)^T$	horizontal coordinates
$\partial_x \cdot$, $\frac{\partial}{\partial x}\cdot$, $(\cdot)_x$	partial spatial derivative in x-direction
$\partial_y \cdot$, $\frac{\partial}{\partial y}\cdot$, $(\cdot)_y$	partial spatial derivative in y-direction
x_0	initial horizontal displacement
z	vertical coordinate
$\boldsymbol{\nabla}_3 = (\partial_x, \partial_y, \partial_z)^T$	three-dimensional gradient operator
$\boldsymbol{\nabla} = (\partial_x, \partial_y)^T$	two-dimensional gradient operator
$[\![\cdot]\!]$, $\{\cdot\}$	jump and average of a quantity at cell interfaces (including boundary edges)
$()^+$, $()^-$	value of a discrete function at right and left side of cell interface (including boundary edges)
$\widetilde{\cdot}$	predicted quantities

A Derivation of general pressure relation

We derive the general pressure relation on non-constant bathymetries for two dimensions based on the one-dimensional version of the derivation given in [86]. The vertical velocity profile (2.14) reformulates using intermediate steps out of (2.19) to

$$W(z) = -(z+d)(\boldsymbol{\nabla}\cdot\boldsymbol{u}) - \boldsymbol{\nabla}d\cdot\boldsymbol{u}.$$

Hence, the terms on the left-hand side of the vertical Euler momentum equation including the vertical velocity are displayed as

$$\begin{aligned}
\partial_t W =& -(z+d)(\boldsymbol{\nabla}\cdot\boldsymbol{u}_t) - \boldsymbol{\nabla}d\cdot\partial_t\boldsymbol{u},\\
\boldsymbol{u}\cdot\boldsymbol{\nabla}W =& -\boldsymbol{u}\cdot\boldsymbol{\nabla}\left((z+d)(\boldsymbol{\nabla}\cdot\boldsymbol{u}) + \boldsymbol{\nabla}d\cdot\boldsymbol{u}\right)\\
=&(-\boldsymbol{u}\cdot\boldsymbol{\nabla}d)(\boldsymbol{\nabla}\cdot\boldsymbol{u}) - ((\boldsymbol{u}\cdot\boldsymbol{\nabla})(\boldsymbol{\nabla}\cdot\boldsymbol{u}))(z+d) - (\boldsymbol{u}\cdot\boldsymbol{\nabla})(\boldsymbol{\nabla}d\cdot\boldsymbol{u})\\
=&(-\boldsymbol{u}\cdot\boldsymbol{\nabla}d)(\boldsymbol{\nabla}\cdot\boldsymbol{u}) - ((\boldsymbol{u}\cdot\boldsymbol{\nabla})(\boldsymbol{\nabla}\cdot\boldsymbol{u}))(z+d)\\
&-\boldsymbol{u}\cdot\boldsymbol{\nabla}(\boldsymbol{\nabla}d)\cdot\boldsymbol{u} - ((\boldsymbol{u}\cdot\boldsymbol{\nabla})\boldsymbol{u})\cdot\boldsymbol{\nabla}d,\\
W\partial_z W =& -(\boldsymbol{\nabla}\cdot\boldsymbol{u})W = (\boldsymbol{\nabla}\cdot\boldsymbol{u})\left((z+d)(\boldsymbol{\nabla}\cdot\boldsymbol{u}) + \boldsymbol{\nabla}d\cdot\boldsymbol{u}\right)\\
=&(\boldsymbol{\nabla}\cdot\boldsymbol{u})^2(z+d) + (\boldsymbol{\nabla}\cdot\boldsymbol{u})(\boldsymbol{\nabla}d\cdot\boldsymbol{u}).
\end{aligned}$$

Therefore, we get another description of the right hand side

$$\begin{aligned}
-\frac{1}{\rho}\partial_z P^{nh} =&\partial_t W + \boldsymbol{u}\cdot\boldsymbol{\nabla}W + W\partial_z W\\
=&(z+d)\left(-(\boldsymbol{\nabla}\cdot\partial_t\boldsymbol{u}) - (\boldsymbol{u}\cdot\boldsymbol{\nabla})(\boldsymbol{\nabla}\cdot\boldsymbol{u}) + (\boldsymbol{\nabla}\cdot\boldsymbol{u})^2\right)\\
&-\boldsymbol{\nabla}d\cdot(\partial_t\boldsymbol{u} + (\boldsymbol{u}\cdot\boldsymbol{\nabla})\boldsymbol{u}) - \boldsymbol{u}\cdot\boldsymbol{\nabla}(\boldsymbol{\nabla}d)\cdot\boldsymbol{u}\\
=:&(z+d)\frac{\Gamma}{h} + \Phi.
\end{aligned}$$

We obtain the non-hydrostatic pressure depending on the vertical coordinate using an integration

$$\frac{1}{\rho}P^{nh}(z) = \int_{\xi}^{z} \partial_z \left(\frac{1}{\rho}P^{nh}\right) dz = \frac{1}{2}\frac{\Gamma}{h}\left(-(z+d)^2 + h^2\right) + \Phi\left(\xi - z\right),$$

which gives on the one hand the depth-averaged non-hydrostatic pressure

$$\frac{1}{\rho}p^{nh} = \frac{1}{h}\int_{-d}^{\xi} \frac{1}{\rho}P^{nh}(z)\, dz = \frac{1}{3}h\Gamma + \frac{1}{2}h\Phi$$

and on the other hand the non-hydrostatic pressure at the bottom

$$\frac{1}{\rho}P^{nh}_{-d} = \frac{1}{2}h\Gamma + h\Phi.$$

We balance the terms containing Γ of both pressures. Hence, we obtain the general pressure relation

$$P^{nh}_{-d} = \frac{3}{2}p^{nh} + \frac{1}{4}\rho h\Phi.$$

B Convergence results

B.1. Poisson problem

The Poisson problem (3.21)–(3.22) with zero Dirichlet boundary data

$$p = 0 \quad \text{on } \partial\Omega$$

is solved on the computational domain $\Omega = [-1, 1]$ with a chosen right hand side

$$f(x) = -\sin(\pi(x+1))\pi^2.$$

The corresponding analytical solution for primal and flux variables is

$$p(x) = \sin(\pi(x+1)),$$
$$u(x) = \cos(\pi(x+1))\pi.$$

Table B.1 shows second order of convergence for both the primal variable p and the flux variable u. For definitions of e_m and $\gamma_{m_f}^{m_c}$, see equations (3.71) and (3.72).

variable	norm	e_9	e_{17}	e_{33}	e_{65}	γ_{17}^{9}	γ_{33}^{17}	γ_{65}^{33}
p	$L^2(\Omega)$	7.650e-02	1.691e-02	3.942e-03	9.484e-04	2.177	2.101	2.055
	$L^\infty(\Omega)$	1.679e-01	4.103e-02	1.017e-02	2.532e-03	2.033	2.013	2.006
u	$L^2(\Omega)$	1.805e-01	4.581e-02	1.148e-02	2.871e-03	1.978	1.996	2.000
	$L^\infty(\Omega)$	2.500e-01	6.597e-02	1.671e-02	4.182e-03	1.922	1.981	1.999

Table B.1.: Experimental errors and orders of convergence for the Poisson problem and zero Dirichlet boundary conditions.

B.2. Periodic standing wave

variable	norm	e_{80}	e_{160}	e_{320}	e_{640}	γ_{160}^{80}	γ_{320}^{160}	γ_{640}^{320}
h	$L^2(\Omega)$	6.253e-06	1.551e-06	3.858e-07	9.620e-08	2.011	2.007	2.004
	$L^\infty(\Omega)$	2.439e-06	6.061e-07	1.510e-07	3.767e-08	2.009	2.005	2.003
hu	$L^2(\Omega)$	8.560e-05	2.113e-05	5.248e-06	1.308e-06	2.019	2.009	2.005
	$L^\infty(\Omega)$	3.687e-05	9.121e-06	2.264e-06	5.645e-07	2.015	2.010	2.004
hw	$L^2(\Omega)$	1.305e-04	3.216e-05	7.985e-06	1.989e-06	2.020	2.010	2.005
	$L^\infty(\Omega)$	5.650e-05	1.397e-05	3.474e-06	8.661e-07	2.016	2.008	2.004
p^{nh}	$L^2(\Omega)$	4.311e-05	1.061e-05	2.628e-06	6.505e-07	2.023	2.013	2.015
	$L^\infty(\Omega)$	1.710e-05	4.221e-06	1.048e-06	2.600e-07	2.018	2.010	2.011

Table B.2.: Experimental errors and orders of convergence for the test case standing wave with quadratic vertical pressure profile and periodic boundary conditions at time $t = 3\,\mathrm{s}$.

B.3. Periodic solitary wave

variable	norm	e_{200}	e_{400}	e_{800}	e_{1600}	γ_{400}^{200}	γ_{800}^{400}	γ_{1600}^{800}
h	$L^2(\Omega)$	1.165e-01	2.929e-02	7.126e-03	1.729e-03	1.992	2.039	2.043
	$L^\infty(\Omega)$	2.009e-02	5.046e-03	1.241e-03	3.031e-04	1.993	2.024	2.034
hu	$L^2(\Omega)$	1.220e-00	3.061e-01	7.437e-02	1.809e-02	1.994	2.041	2.039
	$L^\infty(\Omega)$	2.139e-01	5.561e-02	1.390e-02	3.470e-03	1.943	2.001	2.002
hw	$L^2(\Omega)$	4.106e-01	1.020e-01	2.501e-02	6.185e-03	2.010	2.028	2.016
	$L^\infty(\Omega)$	1.040e-01	2.614e-02	6.579e-03	1.671e-03	1.993	1.990	1.977
p^{nh}	$L^2(\Omega)$	2.376e-01	5.928e-02	1.461e-02	3.629e-03	2.003	2.020	2.010
	$L^\infty(\Omega)$	6.113e-02	1.530e-02	3.890e-03	1.007e-03	1.999	1.975	1.949

Table B.3.: Experimental errors and orders of convergence for the test case solitary wave with quadratic vertical pressure profile and periodic boundary conditions at time $t = 50\,\mathrm{s}$. The incremental second order scheme with linear ($r = 1$) extrapolated non-hydrostatic pressure according to table 3.4 is applied.

variable	norm	e_{200}	e_{400}	e_{800}	e_{1600}	γ_{400}^{200}	γ_{800}^{400}	γ_{1600}^{800}
h	$L^2(\Omega)$	1.591e-01	4.000e-02	9.832e-03	2.473e-03	1.992	2.024	1.991
	$L^\infty(\Omega)$	2.798e-02	7.004e-03	1.729e-03	4.304e-04	1.998	2.019	2.006
hu	$L^2(\Omega)$	1.645e+00	4.114e-01	1.005e-01	2.510e-02	1.999	2.034	2.001
	$L^\infty(\Omega)$	2.906e-01	7.416e-02	1.849e-02	4.690e-03	1.971	2.004	1.979
hw	$L^2(\Omega)$	5.547e-01	1.365e-01	3.295e-02	8.174e-03	2.023	2.050	2.011
	$L^\infty(\Omega)$	1.388e-01	3.434e-02	8.440e-03	2.137e-03	2.015	2.025	1.982
p^{nh}	$L^2(\Omega)$	2.393e-01	1.351e-01	7.730e-02	4.162e-02	0.824	0.806	0.893
	$L^\infty(\Omega)$	6.761e-02	2.787e-02	1.447e-02	7.644e-03	1.279	0.946	0.920

Table B.4.: Experimental errors and orders of convergence for the test case solitary wave with quadratic vertical pressure profile and periodic boundary conditions at time $t = 50\,\mathrm{s}$. The incremental second order scheme with zero ($r = 0$) extrapolated non-hydrostatic pressure according to table 3.4 is applied.

B.4. Reflecting standing wave

variable	norm	e_{80}	e_{160}	e_{320}	e_{640}	γ_{160}^{80}	γ_{320}^{160}	γ_{640}^{320}
h	$L^2(\Omega)$	3.788e-04	1.875e-04	9.331e-05	4.654e-05	1.014	1.007	1.003
	$L^\infty(\Omega)$	1.239e-04	6.062e-05	2.994e-05	1.486e-05	1.031	1.018	1.010
hu	$L^2(\Omega)$	4.204e-03	2.080e-03	1.035e-03	5.161e-04	1.015	1.007	1.004
	$L^\infty(\Omega)$	1.336e-03	6.596e-04	3.277e-04	1.633e-04	1.019	1.009	1.005
hw	$L^2(\Omega)$	6.608e-03	3.269e-03	1.626e-03	8.108e-04	1.015	1.008	1.004
	$L^\infty(\Omega)$	2.400e-03	1.154e-03	5.590e-04	2.729e-04	1.056	1.045	1.035
p^{nh}	$L^2(\Omega)$	1.995e-03	9.783e-04	4.845e-04	2.411e-04	1.028	1.014	1.007
	$L^\infty(\Omega)$	6.597e-04	3.193e-04	1.567e-04	7.744e-05	1.047	1.027	1.016

Table B.5.: Experimental errors and orders of convergence for the test case standing wave with reflecting boundary conditions and first order scheme after a simulation time of $t = 3\,\mathrm{s}$.

variable	norm	e_{80}	e_{160}	e_{320}	e_{640}	γ_{160}^{80}	γ_{320}^{160}	γ_{640}^{320}
h	$L^2(\Omega)$	5.407e-05	1.980e-05	7.121e-06	2.539e-06	1.449	1.475	1.488
	$L^\infty(\Omega)$	1.881e-04	9.754e-05	4.964e-05	2.504e-05	0.948	0.974	0.987
hu	$L^2(\Omega)$	1.159e-04	2.865e-05	7.124e-06	1.776e-06	2.016	2.008	2.004
	$L^\infty(\Omega)$	4.931e-05	1.225e-05	3.051e-06	7.603e-07	2.009	2.006	2.005
hw	$L^2(\Omega)$	4.616e-04	1.546e-04	5.310e-05	1.850e-05	1.578	1.541	1.521
	$L^\infty(\Omega)$	1.519e-03	7.483e-04	3.714e-04	1.850e-04	1.021	1.011	1.005
p^{nh}	$L^2(\Omega)$	5.296e-04	1.940e-04	6.981e-05	2.490e-05	1.449	1.475	1.487
	$L^\infty(\Omega)$	1.843e-03	9.558e-04	4.866e-04	2.455e-04	0.947	0.974	0.987

Table B.6.: Experimental errors and orders of convergence for the test case standing wave with reflecting boundary conditions and second order scheme after a simulation time of $t = 3\,\mathrm{s}$.